MANIPULATION OF CHARGE DENSITY WAVE INSTABILITIES IN TI-BASED TRANSITION-METAL DICHALCOGENIDES

Tommaso Antonelli

A Thesis Submitted for the Degree of PhD
at the
University of St Andrews

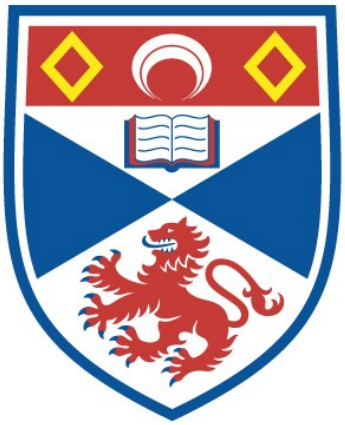

2023

Manipulation of charge density wave instabilities in Ti-based transition-metal dichalcogenides

Tommaso Antonelli

University of
St Andrews

This thesis is submitted in partial fulfilment for the degree of

Doctor of Philosophy (PhD)

at the University of St Andrews

August 2022

Candidate's declaration

I, Tommaso Antonelli, do hereby certify that this thesis, submitted for the degree of PhD, which is approximately 35,000 words in length, has been written by me, and that it is the record of work carried out by me, or principally by myself in collaboration with others as acknowledged, and that it has not been submitted in any previous application for any degree. I confirm that any appendices included in my thesis contain only material permitted by the 'Assessment of Postgraduate Research Students' policy.

I was admitted as a research student at the University of St Andrews in September 2018.

I received funding from an organisation or institution and have acknowledged the funder(s) in the full text of my thesis.

Date 30/08/2022 Signature of candidate

Supervisor's declaration

I hereby certify that the candidate has fulfilled the conditions of the Resolution and Regulations appropriate for the degree of PhD in the University of St Andrews and that the candidate is qualified to submit this thesis in application for that degree. I confirm that any appendices included in the thesis contain only material permitted by the 'Assessment of Postgraduate Research Students' policy.

Date 30/08/2022 Signature of supervisor

Permission for publication

In submitting this thesis to the University of St Andrews we understand that we are giving permission for it to be made available for use in accordance with the regulations of the University Library for the time being in force, subject to any copyright vested in the work not being affected thereby. We also understand, unless exempt by an award of an embargo as requested below, that the title and the abstract will be published, and that a copy of the work may be made and supplied to any bona fide library or research worker, that this thesis will be electronically accessible for personal or research use and that the library has the right to migrate this thesis into new electronic forms as required to ensure continued access to the thesis.

I, Tommaso Antonelli, have obtained, or am in the process of obtaining, third-party copyright permissions that are required or have requested the appropriate embargo below.

The following is an agreed request by candidate and supervisor regarding the publication of this thesis:

Printed copy

Embargo on all of print copy for a period of 1 year on the following ground(s):

- Publication would preclude future publication

Supporting statement for printed embargo request

I am planning to publish the majority of the data reported in this thesis in a scientific journal within the next year.

Electronic copy

Embargo on all of electronic copy for a period of 1 year on the following ground(s):

- Publication would preclude future publication

Supporting statement for electronic embargo request

I am planning to publish the majority of the data reported in this thesis in a scientific journal within the next year

Title and Abstract

- I require an embargo on the title and abstract but I understand that the title will be used in the graduation booklet.

Date 30/08/2022 Signature of candidate

Date 30/08/2022 Signature of supervisor

Underpinning Research Data or Digital Outputs

Candidate's declaration

I, Tommaso Antonelli, understand that by declaring that I have original research data or digital outputs, I should make every effort in meeting the University's and research funders' requirements on the deposit and sharing of research data or research digital outputs.

Date 30/08/2022 Signature of candidate

Permission for publication of underpinning research data or digital outputs

We understand that for any original research data or digital outputs which are deposited, we are giving permission for them to be made available for use in accordance with the requirements of the University and research funders, for the time being in force.

We also understand that the title and the description will be published, and that the underpinning research data or digital outputs will be electronically accessible for use in accordance with the license specified at the point of deposit, unless exempt by award of an embargo as requested below.

The following is an agreed request by candidate and supervisor regarding the publication of underpinning research data or digital outputs:

Embargo on all of electronic files for a period of 1 year on the following ground(s):

- Publication would preclude future publication

Supporting statement for embargo request

I am planning to publish the majority of the data reported in this thesis in a scientific journal within the next year.

Title and Description

- I require an embargo on the title and description

Date 30/08/2022 Signature of candidate

Date 30/08/2022 Signature of supervisor

Abstract

Transition metal dichalcogenides (TMDs) offer a versatile platform to study the interplay of different electronic interactions underpinning collective quantum phases such as ferromagnetism, superconductivity and charge density waves (CDW). In particular, $TiSe_2$ shows an anomalous CDW instability whose microscopic nature has been debated for ~ 50 years, but it still remains unclear. A similar phase transition has been recently observed in single layer $TiTe_2$, but not in the multilayer system opening further controversy on the origin of such lattice instability.

In this thesis, I explore different experimental methods for manipulating the CDW transition in TiX_2 (X = Se, Te) by means of molecular beam epitaxy and angle resolved photoemission spectroscopy (ARPES). I report an in-depth photoemission study of the anomalous lattice instability in single layer $TiTe_2$ providing the first evidence of an electronic energy gain driving the CDW phase in the monolayer configuration. The experimental results are rationalised in a minimal model that ultimately gives a natural explanation for the unusual dimensionality crossover of the CDW instability in $TiTe_2$. By chemically substituting Te with Se, 2D ML-$TiTe_{2x}Se_{2(1-x)}$ alloys are synthesised for the first time, showing a semiconductor ($x = 0$) to semimetal ($x = 1$) transition in the normal phase. The ARPES analysis reported here reveals the continuous evolution of the CDW instability across the entire alloy series opening a new route to manipulate this collective phase at the 2D limit. As an alternative approach, I explore the role of remote electronic screening in manipulating the CDW order in ML-$TiSe_2$. A V_2O_3 functional substrate able to switch between metallic (high screening) to insulating (low screening) phase is used for this purpose, although further optimisations are needed to improve the crystal quality of ML-$TiSe_2$ deposited on top.

This work brings critical new insights for the understanding of CDW-like states across the family of group-VI TMDs and to engineer collective electronic states in 2D materials.

Acknowledgements

This thesis would not be possible without the help and support of a number of people. First, I would like to thank my supervisor Prof. Phil King who made this project possible in the first place and tirelessly supported my work during these four years. I also would like to thank the remainder of the "King's group", past and present, for the numerous discussions, coffees, cakes and beers. Especially Anđela Zivanovic, Chiara Bigi, Gesa Siemann, Phil Murgatroyd, Matthew Watson, Akhil Rajan, Oliver J. Clark, Kaycee Underwood, Igor Marković, Edgar Abarca-Morales who helped to measure part of the data reported in this thesis during beamtimes at SOLEIL and Diamond. I am also particularly grateful to Matthew Watson for the long discussion on $TiSe_2$ and $TiTe_2$ and his essential contribution to the minimal model presented here. The work on $TiTe_2$ wouldn't have been possible without his help and the contribution of Warda Rahim and Prof. David Scanlon from UCL. I am also grateful to Luke Rhode for his help with the tight-binding model.

For the extensive work performed in the lab, I am grateful to Martin McLaren whose constant perseverance and commitment keep the lab in St. Andrews running. Another special thank goes to Akhil Rajan and Yoshiko Nanano for their great help with the MBE system and discussions regarding crystal growth. I am also very grateful to everyone involved with me in the development of *PyPhoto*: Prof. Phil King, Brendan Edwards, Lewis Hart, Liam Trzaska, Edgar Abarca Morales and Anđela Zivanovic.

From outside the Physics department, I would like to thank Mikel and Anken for the numerous nights spent together in St. Andrews. I am also particularly grateful to my family and my friends for giving me a smile every time I hear from them.

Finally, I would like to thank Gesa-Roxanne Siemann for sharing work and everyday life with me, supporting me during the long lockdown and the hard time I spent writing this thesis. Without her, my time spent in St Andrews wouldn't have been the same.

This work was supported by Leverhulme Trust.

List of Papers

1. **Orbital-selective Band Hybridisation at the Charge Density Wave Transition in Monolayer $TiTe_2$**

   T. Antonelli, W. Rahim, M. D. Watson, A. Rajan, O. J. Clark, A. Danilenko, K. Underwood, I. Markovic, E. Abarca-Morales, S. R. Kavanagh, P. Fevre, F. Bertran, K. Rossnagel, D. O. Scanlon, P. D. C. King

   npj Quantum Materials **7**, 98, (2022).

2. **Strong-coupling charge density wave in monolayer $TiSe_2$**

   M. D. Watson, A. Rajan, T. Antonelli, K. Underwood, I. Marković, F. Mazzola, O. J Clark, G.-R. Siemann, D. Biswas, A. Hunter, S. Jandura, J. Reichstetter, M. McLaren, P. Le Fèvre, G. Vinai, P. D. C. King

   2D Materials **8**, 015004, (2021).

3. **Giant valley-Zeeman coupling in the surface layer of an intercalated transition-metal dichalcogenide**

   B. Edwards, O. Dowinton, A. E. Hall, P. A. E. Murgatroyd, S. Buchberger, T. Antonelli, G.-R. Siemann, A. Rajan, E. Abarca Morales, A. Zivanovic, C. Bigi, R. V. Belosludov, C. M. Polley, G. Carbone, M. Leandersson, D. Mayoh, G. Balakrishnan, M. S. Bahramy, and Phil D. C. King

   Accepted for publication in Nature Materials

Contents

Chapter 1

Introduction

1.1 Motivation

Understanding the electron dynamics within a material is one of the most fundamental purposes of condensed matter physics. This research field has been fuelling the technological revolution started during the last century leading to the extreme miniaturisation of electronic devices, the development of more powerful and lighter batteries, and the creation of light emitting diodes (LED) and photovoltaic panels. The working principles of all these applications can be described by assuming the electrons travelling inside the device as independent particles weakly interacting with each other. When the interaction between such particles is strong enough, they start behaving as part of a collective system rather than as single entities, giving rise to interesting quantum phenomena such as ferromagnetism, superconductivity, spin density wave and charge density wave orders. While ferromagnetism and spin density wave derive from the coupling between the electron spins, conventional superconductivity and charge density wave emerge when the electron motion is coupled with the atomic vibrations inside the solid.

In 2005, the isolation of an atomically thin carbon layer, namely graphene [1], paved the way for creating a new class of two-dimensional (2D) materials. The electrons inside these systems are confined in two dimensions showing appealing transport and optical properties for a multitude of applications in nano- and optoelectronics [2–6]. Besides their remarkable single-particle properties, several collective electronic states have also been observed in such materials allowing us to investigate these intriguing quantum phenomena in reduced dimensions [7, 8].

Transition metal dichalcogenides are a class of 2D materials under intense study in this perspective [9–12]. These materials are made by a transition element M (Ti, V, Nb, Ta, etc.) and a chalcogenide X (S, Se, Te) which crystallise in layers where the M atoms are sandwiched between two layers of X, as shown in Fig. 1.1(a, b). These triple layers X-M-X, also called monolayers

(MLs) of MX_2, are stacked one over the others, forming a three-dimensional (3D) crystal held together only by weak van der Waals (v.d.W.) forces (Fig. 1.1(b)). Single or multi-layer films can be obtained by mechanically exfoliating the 3D crystals using tapes or synthesised using chemical or physical deposition techniques [13]. Depending on the local coordinate of M with its surrounding X atoms, three different polymorphs are obtained: trigonal (1T) with M in octahedral coordination, hexagonal (2H), and rhombohedral (3R) having trigonal prismatic coordination instead. Their crystal structure and the number of electrons of the transition metal ion dictate the filling of the conduction band as shown in Fig. 1.1(c) and thus the transport properties of the material. For instance, group-V TMDs have metallic properties as the conduction band is only half filled, while group-VI TMDs are typically semiconductors in the 2H configuration [13]. These latter, and in particular 2H-WSe_2 and 2H-MoS_2 have been employed as channel materials in transistors showing significant improvements in the room-temperature current on/off ratio, carrier mobility and ultralow standby power dissipation compared to devices based on Si technology [3, 14, 15].

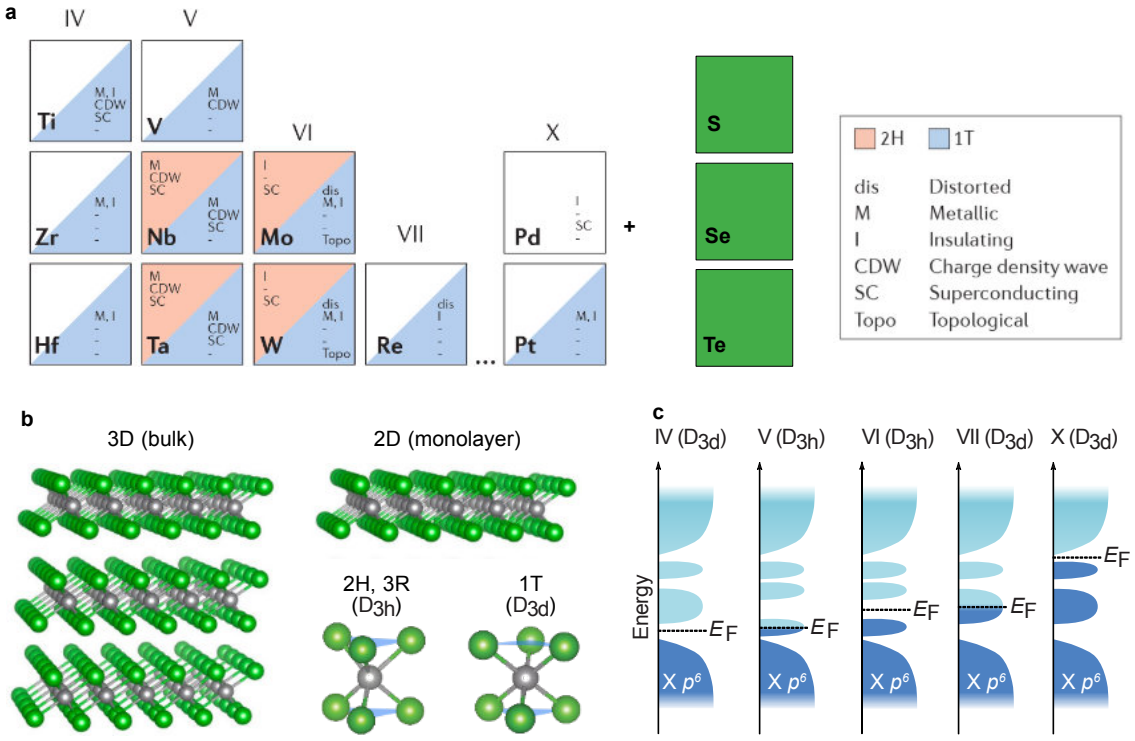

FIGURE 1.1: Overview of chemical composition (a) and crystal structure (b) and electronic density of states (c) of transition metal dichalcogenides MX_2. (a) and (c) adapted from Ref. [16] and Ref. [13], respectively.

Beyond their exceptional single-particle properties, TMDs also host a wide variety of interesting electronic collective states, such as superconductivity and CDW, as well as non-trivial topological states [16–18]. In particular, the microscopic nature of CDW instabilities in these systems has

been debated for over 50 years [12]. This collective electronic state is characterised by a static periodic modulation of the electronic density, which is expected to emerge in 1D or quasi-1D metals, while several CDW-like phases have also been observed in monolayer (2D) and bulk (3D) metallic TMD [12]. Another even more controversial case is the emergence of CDW instability in the narrow gap semiconductor compound $TiSe_2$ [19]. This material has also been considered a promising candidate to host an exotic electronic ground state formed by the condensation of electron-hole pairs, namely an excitonic insulator [20, 21]. A widely accepted understanding of CDW transition in this material hasn't been achieved yet [22–25], fuelling many scientific researches.

By manipulating the energy of the electronic states within the materials using chemical doping, applying external electrostatic field or hydrostatic pressure, the strength of different electronic interactions can be tuned, enhancing or suppressing the different collective phases. Fig. 1.2 shows the emergence of a superconducting dome and the simultaneous suppression of the CDW phase in $TiSe_2$ when this material is doped with Cu [9]. A similar interplay between superconductivity and CDW has also been observed in several high-temperature superconducting materials [26, 27], but this common behaviour is still not well elucidated and remains a central open issue in condensed matter physics.

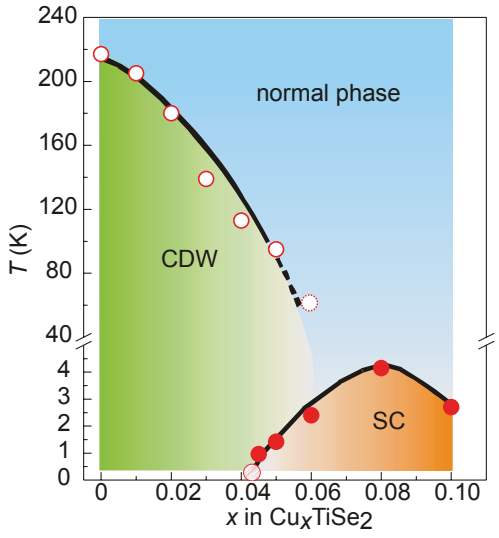

FIGURE 1.2: Phase diagram of $TiSe_2$ doped with Cu showing the suppression of the charge density wave (CDW) phase in favour of a superconducting (SC) dome. Adapted from Ref. [9].

The dimensionality of the system is also an important factor that can have dramatic consequences on collective electronic states. An extreme case is the CDW instability in $TiTe_2$ that emerges only in the monolayer compound while it is completely suppressed for multilayer and bulk crystals [28]. Why this collective ground state emerges only at the 2D limit is still unclear,

motivating part of the research presented in this thesis. The CDW ordering in the telluride single layer closely mimics the instability in ML-$TiSe_2$. However, in the former compound, the transition occurs at lower temperatures compared to the selenide, pointing to a different CDW strength between these two materials. Such difference suggests one can manipulate the microscopic electronic interaction by chemically substituting the chalcogenides in the 2D crystal. Recent experiments have also shown the critical temperature at which the transition occurs is affected by the electronic properties of the substrate placed below the single-layer TMD film [29, 30], although further studies are necessary to clarify how the substrate influences the CDW phase in ML-$TiSe_2$.

In this thesis, I present the research performed during my PhD proposing different methods for manipulating the CDW phase in Ti-based dichalcogenides. The research path followed during this work starts from the synthesis of the material and its structural and chemical characterisation. The changes in energy of the electronic states due to the CDW transition were then measured using angle resolved photoemission spectroscopy (ARPES) and analysed by combining first principles and model calculations. The approaches proposed here bring critical new insights for understanding how the CDW interaction reshapes the electric band structure of TiX_2 (X = Se, Te) materials and how to control quantum phases in 2D materials.

1.2 Outline of the Thesis

This thesis will begin with a brief introduction of the general theory underpinning the electron and lattice dynamics in solids (chapter 2), explaining the several approximations adopted to extract useful information from the complex quantum mechanics formalism. The conventional CDW theory is presented, revealing its limitation in describing the instabilities in real materials with a particular focus on TMDs. The long-studied CDW transition in monolayer and bulk $TiSe_2$ is described on the basis of a recent state-of-the-art ARPES analysis performed by Matthew Watson during his postdoc in St Andrews [31], revealing in detail the evolution of the electronic states across the transition.

The experimental methods used in this work are presented in chapter 3, starting from the crystal growth using molecular beam epitaxy (MBE) to the structural and electronic characterisation of the film using electron diffraction and photoemission spectroscopic techniques. Understanding the working principle of these techniques will be fundamental for correctly interpreting the experimental results shown in the rest of the thesis.

Chapter 4 is dedicated to the unusual dimensionality cross-over of the CDW instability in $TiTe_2$. Combining new ARPES experiments with first-principles and model calculations, this study reveals the energy gain driving the CDW in the monolayer and its suppression in the bulk compound, providing a natural basis for understanding CDW-like states across the family of group-IV chalcogenides.

In chapter 5, the CDW in monolayer Ti-based dichalcogenides is manipulated by chemically substituting the chalcogenides in the 2D film. Using MBE, 2D $TiTe_{2x}Se_{2(x-1)}$ alloys are synthesised, showing CDW transition occurring at different temperatures depending on the alloy composition.

The work reported in chapter 6 proposes another method for tuning the CDW interaction in ML-$TiSe_2$. A V_2O_3 functional substrate able to switch between a metallic and insulating state is used to control the external screening environment surrounding the TMD film deposited on top. The synthesis of such heterostructure reveals, however, complications that need to be overtaken to obtain sufficiently ordered crystals and observe the expected modulation in the CDW critical temperature.

The conclusion and outlook specific to each method will be discussed at the end of the respective chapters, while more general findings will be outlined in chapter 7, focussing on another alternative approach to engineer the CDW instabilities in 2D TMDs.

Chapter 2

Scientific Background

The electrical properties of materials are intimately connected to the dynamics of the electrons within the solid. Since the start of the 20^{th} century, a theory has been developed to describe the microscopic motion of the electrons, underlying the modern field of condensed matter physics. This chapter introduces some of the basic models describing the electron and lattice dynamics drawn from several well known textbooks [32–36]. This information will provide the essential knowledge to understand the intriguing quantum phases emerging in Ti-based dichalcogenides. The most notorious and studied material of this family, namely $TiSe_2$, will be taken here as an example to show the inadequacy of the conventional Peierls theory in describing the charge density wave transition in this class of compound.

2.1 The single electron approximation

Quantum mechanics provides the fundamental theory describing the dynamics of the microscopic particles within a material: electrons and atomic nuclei. When the system is in equilibrium, its quantum state represented by the many-particle wave function Ψ can be calculated by solving the many-particle time-independent Schödinger equation:

$$H\Psi = E\Psi \tag{2.1}$$

where E and H are the energy and the Hamiltonian of the system. Considering all the interaction between the electrons and nuclei, this latter takes the form [36]:

$$H = \sum_i \frac{\boldsymbol{p}_i^2}{2m_i} + \sum_j \frac{\boldsymbol{P}_j^2}{2M_j} + \frac{1}{2}{\sum_{j',j}}' \frac{Z_j Z_{j'} e^2}{|\boldsymbol{R}_j - \boldsymbol{R}_{j'}|} - \sum_{j,i} \frac{Z_j e^2}{|\boldsymbol{r}_i - \boldsymbol{R}_j|} + \frac{1}{2}{\sum_{i',i}}' \frac{e^2}{|\boldsymbol{r}_i - \boldsymbol{r}_{i'}|} \tag{2.2}$$

where $\boldsymbol{p}_i$ ($\boldsymbol{P}_j$) describes the momentum operator of the ith electron (jth nuclei) with mass m_i (M_j) respectively, $\boldsymbol{r}_i$ ($\boldsymbol{R}_j$) is the position vector, Z_j is the atomic number of the nucleus, and e is the electronic charge. The two first terms denote the kinetic energy of the single electrons and nuclei, while the successive terms represent the nucleus-nucleus, nucleus-electron, and electron-electron Coulomb interactions. Since the number of particle within a solid is typically on the order of $\sim 10^{23}$, the number of variables involved in eq. 2.2 is extremely large. Solving this equation for such multitudes of particles is computationally too expensive and completely unpractical with modern mathematical methods. Therefore, several approximations have to be adopted to extract useful information from the theory.

One of the most used approximations in condensed matter physics is the adiabatic approximation. Since the electrons are $\sim$ 1000 times lighter than the nuclei, their dynamics are much faster and can adapt almost instantaneously ($\sim$ fs) to the slower nucleus lattice vibrations ($\sim$ ps). Thus, one can calculate the electron dynamics $|\psi(u,r)\rangle$ assuming the lattice frozen into a particular configuration $|\phi(u)\rangle$ where u is the collection of all the nucleus positions $\{\boldsymbol{R}_j\}$. In modern $ab-inito$ calculations such as density functional theory (DFT), $|\psi(u,r)\rangle$ is computed assuming an initial guess of the atomic equilibrium positions in the crystal u_{init} . Holding the electronic density $|\psi(u_{init},r)|^2$ fixed, the internal forces acting on the lattice are estimated, and the atoms are relaxed into the new configuration u'. A new $|\psi(u',r)\rangle$ is computed again by iterating this process until the internal forces acting on the atoms are negligible. In this way, an estimate of the electronic states and the atomic positions at T=0 K is usually obtained.

To further facilitate the calculation of $|\psi(u,r)\rangle$, one can consider the electrons in the deep core atomic level trapped in the nuclear potential well. These electrons remain localised around the nuclear charge, strongly screening the nucleus Coulomb potential experienced by the other valence electrons that are instead delocalised over the entire crystal. As a result, the interaction between the ionic lattice and each valence electron can be ultimately combined into an average static periodic function $U(r)$ (the mean-field approximation). Excluding the electron-electron Coulomb repulsion, the Schödinger equation describing the motion of each electron takes the form:

$$H_{el}\psi = (\frac{p^2}{2m} + U(r))\Psi = E\psi \tag{2.3}$$

where H_{el} denotes the single electron Hamiltonian having as eigenvalues the single electron energies E and eigenstates ψ describing the single electron wavefunctions. In the next section, the solution to this simplified model will provide a basic qualitative description of the electron dynamics in solids.

2.1.1 Nearly free electron model

Considering the simplest case when $U(r)$ is constant in space, the solution of equation 2.3 takes the form:

$$\psi_k(r) = \frac{1}{\sqrt{V}} e^{-ikr}; \quad E_k = \frac{\hbar^2 k^2}{2m} + U \tag{2.4}$$

where V is the volume of the solid. Therefore, the non-interacting electrons are described by plane waves travelling in the material having a parabolic dispersion relation between energy and momentum k [1] named *band*, shown in Fig.2.1(a-b).

However, the Coulomb potential is not constant in real materials and depends on the atomic position within the solid. In crystals, the atoms arrange in a periodic structure, where a unit cell is repeatedly translated in space by a multiple of the lattice constant a as shown in Fig 2.1(c) for a simple monoatomic 1D crystal. Since the Coulomb potential $U(r)$ assumes the same lattice periodicity, the discrete translational symmetry of the system is reflected in the electronic states. Accordingly to the Bloch theorem, the eigenvectors of a periodic system assume the form:

$$\psi_k(r) = u_k(r) e^{ikr}; \quad u_k(r) = \frac{1}{\sqrt{V}} \sum_G c_{k-G} e^{-iGr} \tag{2.5}$$

where G is a reciprocal lattice vector. These so-called Bloch functions are the product of the plane wave complex factor e^{ikr} from 2.4 with a modulation $u_k(r)$ having the same periodicity of the direct lattice. It can be shown that these wavefunctions are periodic in the reciprocal space, and thus, their eigenvalues $E(k) = E(k + G)$ too. Therefore, all the information of the energy spectrum, i.e., the band structure is included within the reciprocal unit cell known as first Brillouin zone (BZ), denoted by the green area in Fig. 2.1(d)

The interaction of the electrons with the non-zero ionic potential splits the energy of the electronic states at the BZ boundaries, opening gaps in the electronic energy spectrum. One can

[1] Because a free electron is described by a plane wave, its wavevector k completely determines also its momentum $\hbar k/\sqrt{2m}$. This has induced in condensed matter physicists the habit of improperly referring to k as momentum. In general, it is not the case, especially if the free electron wavefunction is assumed to have a more complex and realistic form such as a Bloch function

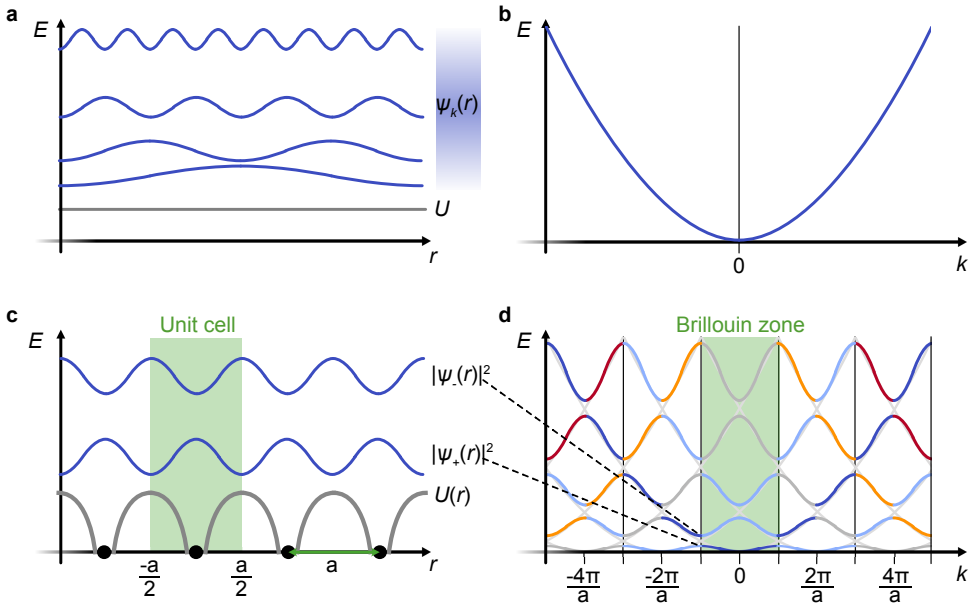

FIGURE 2.1: Schematic of plane wave electronic states $\psi_k(r)$ in an infinite constant potential well U (a) and the associated parabolic energy spectrum (b) considering the free electron model. (c) Turning on the ionic Coulomb potential $U(r)$, gaps at the BZ boundaries are developed in the band structure (d), splitting the degeneracy of the states ψ_- and ψ_+ whose electronic density is illustrated in (c).

intuitively understand this effect by considering the different electronic density of such states ψ_+ and ψ_-. These latter take the form of standing waves resulting from the Bragg scattering of the free electron plane waves with $U(r)$. As shown in Fig. 2.1(c), the maxima of $|\psi_+|^2$ and $|\psi_-|^2$ are localised above and between the ionic potential wells, respectively. Thus, the Coulomb attraction with the lattice is expected to be stronger for ψ_+, resulting in a lower energy compared to ψ_-.

The presence of band gaps in the electronic energy spectrum can directly affect the electrical properties of materials. The Pauli exclusion principle imposes two electrons cannot occupy the same electronic state. Therefore, the bands will be filled with electrons up to a specific energy called Fermi level. In a metal such as copper or gold, the bands are only partially filled. Thus, the conduction electrons at the Fermi level can be easily excited into an unoccupied state and change momentum accordingly to the applied electrical field. In an insulating material, instead, the Fermi level lies in between a gap. In this case, the electrons have to pay a significant amount of energy before being able to reach the first excited state. Although the nearly free electron model provides an intuitive picture of the behaviour of electrons in a solid, it is generally of poor utility for calculating the band structure of real materials. In the next section, a more useful approach is introduced and used to simulate the electronic energy spectrum of ML-$TiSe_2$.

2.2 Tight-binding method

A crystal can be seen as an infinite molecule where the original atomic orbitals overlap, forming wider "molecular" states delocalised over the entire system. This approach is also called tight-binding method because it assumes the electrons are sufficiently tightly bonded to the nucleus that they preserve an atomic-like wavefunction. Thus, the resulting electronic states can be described as a linear combination of atomic orbitals ϕ_i (LCAO):

$$\psi_i = \sum_n^N c_{i,n}\phi_{n,i} \tag{2.6}$$

where the index n runs over the number of atoms in the system N and i denotes the atomic state quantum numbers. In general, the atomic orbitals $\phi_{n,i}$ are not orthogonal when placed at different lattice sites. Still, it is always possible to use the Löwdin's method to transform them into an orthogonal set [37], preserving their symmetries.

When the single atoms are brought together, the overlap between neighbouring orbitals increases, generating electronic states with varying degrees of bonding and anti-bonding character and separated in energy from their original atomic level (on-site energy) as shown in Fig.2.2. In

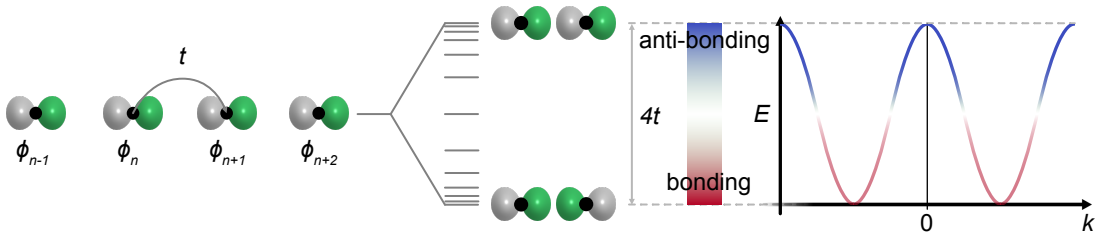

FIGURE 2.2: Schematic of a 1D lattice tight-binding method: the orbitals ϕ in different lattice sites overlap with each others allowing the electrons to hop between adiacent atoms (t denotes the hopping amplitude). The resulting electronic states are formed by superposition of the atomic orbitals with different bonding and anti-bonding character. In the limit of an infinite crystal, such states develop a continuous band having an energy width of $4t$.

the case of an infinite crystal, a continuous spectrum is formed, having a bandwidth proportional to the hopping amplitude between different sites (t). Consequently, a wide band is formed by highly delocalised states, while orbitals that do not significantly overlap generate flatter dispersions. Because the number of states has to be conserved, the number of bands obtained will be equal to the number of atomic orbitals forming the basis of the LCAO. Substituting ψ_i into the Schrödinger

equation 2.4, the energy expectation values become:

$$\sum_{n,m} \frac{c^{\dagger}_{i,m}(k)c_{i,n}(k)\langle\phi_m|H_{el}|\phi_n\rangle}{\langle\phi_m|\phi_n\rangle} = E_i(k) \tag{2.7}$$

where $\langle\phi_m|H(k)|\phi_n\rangle$ is a matrix element of the Hamiltonian describing the hopping between the two atomic sites m and n. Because the system is periodic, the eigenstates take the form of Bloch functions with $u_k(r)$ formed by a linear combination of $\phi_{n,i}$ placed within the same unit cell, while the k-dependent coefficients $c_{i,n}(k)$ can be re-written as $c_i e^{ikna}$, resembling the complex factor e^{ikr} in eq. 2.5.

Slater and Koster introduced an approximated solution for the integral $\langle\phi_m|H(k)|\phi_n\rangle$ considering the different type of chemical bonding (σ, π, δ, etc...) between ϕ_n and ϕ_m [38]. For instance, the integral $\langle p_y(r_A)|H_{el}|p_y(r_B)\rangle$ between the p_y atomic orbitals on two different lattice sites (A,B) can be decomposed in two components describing the overlap in a σ and π bonding as shown in Fig. 2.3. Therefore the matrix element depends only on the parameters $V_{pp\sigma}$ and $V_{pp\pi}$, while θ is known from the crystal structure. However, such parameters vary from one material to another, and they need to be extracted by other more complex $ab-initio$ calculations, such as density functional theory (DFT) or by fitting to the band structure measured with ARPES. In the next section, the band structure on ML-$TiSe_2$ is simulated using the Slater Koster model reported in [39].

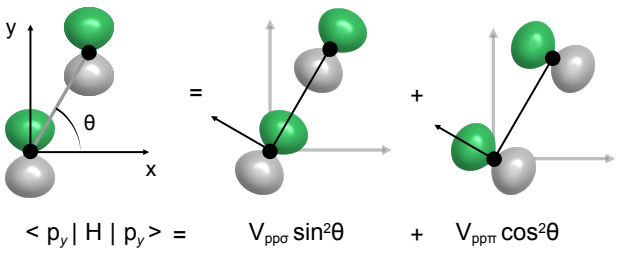

FIGURE 2.3: Decomposition of the integral $\langle p_y(r_A)|H|p_y(r_B)\rangle$ into two components representing the σ and π bonding configuration. $V_{pp\sigma}$ and $V_{pp\pi}$ denotes the Slater-Koster parameters used as input in the calculation.

2.2.1 Tight-binding of monolayer $TiSe_2$

In this section, the band structure of monolayer (ML) $TiSe_2$ is calculated as a practical example of the Slater-Koster tight-binding method and to get familiar with the typical electronic energy spectrum of Ti-based dichalcogenides. This material consists of a triangularly packed layer of Ti

atoms sandwiched between two Se layers as shown in Fig. 2.4(a). Each Ti atom is surrounded by six chalcogenides forming a local octahedral structure rotated by 60° with respect to the out-of-plane crystallographic axis. This crystal structure presents a three-fold axis perpendicular to the lattice plane denoted by the black triangle and a mirror plane (m) perpendicular to a two-fold axis (C_2) crossing each other at the Ti site, generating an inversion point at the centre of the octahedron. The three fold symmetry also produces other two m and C_2 symmetry elements rotated 120° with respect to the ones illustrated in Fig. 2.4(a).

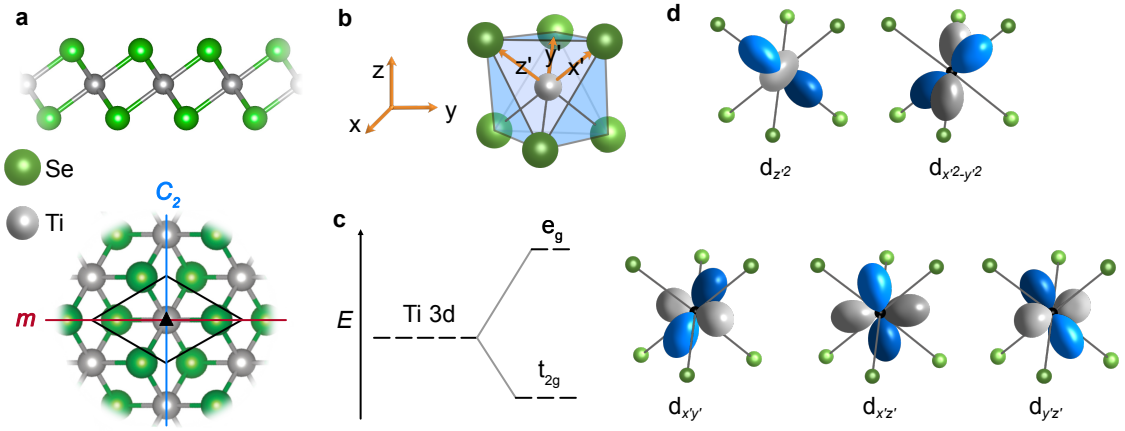

FIGURE 2.4: (a) Side and top view of ML-$TiSe_2$ crystal structure in its undistorted phase. The red and blue lines denotes the mirror plane m and the two-fold axis C_2, respectively, while the unit cell is shown in black. The three fold axis perpendicular to the lattice plane in denoted by a black triangle. (b) Rotated $\{x'y'z'\}$ coordinate frameworks used to define the orbital basis illustrated in (d). (c) Crystal field splitting of the Ti $3d$ orbitals in the double degenerate e_g states (d top) and triple degenerate t_{2g} states (d bottom).

A first effect on the atomic energy levels induced by the vicinity of other atoms can be intuitively understood using a simple classical argument. The electrons around the Ti site are expected to feel an electrostatic Coulomb repulsion from the surrounding Se electron clouds, which significantly increases the on-site energy of the Ti orbitals pointing towards the ligands with respect to the others pointing towards the edges of the octahedron. Therefore, it is useful to adopt an orbital basis that resembles the rotated octahedral structure, for example by defining the atomic orbitals in the rotated coordinate framework $\{x'y'z'\}$ shown in Fig. 2.4(b). In such configuration, the crystal field splitting of the Ti $3d$ orbitals into e_g states ($d_{x'^2-y'^2}$, $d_{3z'^2}$) and t_{2g} orbitals ($d_{x'y'}$, $d_{y'z'}$, $d_{x'z'}$) directly derives from the orbital shape illustrated in Fig. 2.4(c). Moreover, the in-plane threefold symmetry of the system is naturally represented as reflected onto the Se $4p$ orbitals p $\{p'_x, p'_y, p'_z\}$ that point directly toward the Ti atom. Considering the geometry of the system, one would expect the Se p orbitals to generate strong σ bonds with the Ti e_g orbitals and predominant π-type bonds with the other t_{2g} states.

A good approximation of the low energy band structure can be obtained by considering only the hopping between the five Ti $3d$ and three Se $4p$ orbitals for both chalcogenides in the unit cell, resulting in an energy spectrum formed by a total of $5 + 3 \cdot 2$ bands without counting the spin degeneracy. The electronic energy levels are calculated from eq. 2.7 substituting the matrix element with the Slater-Koster parametrised formulas tabulated in Ref. [38]. In order to reduce the computational cost, the summation can also be truncated including only the hopping between the next nearest neighbours.

Fig. 2.5(a) shows the resulting band structure calculated along the high symmetry direction $\Gamma - M$ and $\Gamma - K$ using the hopping parameters reported in Table 2.1. The six Se $4p$ derived bands (green) are fully occupied resembling the closed shell electronic configuration of the chalcogenide ion, while just above the Fermi level the Ti $3d$ are largely split in t_{2g} and e_g manifolds. A small indirect gap of only $\sim$ 170 meV separates in energy the Se valence band maximum at Γ and the conduction band bottom at M that mainly derives from Ti $3d_{x'y'}$. As shown in Fig. 2.5(b), the other elliptical electron pockets at the other M points derive from the other two t_{2g} states resembling the three-fold symmetry that relates these orbitals. Thus, the octahedral basis allows to efficiently decouple the orbital contribution of each conduction pocket. We will see in chapter 4 how this choice largely facilitates the interpretation of the band hybridisation occurring at the charge density wave (CDW) transition in ML-$TiTe_2$.

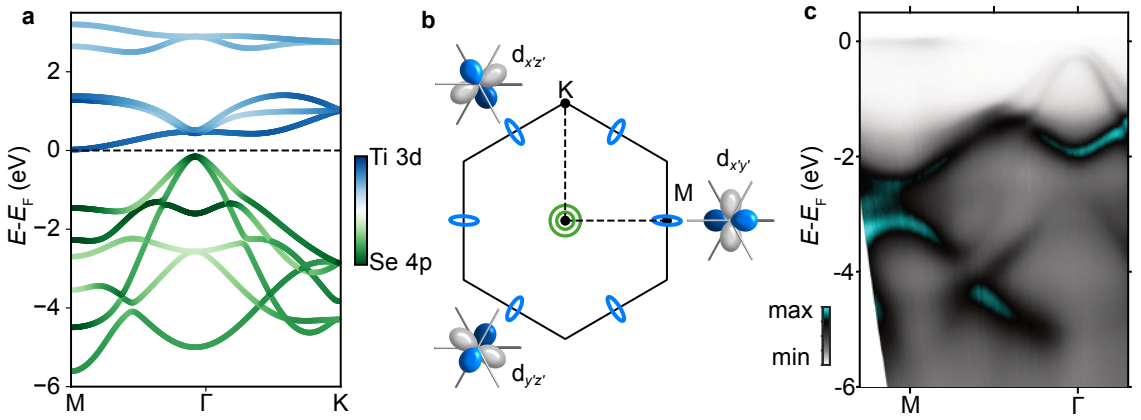

FIGURE 2.5: (a) Tight-binding band structure of ML-$TiSe_2$ without SOC in its undistorted phase. (b) BZ of ML-$TiSe_2$ showing the valence band top at Γ (green) and the conduction band bottom (blue) at M derived by the three Ti t_{2g} orbitals in the rotated octahedral basis. (c) Experimental ARPES band structure of ML-$TiSe_2$ measured at T=290 K; adapted from Ref. [39].

The orbital character of the valence bands is instead more efficiently described by defining the Se $4p$ orbitals in the conventional crystallographic coordinates $\{x, y, z\}$. Because the p states have

TABLE 2.1: Tight-binding parameters for ML-$TiSe_2$ adapted from [39]

On-site energies (eV)		
$e(p)$ = -2.216	$e(d\epsilon)$ = 0.24	$e(d\gamma)$ = 1.352
Hopping parameters (eV)		
$t(pp\sigma)_1$ = 0.709	$t(pp\sigma)_2$ = 0.592	$t(pd\sigma)$ = -1.422
$t(pp\pi)_1$ = -0.103	$t(pp\pi)_2$ = -0.009	$t(pd\pi)$ = 0.797
$t(dd\sigma)$ = -0.347	$t(dd\pi)$ = 0.119	$t(dd\delta)$ = -0.030

axial symmetry, the conversion between the two orbital basis is directly described by the following rotational matrix [40]:

$$\begin{pmatrix} p_{x'} \\ p_{y'} \\ p_{z'} \end{pmatrix} = \begin{pmatrix} \frac{1}{\sqrt{6}} & \frac{-1}{\sqrt{2}} & \frac{1}{\sqrt{3}} \\ \frac{1}{\sqrt{6}} & \frac{1}{\sqrt{2}} & \frac{1}{\sqrt{3}} \\ \frac{-2}{\sqrt{6}} & 0 & \frac{1}{\sqrt{3}} \end{pmatrix} \begin{pmatrix} p_x \\ p_y \\ p_z \end{pmatrix} \tag{2.8}$$

The top of the valence band derives from anti-bonding p_x and p_y states having a large in-plane hopping. Instead, the p_z orbitals are expected to overlap less since they have a node within the plane. Therefore, the energy dispersion of the p_z-derived states in the monolayer compound is strongly reduced, resulting in a flatter band confined at -1.5 eV at Γ. Our calculations are in good agreement with the occupied band structure of ML-$TiSe_2$ measured with ARPES at T=290 K shown Fig. 2.5(c). However, two qualitative differences can be found. Experimentally, a small electron pocket is visible below the Fermi level at M, while it is entirely unoccupied in our calculation. Such n-type doping can derive from the Se vacancies inevitably formed during the crystal growth and from a weak charge transfer induced by the coupling with the substrate. The simulation can be corrected by simply shifting the Fermi level of a few meV in order to have a better agreement with the ARPES data. A second difference can be identified at Γ where the top of the valence band is degenerate in our simulation while they are split by ~ 200 meV in the experimental data. This is a well know phenomenon induced by the interaction between the orbital angular momentum of the electron and its spin, causing a further split in the atomic energy levels, which in turn is inherited by the tight-binding wavefunction.

2.3 Spin-orbit coupling

The interaction between the orbit of the electrons and their spin, i.e., spin-orbit coupling (SOC) occurs in all elements determining the fine structure of their energy spectrum. This phenomenon can be qualitatively understood considering the oversimplified classical picture of an electron orbiting in the isotropic nuclear potential $U(\boldsymbol{r})$. In its rest coordinate framework, the electron experiences an effective magnetic field:

$$\mathbf{B} = \frac{\boldsymbol{E} \times \boldsymbol{v}}{c^2}, \quad with \quad \boldsymbol{E} = -\frac{\boldsymbol{r}}{r}\frac{\delta U}{\delta r} \tag{2.9}$$

where $\boldsymbol{v}$ denotes the electron tangential velocity, c the speed of light. Since the angular momentum of the electron is given by $\boldsymbol{L} = m_e \boldsymbol{r} \times \boldsymbol{v}$, equation above can be rewritten as:

$$\boldsymbol{B} = -\frac{1}{m_e r c^2}\frac{\delta U}{\delta r}\boldsymbol{L} \tag{2.10}$$

The intrinsic spin angular momentum of the electrons **S** can interact with such magnetic field as an effective Zeeman effect. Thus, the Hamiltonian term describing the spin-orbit coupling takes the form of:

$$H_{SOC} = -\boldsymbol{\mu} \cdot \boldsymbol{B} = -\frac{1}{2}\frac{e}{2m_e^2 r c^2} g \frac{\delta U}{\delta r}\boldsymbol{S} \cdot \boldsymbol{L} \tag{2.11}$$

where $\boldsymbol{\mu} = \frac{e}{2m_e} g \boldsymbol{S}$ is the magnetic moment related to the electron spin and g is the electron g-factor ~ 2. In eq. 2.11 a corrective factor of $1/2$ is included to take into account the relativistic kinematic effect called Thomas precession. Noticeably, this new Hamiltonian term does not commute anymore with orbital and spin angular momentum operators. Thus, it is useful to introduce the total angular momentum $\boldsymbol{J}$ defined as $\boldsymbol{J} = \boldsymbol{L} + \boldsymbol{S}$ for which $[\hat{H}_{SOC}, \hat{J}] = 0$. Spin-orbit coupling promotes the mixing of energy levels with different $\boldsymbol{L}$ and $\boldsymbol{S}$, which are split in energy according to their total angular momentum. For instance, in Fig.2.6(a) the SOC splitting of the atomic p manifold into two degenerate levels characterised by total angular momentum quantum number $j = 1/2$ (double degenerate) and $j = 3/2$ (fourfold degenerate) is shown. Because the expectation value $< \phi|\frac{\delta U}{\delta r}|\phi >$ is proportional to Z^4, the magnitude of such splitting is stronger for heavier atoms such as Se and Te compared to the lighter Ti.

To include SOC in our calculation only for the Se p manifold, eq. 2.11 can be re-written in the following matrix representation using the Se $3p$ basis $\{px\uparrow, px\downarrow, py\uparrow, py\downarrow, pz\uparrow, pz\downarrow\}$:

$$H_{SOC} = \frac{\lambda}{2}(L_x\sigma_x + L_y\sigma_y + L_z\sigma_z) = \frac{\lambda}{2}\begin{pmatrix} 0 & 0 & -i & 0 & -i & 0 \\ 0 & 0 & 0 & i & 0 & 1 \\ i & 0 & 0 & 0 & 1 & 0 \\ 0 & -i & 0 & 0 & 0 & i \\ i & 0 & -1 & 0 & 0 & 0 \\ 0 & 1 & 0 & -i & 0 & 0 \end{pmatrix} \tag{2.12}$$

where σ_{xyz} denotes the Pauli matrices. Fig. 2.6(b-c) show a comparison between the resulting low energy band structures of ML-$TiSe_2$ neglecting and including SOC, respectively. At Γ, the Se $4p_x$ (red) hybridises with the $4p_y$ (green)-derived states splitting the degeneracy of the valence band top by opening a sizeable gap of ~ 200 meV. Similar effects are also visible at the crossing point with the Se $4p_z$ band at ~ -1.5 eV. Moreover, the indirect gap between the electron and hole pockets is now reduced to only ~ 70 meV. Therefore, spin-orbit coupling should be included in the calculation in order to achieve a realistic description of the low energy band structure of ML-$TiSe_2$. So far, I have assumed the atoms in ML-$TiSe_2$ frozen in their normal state equilibrium

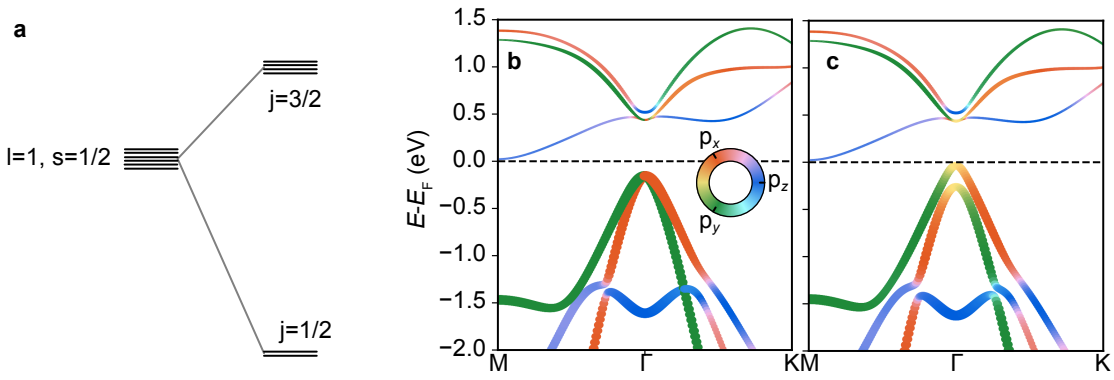

FIGURE 2.6: (a) Spin-orbit splitting of the atomic p states into two manifold characterised by different total angular momentum quantum number j. Tight-binding band structure of ML-$TiSe_2$ with (b) and without SOC (c); the color map represents the band character derived from the Se $4p$ orbital defined in the coordinates $\{x, y, z\}$.

positions. However, below ~ 220 K its atomic structure distorts with the emerging of a charge density wave phase in which the electronic states are strongly coupled with the lattice vibrational modes. Before diving into the CDW mechanism, a basic description of such vibrational modes is therefore essential.

2.4 Lattice dynamics

A lot of properties of materials can be described by decoupling the lattice and electronic motions accordingly to the adiabatic approximation introduced above. However, the lattice dynamics underpins very common phenomena such as the propagation of sound waves in solids, how the resistivity of metals changes with the temperature and even more exotic properties like superconductivity and CDW instabilities.

2.4.1 Simple model: the diatomic 1D chain

A simple but instructive model, the diatomic 1D chain, provides the basic concepts for a qualitative understanding of the lattice vibration in complex materials. In first approximation, a 1D infinite lattice with two atoms per unit cell having masses M_1 and M_2 can be considered as a chain of rigid balls (atoms) connected with springs (bonding electrons) as illustrated in Fig. 2.7(a). For small displacements, the forces acting on the atoms can be approximated using the classical elastic Hook law (harmonic approximation), causing the atoms to oscillate around their rest positions. The lattice vibrations can be decoupled into orthogonal harmonic modes called phonons which are mathematically described by plane waves propagating in the lattice having wavevector k and frequency ω. Similar to the nearly free electronic states, the energy of these phonon modes can be represented with a dispersion relation formed by vibrational bands periodic in the reciprocal space. In general, the number of phonon bands is equal to the number of translational degrees of freedom (3 assuming the atoms can vibrate along all the x, y, z directions) times the number of atoms in the unit cell (2 in this case). Fig. 2.7(c) shows a typical phonon spectrum of such a system comprised of four bands, two of them having a double degeneracy for a total of six bands as expected. The normal modes are clearly divided in energy into two branches. The low energy branch goes to zero frequency at small q and describes the mechanical waves (sound) propagating in the material characterised by modes where the two atoms inside the same unit cell vibrate in phase as shown in Fig. 2.7(b). For this reason, it takes the name of acoustic branch. Instead, the higher energy branch with $\omega(0) \neq 0$ is characterised by atoms within the same unit cell vibrating out of phase. These modes are also known as optical branches: if the two ions have opposite charges, the motion can create a vibrating dipole that can strongly couple with infrared light. Each branch can be split further into one longitudinal (LA and LO) and two degenerate transverse branches (TA and TO). The vibrational normal modes introduced here are a complete orthogonal

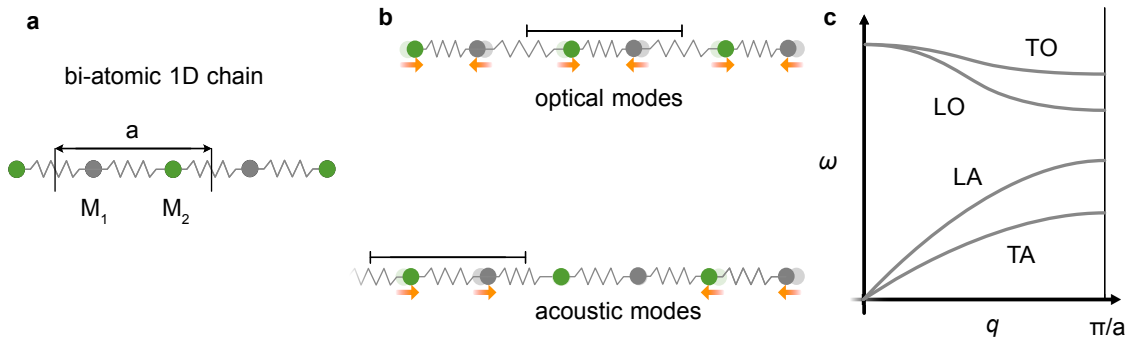

FIGURE 2.7: (a) 1D lattice with two atoms per unit cell having masses M_1 and M_2 connected with springs representing their recoil forces. (b) Representation of an optical and acoustic phonon mode characterised by an out-of-phase and in-phase atomic distortion (orange arrow) within the unit cell (black line). Typical phonon spectrum of the ideal system in (a), showing the optical (O) and acoustic (A) branches further split in longitudinal (L) and transverse (T) modes.

basis describing the periodic displacements of the atoms in the system. Thus, also the periodic lattice distortion induced by the CDW transition can be ultimately decoupled onto such a basis.

2.4.2 Phonons in ML-$TiSe_2$

Here, the phonon band structure of ML-$TiSe_2$ is analysed, showing the characteristic signature of its lattice instability. The phonon spectrum of free-standing ML-$TiSe_2$ was calculated by Dr. Warda Rahim at University College London using finite-displacement method (FDM) [41, 42] within the harmonic approximation. The electronic density is first calculated including SOC with *ab-initio* DFT method assuming the atoms at rest in their equilibrium positions. Then, the atoms are displaced accordingly with certain symmetric schemes, generating non-zero internal restoring forces in the crystal. These latter are analysed to extract information about the lattice dynamics and, therefore, to calculate the phonon energies along certain high-symmetry directions. More details on the computational method can be found in [43]. Fig. 2.8(a) shows the resulting phonon spectrum along the K-Γ-M path comprised of nine vibrational bands, as expected. The three acoustic modes are well recognisable at Γ since they assume $\omega = 0$, with the longitudinal branch having the highest energy among the three. The transverse mode characterised by an out-of-plane atomic vibration (ZA) is particularly affected by the reduced dimensionality in the monolayer. The missing elastic coupling with the absent layers above and below the plane significantly reduces the ZA mode frequencies.

The other six optical branches having finite energies at Γ can be categorised following their specific symmetry. A schematic representation of their atomic vibration in the local octahedral

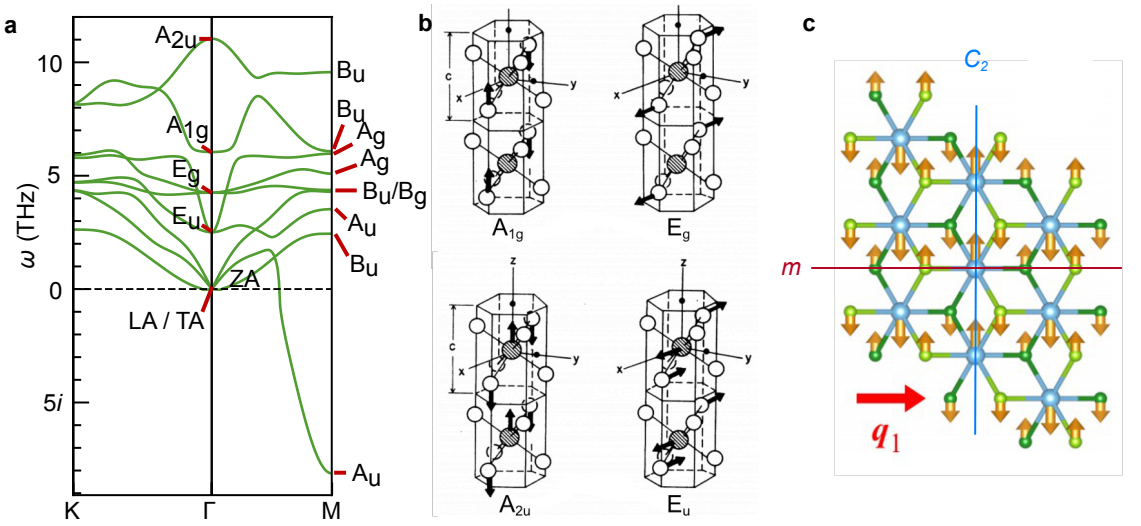

FIGURE 2.8: (a) DFT phonon band structure of ML-$TiSe_2$ along the K-Γ-M path where the irreducible representation of the vibrational modes at Γ and M are indicated. (b) Schematic of the optical phonon modes at Γ, adapted from Ref. [44]. (c) Schematic of the soften phonon at M with A_u symmetry which is odd in the mirror plane m, but even in the C_2 axis; adapted from [40].

structure is shown in Fig. 2.8(b), where the typical out-of-phase motion of the atoms within the same unit cell is well recognisable. However, such symmetry representation is valid only along specific high symmetry direction in the BZ, and away from them, their character can mix, opening gaps at the band crossing. Interestingly one of the phonons assumes imaginary frequencies around M. This transverse phonon belongs to an irreducible representation called (A_u) that is symmetric with respect to the two-fold rotation axis (C_2), but antisymmetric in the mirror plane (m). It is helpful to think about a plane wave with an imaginary frequency as a damped oscillation with an exponential decay time equal to $1/\omega$. Thus, the atomic motion doesn't oscillate anymore. Instead, the atoms freeze into their displaced positions after a time much longer than $1/\omega$. In general, it means the original lattice configuration is unstable and prefers to distort to minimise its free energy. In $TiSe_2$, the lattice instability predicted by the phonon calculation is the signature of atomic distortion induced in its CDW ground state.

2.5 Screening and the Lindhard susceptibility

The charge density of the valence electrons can strongly influence the interatomic potential and, therefore, the phonon dynamics. In extreme cases, the coupling between these two subsystems can promote collective ground states such as CDW where the electron-hole pairing is mediated by phonons. However, as discussed in Sec. 2.1, treating interacting particles is not an

easy task in quantum mechanics, and therefore, one tends as much as possible to describe the system within the single electron approximation. Even within this simplified framework, phenomena deriving from electron-electron coupling, such as the screening of the ionic potential, can be, in any case, described by adopting the mean field approximation. As already briefly mentioned in Sec. 2.1, the nucleus potential is largely screened by the deep core electrons, but also the valence electrons delocalised over the entire crystal can contribute to such screening. Intuitively, the valence electron density is able to rearrange itself in order to partially cancel out the ionic Coulomb potential. Let's consider a particle with charge Ze immersed into an independent electron gas with density n as shown in Fig. 2.9(a). In a semiclassical approximation, the long-range Coulomb potential $U(r) = \frac{-Z}{r}$ would be screened by the delocalised electrons in space as [33]:

$$U(r) = \frac{-Z}{r} e^{-k_{TF} r} \tag{2.13}$$

where k_{TF} is known as Thomas-Fermi screening wavevector. $U(r)$ is therefore scaled by an exponential factor having a decay rate equal to $1/k_{TF}$. It can be shown that k_{TF} is proportional to $n^{-1/6}$. Thus, the more electrons participate in the screening, the faster $U(r)$ will fall. For instance, the Thomas-Fermi screening length $1/k_{TF}$ in copper (Cu) is 0.55 Å [33], which is smaller than the interatomic distance. The valence electrons are, therefore, very efficient in screening the ionic Coulomb potential, and they can impart a strong renormalisation not only on the electron-lattice but also on the ion-ion interaction that ultimately determines the phonon spectrum.

In general, the response function of the electrons to an external field U_{ext} is described by the electronic susceptibility $\chi(q)$ as:

$$\delta\rho(q) = \chi_0(q)U(q) + \chi'(q)U(q)^2 + \chi''(q)U(q)^3 ... \tag{2.14}$$

For small external field the Taylor expansion can be truncated at the linear term χ_0 that links the Fourier components of the screening electron density $\delta\rho(q)$ to the Fourier transform of the total potential $U(q) = U^{ext}(q) + \delta U(q)$, where $\delta U(q)$ is the potential formed by the induced electronic screening density $\delta\rho$. Treating $U(q)$ as a first-order perturbation on the free electron Hamiltonian, Lindhard derives the following expression for χ_0 [32]:

$$\chi_0(q) = \sum_k \frac{f(E_k, T) - f(E_{k-q}, T)}{E_k - E_{k-q}} \tag{2.15}$$

where $f(E_k, T)$ is the Fermi-Dirac distribution representing the probability that the energy level E_k is occupied at a certain temperature T. Fig. 2.9(b) shows χ_0 calculated for a 3D electron gas. For q much smaller than two times the Fermi momentum (k_F) the electrons screen efficiently the long wavelength Fourier components of $U_{ext}(q)$ resembling the result obtained within the semi-classical Thomas-Fermi approximation. However, for perturbation with $q >> 2k_F$, the electron is unable to screen the external field that is expected to permeate into the electron cloud for a longer distance. Such a drop in the electronic response function can be understood by noting that in eq. 2.15 the main contribution to susceptibility comes from states close to the Fermi surface, where the probability to scatter from an occupied state k to an unoccupied state $k+q$ is maximised. For $q \sim 2k_F$, only the few states at diametrically opposite sides of the Fermi sphere are connected by the vector q causing a logarithmic decrease in the response function that develops a singularity in its first derivative at exactly $q = 2k_F$. However, for larger q there are no more states at the Fermi level able to accept the scattered electron as illustrated in the insets of Fig. 2.9(b), and the screening efficiency rapidly drops to zero.

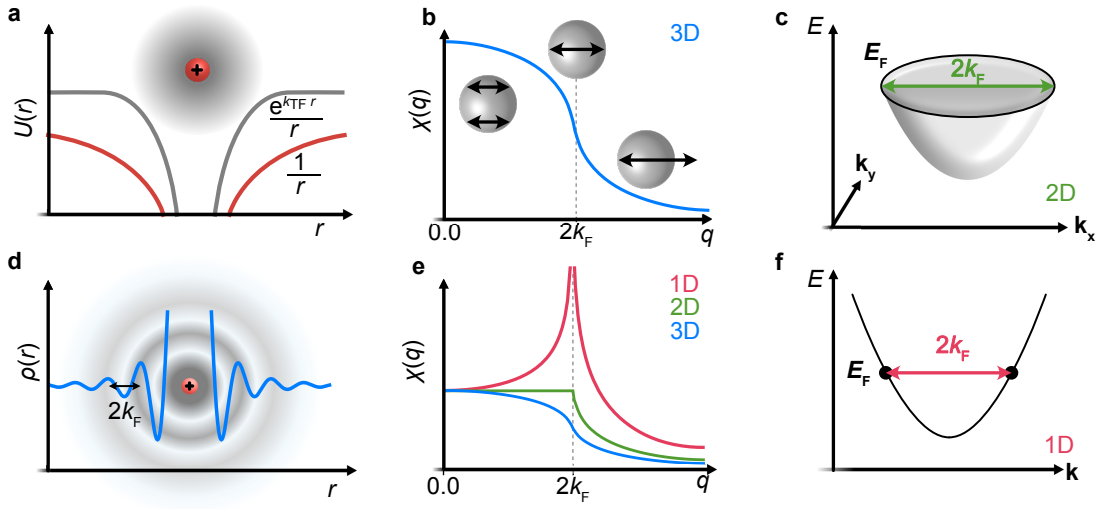

FIGURE 2.9: (a) Coulomb potential $U(r)$ (red line) generated by a positive charge (red dot) immersed in a Fermi sea and the screening induced by the electrons resulting in an exponentially decay of the original potential (grey line) in the Thomas Fermi approximation. (b) Lindhard susceptibility $\chi(q)$ for a 3D electron gas with the q vector (black arrows) connecting part of the Fermi surface represented by gray spheres. (c) Circular Fermi surface for a 2D free electron gas. (d) Friedel oscillations of the electron density $\rho(r)$ around a charged impurity. (e) comparison between the Lindhard susceptibility for a 3D, 2D, 1D free electron gas. (f) Perfectly nested Fermi surface of a 1D free electron gas.

Such a step in the response function has strong implications in reshaping the charge density in a way not predicted by the Thomas-Fermi approximation. Indeed, it can be shown that for $r >> 0$,

the induced charge density decays as a damped oscillation with a wavelength equal to $1/(2k_F)$:

$$\delta\rho \sim A_0 cos(2rk_F)/r^3 \tag{2.16}$$

Such long range oscillation in the charge density illustrated in Fig. 2.9(d), also called Friedel oscillations, has been observed experimentally on the surface of metallic materials in the proximity of point defects [45]. Nowadays, such phenomenon is exploited for measuring the Fermi surface of several materials by measuring their Friedel oscillation period using scanning probe microscopy.

It is now clear how the Fermi surface plays an important role in reshaping the induced charge density by dictating the probability of electron scattering. This effect is even amplified by reducing the dimensionality of the system to 2D and 1D free electron gases for which the respective Fermi surfaces assume a circumference and point-like shapes, respectively (Fig. 2.9(c, f)). These different Fermi surface topologies significantly increase the fraction of states linked by the same nesting vector, enhancing the singularity in χ_0. While in 2D, χ_0 develops a sharp step at $q = 2k_F$ (Fig 2.9(e)), in the 1D case, the susceptibility diverges at T=0 K due to the perfect nesting in the point-like Fermi surface. Thus, a very weak periodic perturbation in the Coulomb potential with $q = 2k_F$ is expected to induce a dramatic response on the 1D electron cloud. We will see in the next section how such quantum behaviour of the electrons underpins the charge density wave formation in a 1D electron gas.

2.6 Peierls distortion

The first theoretical description of a CDW instability was provided by Peierls [46] and Fröhlich [47] back in the 1930s when they predicted that a 1D metal undergoes a lattice distortion at low temperatures leading to a new insulating ground state characterised by a periodic modulation of the charge density, i.e., a charge density wave. Their model considers a 1D atomic chain with one atom per unit cell and lattice constant a as sketched in Fig. 2.10(a). If each atom contributes with one electron, E_F crosses the band at half of the first BZ resulting in a metallic system. As described in the previous section, the Lindhard electric susceptibility of the system at T=0 K has a singularity $q = 2k_F$, due to the perfect nesting of the 1D point-like Fermi surface. Such massive response of the 1D electronic system makes the metallic state unstable under an infinitesimally weak periodic perturbation in the Coulomb potential with $q = 2k_F$, inducing a modulation with the same periodicity in the electron cloud itself. This new periodicity leads to a larger unit cell in

the direct space and, therefore, a smaller BZ in the reciprocal space. Because of this periodicity in the reciprocal space, the original bands are backfolded into the new BZ where they cross with each other at the BZ boundary. However, the presence of the new periodic potential splits the degeneracy of these states, opening an energy gap at the Fermi level that leads to a metal to insulator transition and the lowering of the electronic total energy.

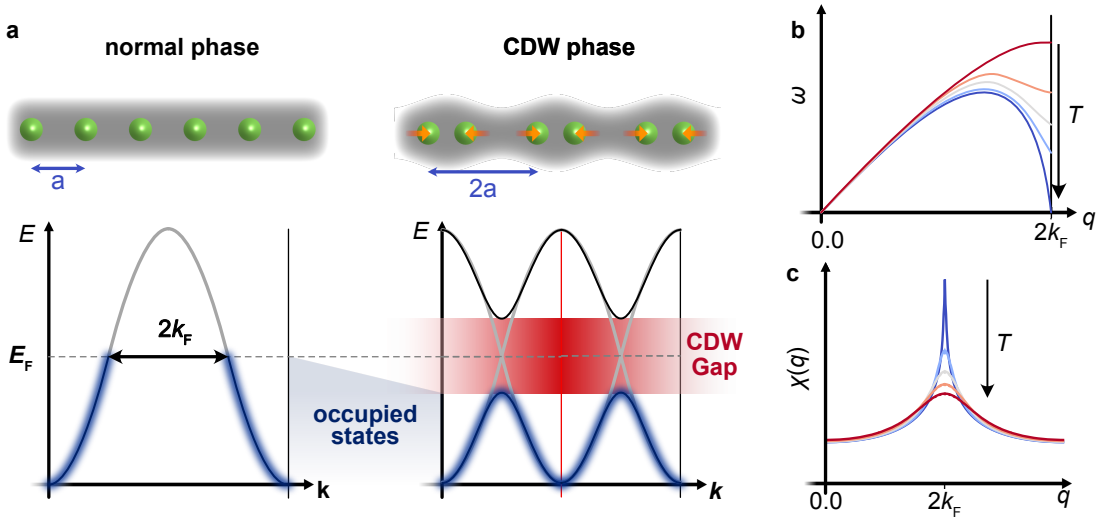

FIGURE 2.10: Peierls distortion in 1D metallic chain. (a) Schematics of a 1D lattice and its band structure undergoing a charge density wave transition which leads to a lattice distortion (orange arrows) and the opening of a CDW gap at k_F. (b) Softening of the phonon mode at $q = 2k_F$ at low temperatures. (c) Temperature-dependent Lindhard susceptibility $\chi(q)$ of the system in (a) in its normal phase.

So far, the ionic lattice has been neglected for simplicity, but it has to be taken into consideration in order to achieve a more realistic description of the phase transition. As described in the previous section, the valence electrons are very efficient in screening a periodic perturbation with $q = 2k_F$ in $U(r)$. Such perturbation can be easily provided by a phonon mode having the appropriate wavevector. The screening is expected to drastically reduce the internal restoring forces between the ions and consequently lower the phonon frequency, as shown in Fig. 2.10(b). This coupling between the electrons at the Fermi level and the phonon with $q = 2k_F$ is also known as Kohn anomaly [48]. As the peak in χ_0 becomes sharper at lower temperatures (see Fig. 2.10(c)), the effect of the electronic screening on the phonon spectrum becomes more pronounced until the soft mode frequency reaches zero energy. At this point, this specific atomic vibration is completely frozen-in, displacing the atomic rest position into a new periodic configuration.

The phenomenology of the CDW transition discussed so far can be microscopically described using the so-called Frölich hamiltonian [49]:

$$H = \sum_k E_k a_k^\dagger a_k + \sum_k \hbar\omega_q b_q^\dagger b_q + \frac{1}{\sqrt{N}} \sum_{k,q} g_q a_{k+q}^\dagger a_k (b_{-q}^\dagger + b_q) \tag{2.17}$$

The first term denotes the total electron energy using the creation $a_k^\dagger$ and annihilation a_k operator for the electronic state k; the second term describes the total energy of the lattice summing over the energy of each phonon $\hbar\omega_q$ times the creation $b_k^\dagger$ and annihilation b_k operator of the phonon mode q. The last term represents two processes: scattering of an electron from k to $k+q$ by (i) annihilation (=absorption) of a photon with momentum q or by (ii) creation (=emission) of a phonon with momentum $-q$. The parameter g_q is the electron-phonon coupling strength that generally depends on q. In the weak electron-phonon coupling limit (the lattice distortion is much smaller than the lattice constant), the theory takes the same mathematical form of the BCS theory describing the conventional superconductivity where electron-electron pairing is mediated by electron-phonon coupling. This similarity is not surprising since a CDW phase can also be seen as an instability of the Fermi sea resulting in a coherent quantum ground state achieved by condensation of electron-hole pairs mediated by electron-phonon coupling. Within this theoretical framework, it can be shown that the energy gain (δE_e) induced by the band gap opening in the electronic spectrum and the elastic energy cost (δE_l) due to the lattice distortion has the following forms [50]:

$$\delta E_e = -|g_{q_0} u_0 \sqrt{\frac{2M\omega_{q_0}}{\hbar}}|^2 \chi(q_0) \tag{2.18}$$

$$\delta E_l = \frac{1}{2} M \omega_{q_0}^2 u_0^2 \tag{2.19}$$

where u_0 is the amplitude of the atomic displacement. Thus, the CDW phase will be stable when $\delta E_e > -\delta E_l$, which in turns can be expressed in terms of microscopic parameters as:

$$\frac{4g_{q_0}^2}{\hbar\omega_0} > \frac{1}{\chi(q_0)} \tag{2.20}$$

For a non-interacting 1D electron gas with a non vanishing electron-phonon coupling, this last relation is always satisfied because $\chi(q_0) \longrightarrow \infty$ at T=0 K. However, at higher temperatures, the singularity in electronic susceptibility is relaxed to a peak having a maximum finite value of $\chi(q_0, T) = \frac{1}{2} N(0) ln(\frac{2.28 E_F}{k_B T})$, where $N(0)$ is the density of states at the Fermi level in the normal

phase. Substituting $\chi(q_0, T)$ in eq. 2.20 an estimate of the critical temperature is readily extracted:

$$k_B T_c = 2.28 E_F \, exp(-\frac{\hbar\omega_{q_0}}{2g_{q_0}^2 N(0)}) \tag{2.21}$$

T_c can be further related to the CDW electronic gap at T=0 K using the well known BCS relation valid in the weak coupling regime:

$$\frac{2\Delta(0)}{k_B T_c} = 3.52 \, . \tag{2.22}$$

The CDW phase in materials with strong electron-phonon coupling (but still within the approximation that the lattice distortion is much smaller than the lattice constant) is expected to be stable at high temperatures and have a relatively large CDW gap in their energy spectrum. However, there are several factors that limit the applicability of the Peierls model to real materials. Repulsive interactions between the electrons, such as Coulomb repulsion and exchange coupling, tend to spread the electrons further apart, limiting the amplitude of electron cloud modulation in the CDW phase [50]. Geometrical deviation from a perfectly nested Fermi surface, which is always the case in real materials, significantly reduces the singularity in χ [51], limiting the electronic energy gain δE_e in eq. 2.18. Several studies revealed this model is neither suitable to describe the lattice distortion expected in a free-standing 1D alkaline metal chain [51, 52]. Thus, a realistic theoretical framework describing the CDW transition that can be transferable across a wide range of materials is still missing. Although its theoretical complexity, CDW instability is a quite common phenomenon observed in a wide range of materials such as quasi-1D material inorganic and organic crystals (e.g. $K_{0.33}MoO_3$ and TTF-TCNQ, respectively) [53, 54]. CDW-like phases also emerge in several 2D (monolayer), quasi 2D (bulk) TMDs or cuprate superconductors, where the interesting competition or coexistence between CDW and superconductivity still drives a rich scientific research.

2.7 CDW in TMDs

Transition metal dichalcogenides are one of the most studied CDW materials since the 1970s when anomalies in their electronic properties were first observed and associated with the emergence of satellite peaks in their diffraction pattern, denoting the onset of a lattice distortion at low temperatures [12]. An overview of the wide range of CDW phases in different TMDs is

shown in table 2.2 where the critical temperatures and the periodicity of their lattice instabilities are reported. If the distorted unit cell is not an integer multiple of the undistorted lattice, a incommensurate (IC) or nearly-commensurate (NC) CDW super-lattice is obtained such as in 2H-$NbSe_2$ (bulk), 1T-TaS_2 and 2H-$TaSe_2$. In group-V TMDs such as 1T-VSe_2, 2H-$NbSe_2$, 1T-TaS_2, 2H-$TaSe_2$ the d-derived conduction band is only partially filled, resulting in a metallic system where CDW instabilities are most likely to occur.

	Bulk	Monolayer
1T-VSe_2 [55]	110 K $(4 \times 4 \times \sim 3)$	140 K $(\sqrt{7} \times \sqrt{3})$
2H-$NbSe_2$ [56]	35 K NC (3×3)	145 K (3×3)
2H-$TaSe_2$ [57]	122 K (IC)	133 K
	90 K (3×3)	–
1T-TaS_2 [50]	543 K (IC)	–
	350 K (NC)	–
	183 K $(\sqrt{13} \times \sqrt{13})$	–
1T-$TiSe_2$ [58]	200 K $(2 \times 2 \times 2)$	232 K (2×2)

TABLE 2.2: CDW critical temperature for bulk and monolayer TMDs and the type of distortion established below it: commensurate $(n \times n)$; nearly commensurate (NC); incommensurate (IC).

The phase diagram of 1T-$TaS_{2(1-x)}Se_{2x}$ alloys is particularly rich in CDW phases showing critical temperatures well above room temperature [59] (Fig. 2.11(a)). For $x = 0$ the system has $(\sqrt{13} \times \sqrt{13})$ commensurate CDW ground state characterised by a concomitant Mott insulating phase. However, the Mott gap is small and is believed to have a negligible effect in stabilising the charge ordering [50]. Here, the lattice distortion takes the form of a breathing mode around one of the Ta sites with a David-star configuration, as shown in Fig. 2.11(b). Above 180 K a nearly commensurate (NC) phase emerges, where undistorted boundaries separate commensurate domains. At even higher temperatures, an additional ICCDW phase (not shown in the phase diagram) where the David-star domains are even more separated remains stable up to 550 K. Substituting S with Se, the CCDW (Mott insulator) phase is suppressed in favour of a superconducting dome with a maximal T_c up to $\sim$ 5 K, but a strong $(\sqrt{13} \times \sqrt{13})$ CCDW phase re-emerges for composition close to pure 1T-$TaSe_2$.

This latter compound can also crystallise into a 2H allotrope (2H-$TaSe_2$) that undergoes a incommensurate CDW transition at 122 K, followed by a commensurate (3×3) CDW instability below 90 K. Its normal state Fermi surface is characterised by dog bone-like electron pockets centred at M and rather circular sections centred at K and Γ as shown in Fig. 2.12(a). Strong Fermi surface nesting has been found for $q \sim \frac{2}{3}(\Gamma - \mathrm{M})$, resulting in a sharp peak in its electronic susceptibility [61]. Below the critical temperature, the new periodic potential backfolds the band

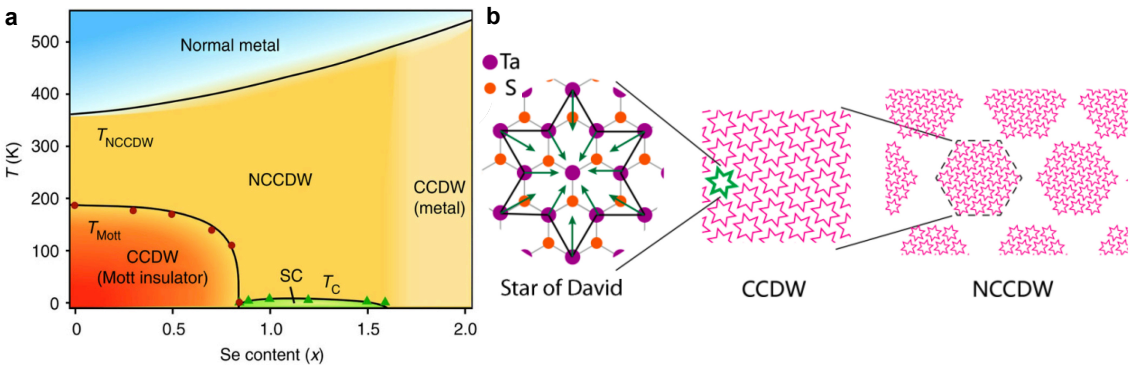

FIGURE 2.11: (a) Phase diagram of 1T-$TaSe_{2x}S_{2(1-x)}$ adpted from [60]. (b) Representation of the lattice distortion in the commensurate and nearly commensurate CDW phase adapted from [59]

into the reduced BZ, opening gaps where the bands cross each other. However, the Fermi surface remains only partially gapped, leaving the system in a metallic ground state, contrary to what occurs in the much simpler 1D case.

Another interesting example of CDW instability in this class of materials is the lattice instability in 2H-$NbSe_2$, a compound also extensively studied for its superconducting phase emerging below 7.2 K in the bulk crystal [56]. As sketched in Fig. 2.12(b), a cut of its Fermi surface at k_z = 0 consists in almost circular pockets centred at Γ and K. Although the Fermi topology doesn't promote any particularly strong nesting, a nearly commensurate (3×3) CDW transition occurs below 35 K. Recent studies reveals the electron-phonon coupling is strongly anisotropic and peaked at $q_{CDW} \sim 2/3(\Gamma -$ M) (blue arrows in Fig. 2.12(b)) [62]. The phonon-mediated scattering between these hot spot states promotes the opening of CDW gaps localised in k-space in restricted sections of the Se-derived pocket centred at K, leaving the rest of the Fermi surface available for superconductivity to emerge, as shown in Fig 2.12(c).

As noted in Table 2.2 the CDW critical temperature in $NbSe_2$ is significantly enhanced in the 2D limit and assumes a commensurate periodicity [56]. Even though these TMDs are layered materials with relatively weak inter-layer coupling, the out-of-plane dispersion of the electronic and phonon modes can affect the CDW mechanism. For instance, in 1T-VSe_2, the relatively weak k_z Fermi surface dispersion shown in Fig.2.12(d-e) is enough to introduce an out-of-plane component in the nesting vector and drive a three dimensional $(4 \times 4 \times \sim 3)$ CDW ordering. At the 2D limit, the lack of such an out-of-plane component enforces the system to find new connections between the Fermi states, resulting in a different periodicity in monolayer configuration. The nature of CDW in 1T-VSe_2 is still highly debated since the material is believed to lie on an incipient ferromagnetic transition that is instead suppressed by the CDW order [63, 64]. Therefore, multiple

nesting vectors, momentum-dependent electron-phonon coupling and the competition with other quantum phases make the description of CDW phenomena in TMDs much more complex than what is predicted by the simplified Peierls model.

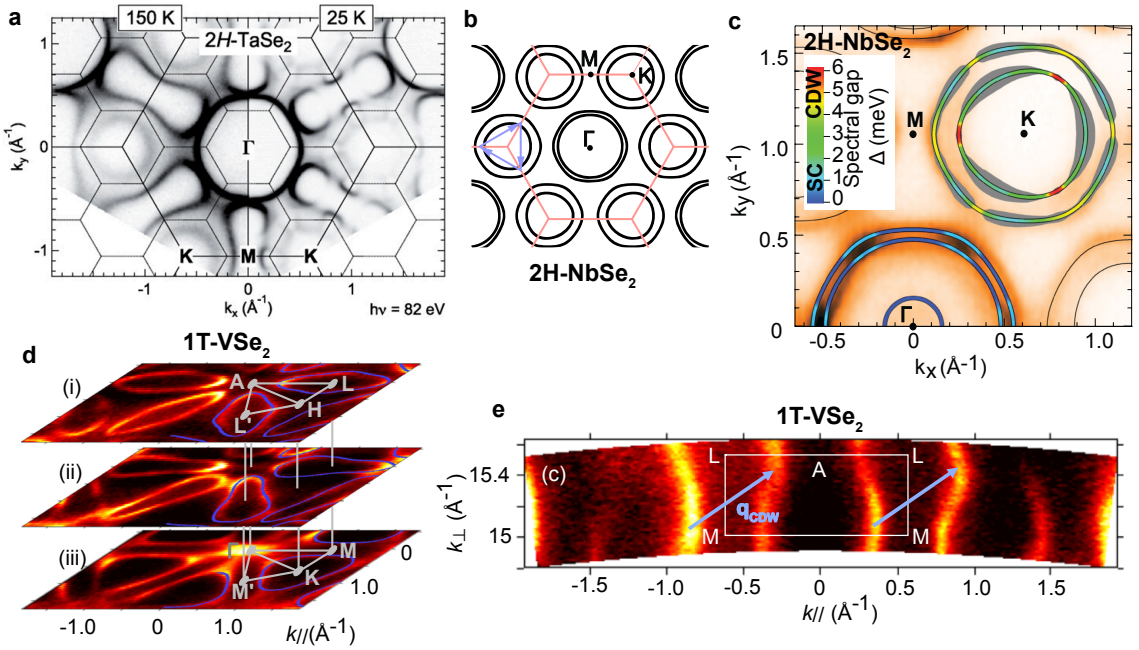

FIGURE 2.12: (a) Partial gapping of the 2H-$TaSe_2$ Fermi surface induced by the CDW transition, adapted from Ref. [50]. (b) Schematic of the 2H-$NbSe_2$ Fermi surface and the triple-q_{CDW} vectors, adapted from Ref. [62]. (c) ARPES Fermi surface of 2H-$NbSe_2$ revealing the wave vector dependencies of the CDW and superconducting spectral gap (Δ), adapted from Ref. [65]. (d-e) ARPES measurements of bulk VSe_2 showing the 3D character of its CDW ordering with a q_{CDW} (blue arrows) having a significant component the out of plane momentum $k_\perp$, adapted from Ref. [66]

2.8 CDW in $TiSe_2$

One of the most studied and controversial CDW TMD is undoubtedly $TiSe_2$. Its lattice instability has been debated for more than 50 years and still drives a considerably rich research field due to its large discrepancy from the conventional Peierls picture. I will start the description of this curious phenomenon from the monolayer compound, where CDW phase assumes a similar but simplified configuration compared to the bulk case [39, 58].

2.8.1 The monolayer case

As previously discussed in sec. 2.2.1, the band structure of monolayer $TiSe_2$ in its undistorted phase consists in a narrow indirect gap between the Se $3p_{x,y}$-derived band at Γ and the bottom of the Ti $3d$ - derived elliptical electron pocket at M. Cooling the temperature down below 220 K,

the system undergoes a (2×2) CDW transition that halves the reciprocal lattice periodicity, as shown in Fig 2.13(a), allowing the backfolding of the original bands into the new BZ accordingly with the three CDW wave vectors q_{CDW} (red arrows) connecting Γ and M. In the CDW phase the Se atoms and Ti atoms are displaced along the three directions indicated by the orange arrows in Fig.2.13(b). Such lattice distortion can be decoupled in three equivalent M-point frozen-in phonon modes, all of them having the same A_u symmetry. These are exactly the soft modes that assume imaginary frequencies in the normal state phonon spectrum in Fig.2.8(a). Each q phonon mode is, therefore, related to the *umklapp* scattering of the original electron and hole bands along the respective wave vector.

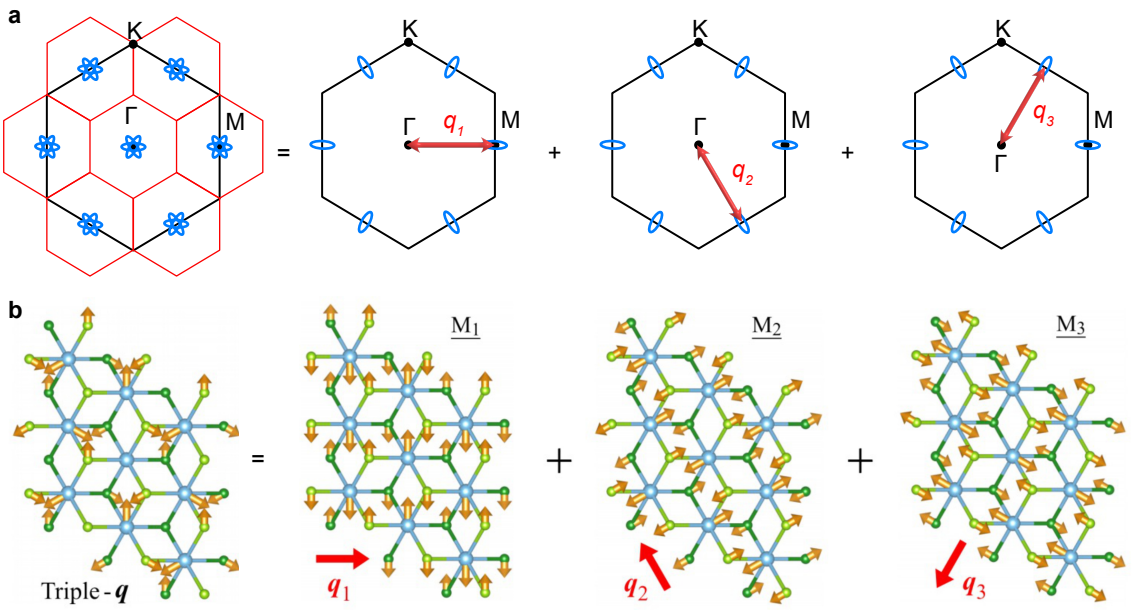

FIGURE 2.13: Decomposition of the band backfolding (a) and lattice distortion (b) in three equivalent q vectors connecting Γ to M and related to the softening of the A_u phonon modes having the same wavevector, respectively. (b) Adapted from Ref. [40].

The backfolding of the two valence bands to M below the conduction pocket is experimentally observed with ARPES as shown in Fig 2.14(a). The equivalent backfolding of Ti $3d_{x'y'}$-derived conduction band to Γ is expected but not evident in the measurement, possibly reflecting the lack of participation of this state in the CDW ordering. The temperature evolution of the replica band is well represented by the energy distribution curves (EDCs) in Fig. 2.14(b) extracted by taking vertical cuts of the ARPES spectra at M for different temperatures. Not only does the backfolded spectral weight (light blue and green peaks) become stronger at low temperatures but is also significantly shifted to lower energies, as evident in Fig. 2.14(c), where the positions of the fitted peaks are plotted. The larger energy separation between the electron and hole pockets in the CDW phase

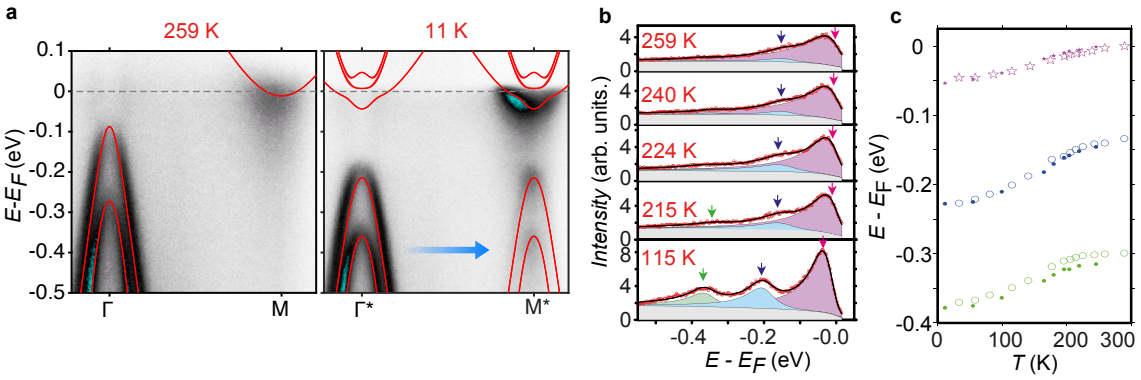

FIGURE 2.14: (a) ARPES spectra of ML-$TiSe_2$ in the normal (259 K) and CDW phase (11 K); In red the tight-binding calculation of the bands, revealing the hybridisation between the hole and electron pockets. (b) Fitting EDCs at M for different temperatures in order to track the energy position of the conduction band minimum (pink) and valence band tops (light blue and green) plotted in (c). Adapted from Ref. [39].

is the direct consequence of the hybridisation between these bands enabled by the onset of the new periodic potential. In Fig. 2.14(a), the tight-binding model in Ref. [39] is used to simulate how the electronic energy spectrum (red bare bands) is affected by the new CDW ordering. The hybridisation splits the degeneracy of the backfolded conduction bands pushing two of them above the Fermi level. In contrast, a third pocket shows the opposite trend becoming slightly more occupied, in good agreement with the observed shift of the conduction band minimum at low temperatures. The enhanced band gap induced by the lattice instability ultimately provides an evident electronic energy gain expected to overtake the lattice energy cost at T_c. The tight-binding analysis estimates the effective hybridisation strength at T=0 K as $2\Delta(0) = 203$meV. For a conventional weak coupling Peierls instability the ratio between $2\Delta(0)$ and $k_B T_c$ is expected to be ~ 3.5 (see eq. 2.22), but in ML-$TiSe_2$ this value is largely exceeded (10.7 assuming $T_c = 220K$). Therefore, the phase transition in this material is driven by a strong CDW coupling that falls outside the validity range assumed for the conventional CDW mechanism. Another signature of such a strong driving force is the endurance of the replica spectral weight even well above T_c, as visible in the ARPES spectrum and in the EDC taken at 259 K in Fig. 2.14(a-b). This feature is usually associated to the presence of strong CDW fluctuations in the normal states.

2.8.2 The bulk case

A similar CDW transition also occurs in the bulk crystal but at slightly lower $T_c \sim 200$ K. Here the lattice distortion is equivalent to the monolayer, but with an additional out-of-plane modulation that inverts the phase of atomic displacement between nearest layers resulting in a $(2\times2\times2)$ lattice

reconstruction as shown in Fig 2.15(a). The new ordering is also consistent with the bulk phonon spectrum calculated following the same method adopted for the monolayer, where all the phonons between L $(1/2 \times 1/2 \times 1/2)$ and M $(1/2 \times 1/2 \times 0)$ assume imaginary frequencies (Fig 2.15(b)).

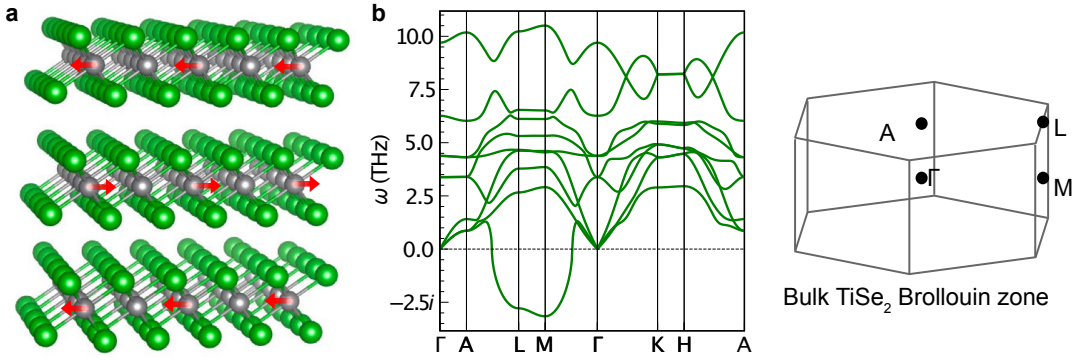

FIGURE 2.15: CDW in bulk $TiSe_2$. (a) Side view of the crystal structure. In the $(2 \times 2 \times 2)$ CDW phase, the atomic displacement has opposite phase between nearest neighbouring layers. Here, only the distortion of the Ti atoms are represented by red arrows for simplicity. (b) DFT phonon dispersion showing the softening of the vibrational modes at two high symmetry points (L and M) of the 3D Brillouin zone.

The normal phase low energy band structure of the bulk compound is a bit more complex compared to the monolayer case [31]. The electron pocket has its minimum at L visible in the ARPES spectrum in Fig 2.16(a). Also at M, a weak spectral weight is observed, although the electron pocket is expected to be a few 100 meV above the Fermi level here. Because the out-of-plane momentum is not conserved during the photoemission process (see chapter 3 for more details), an artificial shadow of the electron pocket at L is also visible in the ARPES spectrum at M. Another difference is also visible in the valence band. An additional outermost band derived mainly from Se $4p_z$ orbitals is visible at Γ, but not at A. Contrary to the $p_{x,y}$ states, the $4p_z$ orbitals have lobes pointing out-of-plane, resulting in a substantial overlap in this direction. Therefore, they generate a band widely dispersed in k_z with a maximum at Γ and a minimum at ~ -2 eV at A. Fig. 2.16(b) shows a 3D representation of the low energy band structure characterised by the elliptical electron pockets at L and the hole pockets at $k_{||} = 0$ that become larger at Γ due to the $4p_z$-derived band. In the CDW phase, the new $(2 \times 2 \times 2)$ periodic potential backfolds the bands accordingly to the q_{CDW} vector represented by the blue arrow connecting Γ and L.

As shown in the ARPES spectra in Fig. 2.16(c), a replica of the valence band appears at L, where it hybridises similar to what occurs in the monolayer case, flattening the top of the backfolded $p_{x,y}$-valence band, as highlighted by the green dashed lines. The backfolding of the $4p_z$ derived band is not observed at L instead, suggesting its marginal involvement in the CDW

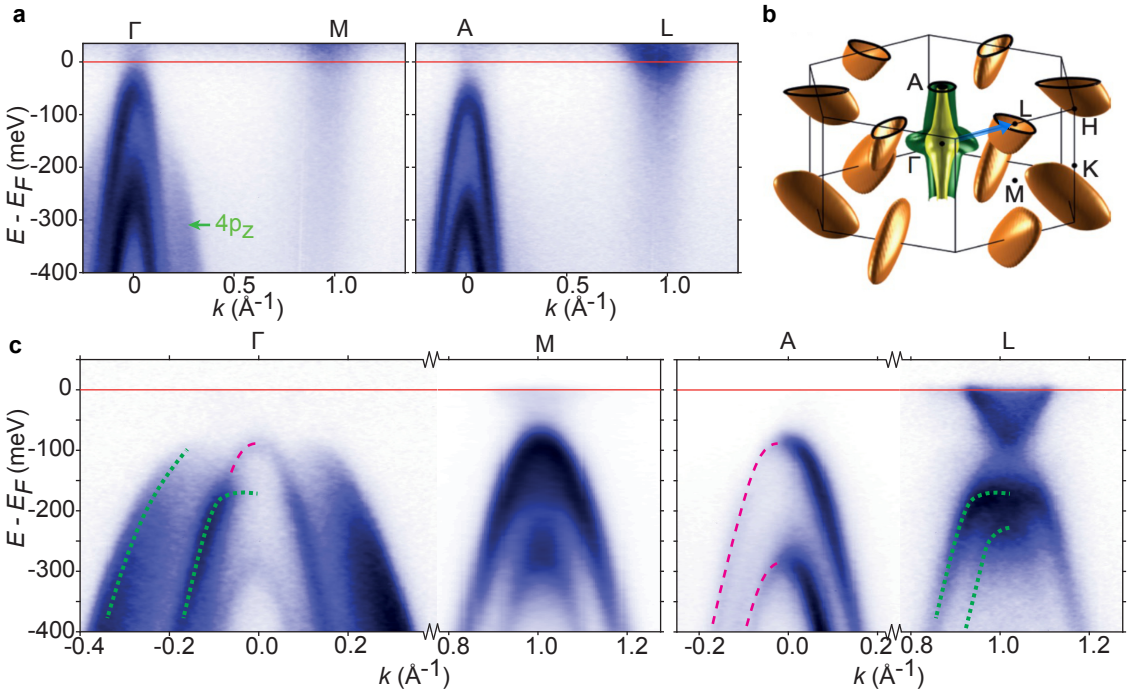

FIGURE 2.16: ARPES spectra of bulk $TiSe_2$ along Γ-M and A-L measured in the normal phase at 300 K (a) and in the CDW phase at 10 K (c). The purple and green dashed lines represents the dispersion of the valence band at A and Γ, respectively. (b) 3D representation of the low energy band structure of bulk $TiSe_2$. The blue arrow represents q_{CDW} connecting Γ and L. Adapted from Ref.[31].

mechanism. At M, such hybridisation is weaker since the conduction band minimum is further away in energy from the hole pocket, leaving the backfolded spectral weight mostly unperturbed. The lattice instability in bulk $TiSe_2$ is phenomenologically very similar to the monolayer case, showing the same strong CDW coupling described earlier for the 2D compound.

2.8.3 Controversy on the CDW phase in $TiSe_2$

Several models have been proposed to explain the CDW transition in $TiSe_2$ in the past 50 years. The lack of a Fermi surface in its semiconducting normal state is the main argument against a possible Peierls-like mechanism driven by the Fermi surface nesting. However, it has been noted that the nesting mechanism is a poor simplification of the Peierls theory, where the peak in the electronic susceptibility χ is instead a more relevant physical quantity for predicting CDW instabilities. As calculated by Kaneko *et. al.* in Ref. [40], a pronounced temperature-dependent peak at $q = \mathrm{M}$ is present in the electronic susceptibility of this material (see Fig. 2.17(a)), which can drive the lattice instability.

However, the conventional CDW BCS-like theory valid in the regime of weak electron-phonon

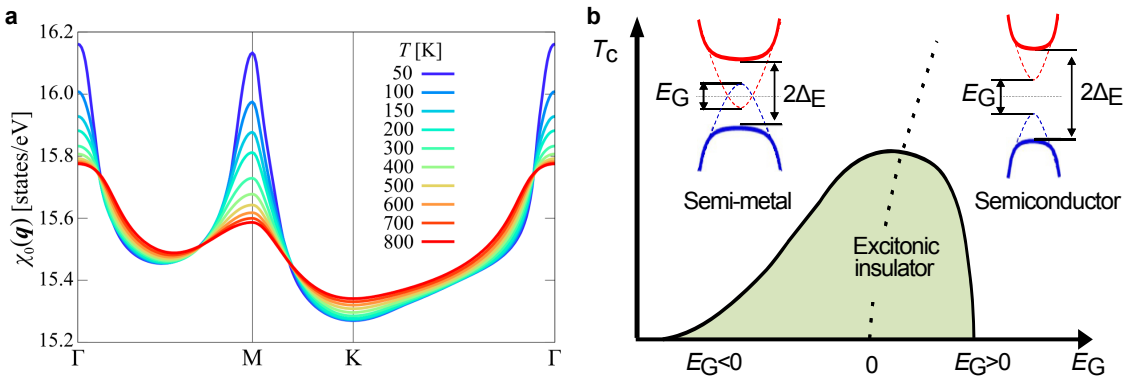

FIGURE 2.17: (a) Electronic susceptibility of ML-$TiSe_2$ at different temperatures, adapted from Ref. [40]. (b) Phase diagram of an ideal excitonic insulator versus the normal state energy gap (E_G), adapted from Ref. [67].

interaction cannot be applied to the strongly coupled CDW transition in $TiSe_2$. An alternative theory assumes the energy gain driving the transition comes from lifting the conduction band degeneracy, similar to a Jahn-Teller distortion [68]. However, this model predicts a first-order transition, in contrast with the experimentally observed second-order transition in $TiSe_2$. Moreover, its CDW phase should be insensitive to conduction band doping, opposite to the fast suppression of the CDW ordering observed under n-type doping.

Another revised theory called pseudo-Jahn-Teller mechanism considers a more realistic strong electron-phonon coupling as driving force for CDW transition. Accordingly, the energy gain derives mainly from lowering the valence band energy as a consequence of the band hybridisation [22, 69]. Although the experiments are in good agreement with this model, several arguments and experimental evidence have been proposed in favour of a more exotic theory. This latter considers the tendency of electrons and holes to attract each other and form bound states called excitons. In a narrow gap semiconductor or small overlap semimetal, the screening environment is weak, resulting in a strong electron-hole Coulomb attraction which in turn promotes exciton formation. When the excitonic binding energy is larger than the energy gap, the energy needed to create an exciton becomes negative, resulting in a spontaneous formation of electron-hole pairs [70]. Consequently, the single-particle spectrum develops a gap lowering the total electron energy as shown in Fig. 2.17(b). In a 1D indirect semiconductor having the valence band at Γ and the electron pocket minimum centered at the BZ boundary like $TiSe_2$, the excitonic condensation induces a modulation in charge density doubling the periodicity of the system. If the electron-phonon coupling is sufficiently strong, the modulated charge density can induce a lattice distortion driving a

CDW-like transition. However, since the transition only breaks a discrete translational symmetry, such condensate wouldn't lead to dissipationless transport or excitonic superfluidity, which requires the breaking of a continuous symmetry operator [71]. Reducing the normal phase gap to zero, the energy gain due to exciton condensation is maximum resulting in the highest T_C in the phase diagram in Fig. 2.17(b). For negative energy gaps, the free charge carriers at the Fermi level start screening the Coulomb attraction between electrons and holes, suppressing the expected T_C.

As evident, the electron-phonon coupling also plays an important role in the exciton mechanism, and the idea of a more cooperative driving force between these two microscopic mechanisms has been growing stronger in the field [72]. Noticeably, the Peierls instability can also be considered a pairing mechanism between electrons and holes mediated by the electron-phonon coupling. Indeed, it has been shown that by including an attractive Coulomb potential between these two opposite charge carriers, the electron-hole pairing is eased, enhancing the CDW stabilisation in $TiSe_2$ [40]. Thus, the two mechanisms are not at all mutually exclusive, but rather they might be two different sides of the same phenomenon. The complexity of the CDW mechanism makes $TiSe_2$ and, in general, Ti-based dichalcogenides an attractive playground where the cooperation of different coupling can be experimentally manipulated. The targeted engineering of the low energy band structure might indeed suppress or emphasise one of the multiple driving forces and, therefore, provides useful insight for a deeper understanding of the CDW in $TiSe_2$. In the next chapter, the experimental techniques I used to manipulate and study the electronic energy spectrum of Ti-based dichalcogenides are introduced.

Chapter 3

Experimental methods

Tuning the electronic properties of a 2D material requires the ability to control and manipulate the crystal lattice or its surrounding on the atomic scale. In this work, I used molecular beam epitaxy (MBE) to grow atomically thin films of Ti-based dichalcogenides and modify their composition. Electron diffraction techniques were used to verify the actual realisation of the desired crystal structure and quality. Ultimately, the electronic energy spectrum of the sample was measured using angle resolved and X-ray photoemission spectroscopy (ARPES and XPS, respectively) to investigate the CDW instability in the tailored material. This chapter reports a brief overview of the working principle of these experimental techniques and the details of the experimental set-ups used to acquire the measurements reported and discussed in the following chapters.

3.1 Molecular beam epitaxy

Molecular beam epitaxy is a highly controllable and reliable crystal growth technique enabling the deposition of high-purity, epitaxial thin films with atomic precision on the film thickness. Nowadays, it is a well-established method to produce III-V semiconductor quantum well [73], perovskite heterostructures [74], nanowires [75], quantum dots islands [76] and organic molecule thin films [77]. A schematic of a typical MBE process is shown in Fig. 3.1. The source materials (typically the single elements comprising the desired crystal) are placed in crucibles inside a UHV chamber and heated up to a certain temperate, at which they start to evaporate, creating atomic or molecular beams directed to the substrate. Here, these particles can condense and arrange themselves in crystals depending on the substrate temperature. The chemical composition of the deposited film depends on the flux ratio between the different precursor beams that are controlled by changing the effusion cell temperature. Multiple elements can be deposited either simultaneously (co-deposition) or sequentially by alternating the opening of the shutters, a method usually

employed to create heterostructures comprised of layers with different compositions stacked one over the other.

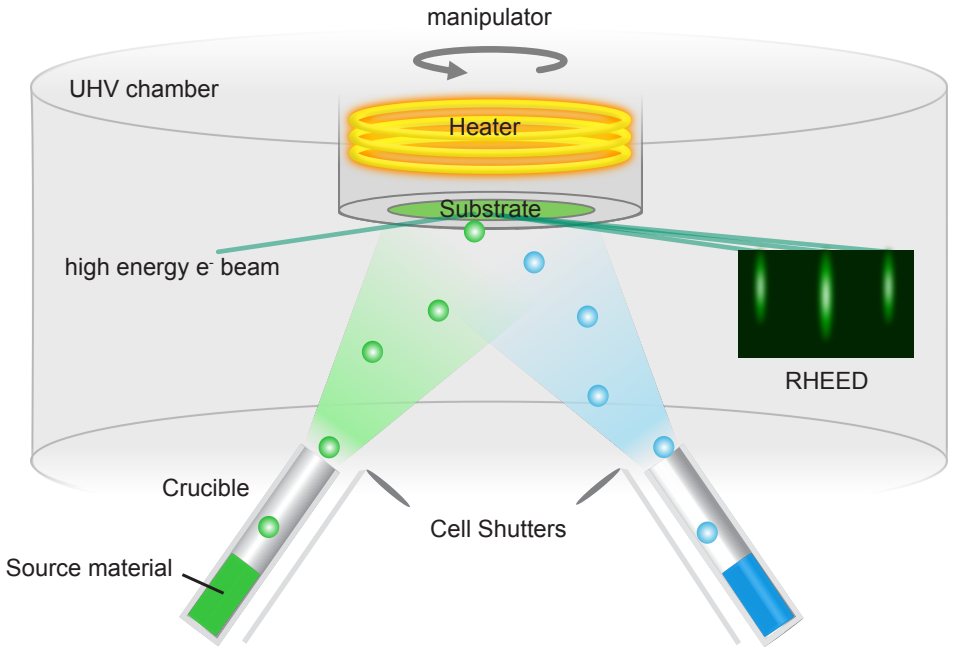

[t]

FIGURE 3.1: Schematic of the UHV chamber where the precursor elements are evaporated on a substrate. The crystallisation of the new material can be monitored in real time with reflection high energy electron diffraction (RHEED).

The crystallisation process can be monitored *in-situ* by measuring the diffraction pattern of the growing crystal using reflection high energy electron diffraction (RHEED), which will be discussed in more detail in Sec. 3.2. The entire process takes place in an ultra-high vacuum (UHV) environment in order to minimise the unintentional incorporation of impurities and isolate the process from external condition. Moreover, at a typical operational pressure of 10^{-9} mbar, the mean free path of the particle is $\sim 10^4$ m), which is much larger than the typical dimension of the growth chamber ≈ 1 m. Consequently, the atoms of the incoming precursor flux won't interact until they condense on the substrate. The surface atomic structure of this latter imposes an epitaxial constraint to the growth of the new material. If the substrate and the epilayer strongly interact such as by forming chemical bonding at the interface, the deposited film tends to crystallise with the same atomic structure and lattice constant of the substrate. However, 2D materials typically couple only through weak van der Waals forces allowing a partial or full relaxation of the epitaxial constraint. In section 3.2.1 we will see how such weak coupling between ML-$TiSe_2$ and the graphene substrate prevents the strain of the dichalcogenide film despite the large lattice mismatch

between these two materials.

3.1.1 Crystal growth

The versatility of MBE derives from the fine control of the growth parameters, i.e. substrate temperature, atomic fluxes and pressures, which have direct effects on the microscopic processes involved during the crystallisation. The epitaxial process results from the cooperation of five phenomena: adsorption, desorption, diffusion, nucleation and growth [78]. When an atom from the molecular beam reaches the substrate, it can be adsorbed on the surface, becoming a so-called ad-atom, as illustrated in Fig.3.2(a). However, if the kinetic energy of the ad-atom is larger than its bonding energy with the surface, it desorbs, leaving the surface. The probability of an atom sticking to the surface is called the sticking coefficient. Its value decreases monotonically with the substrate temperature (T_s), with a rate that largely depends on the specific chemical nature of the precursor atom. Thus, even if two elements are evaporated with the same flux, the deposited film will have a composition dominated by the precursor element having the larger sticking coefficient at that specific growth temperature.

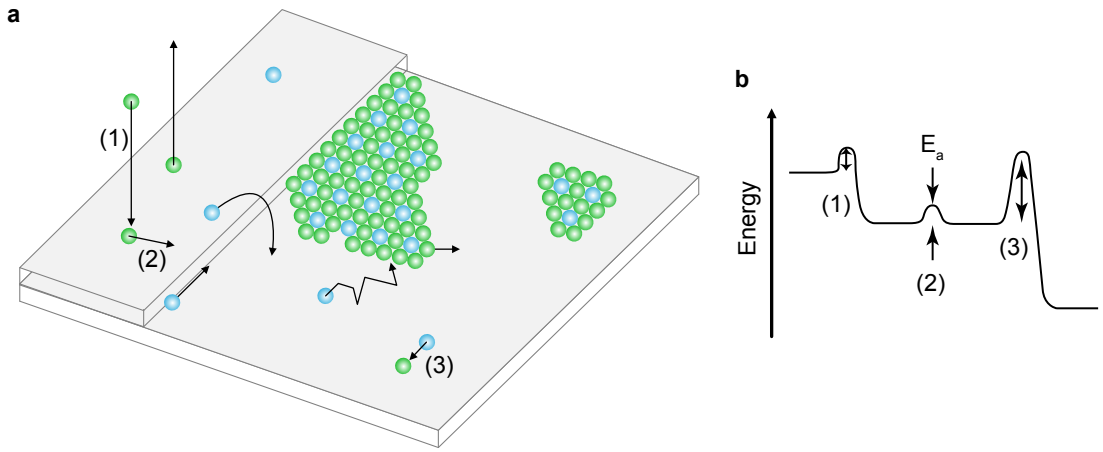

FIGURE 3.2: (a) Kinetic mechanisms occurring during the growth of an epilayer on top of the substrate surface. (b) Change in the ad-atom energy during the adsorption on the surface (1), diffusion (2) and reaction with another ad-atom (3). All of these steps require to overcome a certain activation energy E_a denoted by black arrows.

The ad-atoms that do not desorb remain in the adsorption site, where they vibrate around their equilibrium positions. Thermal fluctuation can provide them with enough energy to exceed the saddle point in the surface potential between two adjacent adsorption sites promoting their diffusion on the surface. When two ad-atoms meet on the surface, they can react, forming a dimer having a lower desorption rate and surface mobility than single ad-atoms. When more atoms

aggregate together, a small nucleus starts growing and forming the desired crystal. The rate (R) at which each of these microscopic processes occurs can be described by the Arrhenius equation:

$$R = Ce^{-E_a/k_B T_s} \tag{3.1}$$

where E_a is the activation energy barrier that needs to be overcome in order to activate the specific process, k_B is the Boltzmann constant and C is an exponential prefactor, usually considered constant in temperature. This latter term has typical values of 10^{12}-10^{13} Hz related to the vibrational frequency of the ad-atom in the adsorption site. The ad-atom energy during the main kinetic processes of the growth is illustrated in Fig. 3.2(b), showing the different activation energies for adsorbtion (1), diffusion (2) and dimerisation (3). Noticeably, after step (1) and (3), the ad atom energy is lowered resulting in a higher energy barrier needed to reverse such processes. Thus, the system evolves during the deposition searching for a minimum in its free energy. Usually, the growth of large and high quality crystals requires relatively high temperatures and low deposition rates in order to let the particles on the surface able to reverse such kinetic processes and let the system explore a large section of the phase space, eventually reaching a thermodynamically stable configuration.

The growth parameters can also alter the thermodynamic stability of the crystal formed on the surface. The free energy change ΔG of the system due to the formation of a 2D nucleus comprised of n atoms can be written as:

$$\Delta G = -n\Delta\mu + n(\gamma_F + \gamma_{S/F} - \gamma_S)\Omega^{2/3} + n^{1/2}\gamma_E \tag{3.2}$$

where Ω is the atomic density of the material and $\Delta\mu$ is the chemical potential of the material, γ denotes the surface free energy of the film-vacuum (F), substrate-vacuum (S) and film-substrate (S/F) interfaces, while γ_E denotes the edge free energy. This last term is positive and tends to increase the nucleus energy. Instead, the first term is negative and tends to stabilise the nucleus. The second term is negative when $\gamma_S > \gamma_{S/F} + \gamma_F$, namely when the system prefers to expose the surface of deposited material instead of the substrate one. This condition is also referred to surface wetting. In this condition, ΔG has a non-monotonic trend shown in Fig. 3.3(a) having a maximum at:

$$n_{crit} = \sqrt{\frac{2\gamma_E}{\Delta\mu - \Delta\bar{\mu}}} \tag{3.3}$$

with $\Delta\bar{\mu} = (\gamma_F + \gamma_{S/F} - \gamma_S)\Omega^{2/3}$. For $n < n_{crit}$ the nucleus is too small and tends to break apart. For $n > n_{crit}$ instead, the nucleus size is large enough to form a thermodynamically stable crystalline domain that tends to grow in size. The number of stable nuclei is particularly important because it can affect the dimension of the final crystalline domains. Since $\Delta\mu \propto T$, n_{crit} is smaller at lower temperatures resulting in lots of small domains formed on the surface very close to each other. Therefore, their lateral growth is limited by the reduced space available. At high temperatures instead, only a few nuclei become stable, resulting in bigger crystals. These conditions are experimentally observed in the atomic force microscopy topographic images in insets of Fig. 3.3(b), showing the morphology of the 2D microscopic domains of ML-$TiSe_2$ grown with our MBE system on a graphite substrate at two different growth temperatures as reported in Ref. [79]. At high growth temperatures (T= 600°C), the $TiSe_2$ film consists of relatively big triangular domains of size $\sim 1\mu$m spread on the substrate surface. Instead, growing at lower temperatures (T=300°C) results in lots of small nuclei closely packed together. The difference in coverage can be ascribed to the lower sticking coefficients of the precursor Se and Ti atoms at high temperatures resulting in a slower growth. In real material, the defects on the substrate surface act as preferential nucleation sites that reduce the free energy of the nucleus stabilising domains with $n < n_{crit}$. This is evident, for example, in the AFM image of a low T growth, where the majority of the nuclei start from the two lines representing two step edges of the graphite surface. Therefore, the substrate surface's quality is extremely important to obtain highly crystalline films with MBE.

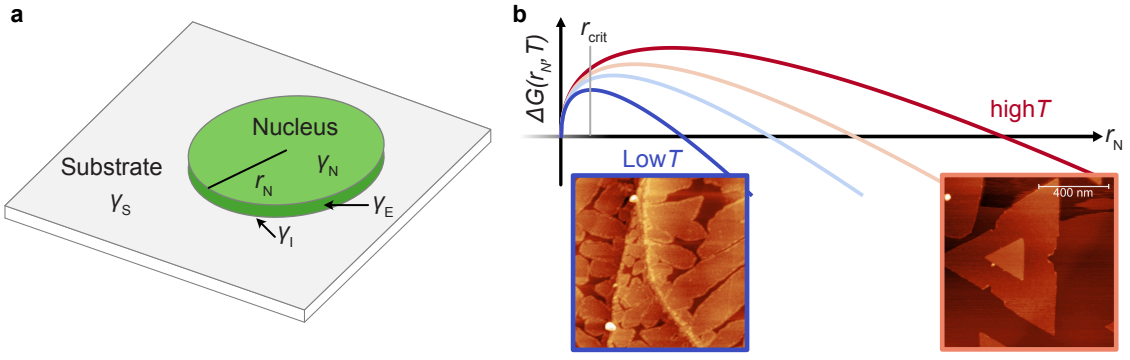

FIGURE 3.3: (a) A circular nucleus (N) with radius r_N on a substrate (S). (b) Change in the Gibbs free energy of the system depending on the nucleus radius and temperature (T). In insets the AFM images of ML-$TiSe_2$/HOPG grown at low and high temperatures, showing a different number of nuclei (adapted from Ref. [79].

As already mentioned, the thermodynamic condition to obtain 2D nuclei is $\gamma_S > \gamma_{S/F} + \gamma_F$. In this regime, when the 2D islands coalesce together covering the entire surface, the growth continues forming the successive layer above the previous one, as illustrated in Fig. 3.4. For

substrates having $\gamma_S < \gamma_{S/F} + \gamma_F$ the deposited material doesn't wet the surface but prefers to grow in a 3D cluster in order to minimise its exposed surface. Again, the substrate has a very important role in dictating the morphology of the deposited film. The mismatch between the lattice constants of the substrate and the deposited material can also induce a strain field into the film provoking instability in the 2D growth mode. In the so-called Stranski-Krastanov (S-K) mode, after a critical thickness of the wetting layer, the elastic energy stored in the film increases the free energy of the system. A way to dissipate this elastic energy is to form 3D islands that can partially relax the film, thereby minimising the total free energy. A competing mechanism to dissipate the epitaxial strain is the formation of shear dislocation at the interface between the two films relaxing the strain field and avoiding the island formation. As we will see in chapter 6, the epitaxial strain is probably the main cause of island formation occurring during the deposition of the functional material V_2O_3 grown on Al_2O_3.

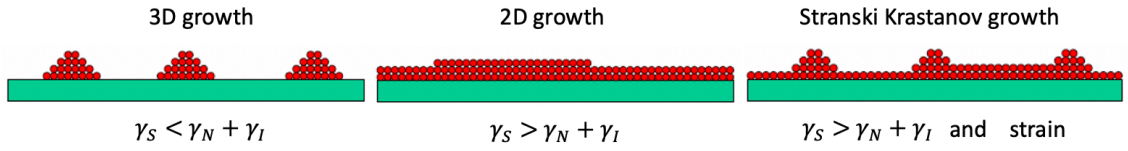

FIGURE 3.4: Depending on the surface free energy γ of the substrate S, nucleus N and interface I, the film can assume a 3D or 2D configuration. The introduction of epitaxial strain can cause an instability in the layer-by-layer growth transforming into a 3D growth after few layers.

3.1.2 MBE apparatus

The MBE system used in this work consists of two growth chambers: the first (GM1) is dedicated to the deposition of oxide materials, while the second (GM2) is designed for the growth of 2D TMDs (Fig. 3.5). This latter is equipped with Se and Te effusion cells that provide the desired partial pressure of chalcogenide. Since Se evaporates in molecules Se_x with $x \geq 2$, the beam evaporated from the crucible passes through a section called cracker heated up to 500° C, where the molecules are cracked to single atoms. The resulting atomic beam is therefore directed to the substrate.

Evaporating Ti requires a high temperature effusion cell able to reach a temperature of $\sim$ 1350° C. The beam equivalent pressure (BEP) of Se, Te and Ti introduced in the chamber is calibrated just before the growth by placing a Bayard-Alpert type ionization gauge close to the substrate surface and then it is retracted before the growth commences. A long tunnel kept in UHV allows the sample transfer from the two MBE chambers to an ARPES system where the

electronic structure of the deposited material can be investigated directly after the growth without contaminating the sample surface with air contaminants. Preliminary structural information of the grown film can also be extracted directly from the growth chamber using reflection high energy electron diffraction (RHEED), as will be discussed in detail in the next section.

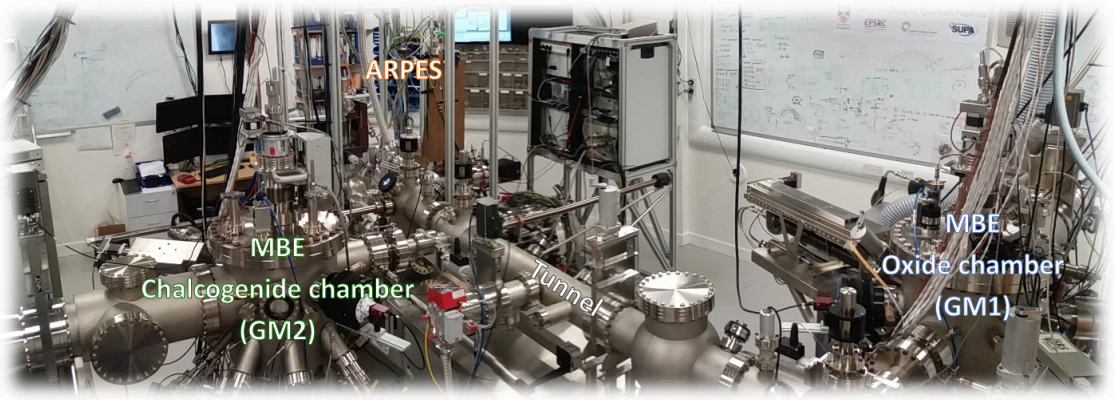

FIGURE 3.5: MBE system used during this work consisting of two growth chambers connected by a tunnel kept in UHV. The entire cluster is also connected to the ARPES system, visible on the background, where XPS measurements are also performed.

3.2 Electron diffraction

During the work presented in this thesis, I used two different electron diffraction techniques to probe the reciprocal lattice of the films grown with MBE: reflection high energy electron diffraction (RHEED) and low energy electron diffraction (LEED). The first consists of measuring the diffraction pattern generated by a high-energy electron beam (15-35 keV) reflected from the sample surface. The incident beam is directed to the surface at a very shallow angle ($\sim 5°$), penetrating into the material for only a few atomic layers. Thus, the electron probe is not diffracted from the substrate lattice in the out-of-plane direction but only from the surface in-plane atomic structure. The reciprocal surface lattice can be therefore represented by a 2D lattice of infinite rods perpendicular to the surface plane as shown in Fig. 3.6(a). The diffraction occurs when the momentum transfer between the incoming and scattered electron $q_f - q_i$ is equal to a surface reciprocal lattice vector $G_{\parallel}$, also known as Laue condition:

$$G_{\parallel} = q_f - q_i \tag{3.4}$$

The momentum of the electron scattered from the surface can be represented in the reciprocal space by a sphere (the Ewald sphere) having radius equal to the wavevector of the incident electron.

The Laue condition is satisfied when the Ewald sphere crosses the surface reciprocal lattice rod. The diffracted electrons are impressed on a phosphorous screen where the RHEED pattern appears as spots aligned on concentric circumferences, as illustrated in Fig. 3.6(a). When the electron beam is aligned along a high symmetry direction of the crystal, the perpendicular in-plane lattice constant a can be estimated using:

$$a = \frac{2\pi}{\theta L} \tag{3.5}$$

where L is the distance between the sample and the phosphorous screen and θ is the angle in the surface plane between two diffraction spots.

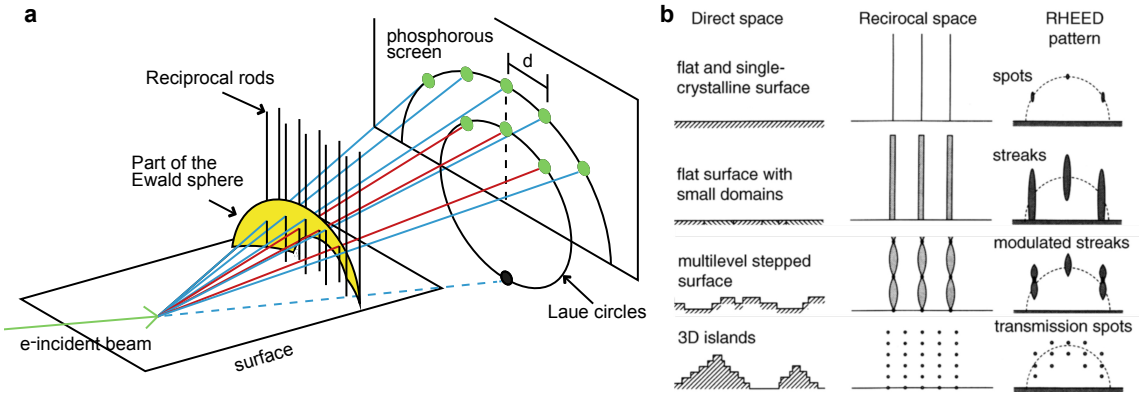

FIGURE 3.6: (a) The RHEED pattern can be described as the intersection of the Ewald's sphere with the reciprocal surface lattice projected on a phosphorous screen; adapted from [80] (b) Various surface morphologies produce different diffraction patterns; adapted from [81].

Valuable information about the crystal quality and surface morphology can be extracted from the RHEED pattern. Similar to other diffraction techniques, the diffraction spot width is inverse proportional to the coherence length of the surface lattice. Therefore, the sharper the RHEED pattern, the higher the crystal quality of the deposited film. Increasing the surface roughness, the two-dimensional pattern acquires an out-of-plane dispersion that becomes more similar to a transmitted pattern with spots resembling the out-of-plane reciprocal lattice of the sample. Otherwise, if an amorphous material is deposited, the RHEED signal becomes a uniform background without any diffraction.

Another useful technique to investigate the reciprocal space of the material surface is low energy electron diffraction. Contrary to RHEED, a low energy electron beam ($\sim$10-500 eV) is directed perpendicular to the surface. The backscattered and diffracted electrons are then collected

by a grid that accelerates them to higher energies in order to activate the fluorescence of the phosphorous screen, as shown in Fig. 3.7(a).

The LEED image of the substrate used in this work for the MBE of TMDs, namely a bilayer-graphene (BL-Gr) on SiC(0001), is shown in Fig. 3.7(b). The 2D diffraction pattern comprises two main hexagonal reciprocal lattices of SiC and Gr rotated to each other by 30°. In the direct space, the superposition of the two 2D crystal structures generates a superlattice with a larger unit cell comprised of 13 Gr unit cells. This new periodicity generates a so-called moiré pattern in the reciprocal space consisting of small hexagons surrounding the original SiC and Gr spots. The moiré reciprocal superlattice is also observed in the RHEED pattern acquired before the growth indicated by the grey spots, while the elongated spot circled in blue is associated with the Gr (100) diffraction. The additional lines visible in the RHEED image are generated from the quasi-elastic scattering of the electron with the atomic surface structure. They take the name of Kikuchi lines and are usually visible only for highly ordered surfaces, suggesting the good crystal quality of our substrates.

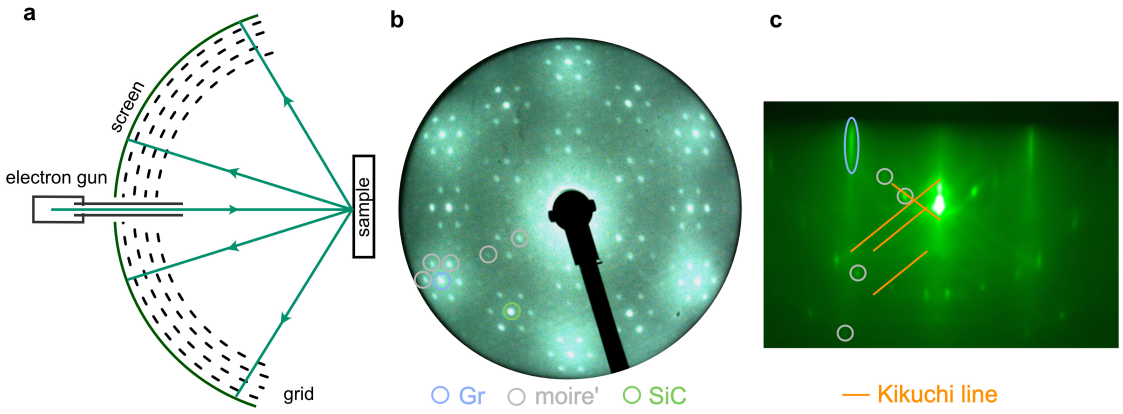

FIGURE 3.7: (a) Schematics of a LEED apparatus, where the electrons (green lines) are backscattered from the sample surface and collected on a phosphorous screen. Typical LEED (b) and RHEED (c) images of the BL-Gr/SiC(0001) substrate used in this work.

3.2.1 Growth of TiX_2

Here an example of the growth of ML-TiX_2 (X=Se, Te) using our MBE system is described. As briefly mentioned in section 3.1, a graphene-like substrate provides a suitable template for the MBE of TMDs since it has a chemically inert triangular lattice, and the absence of dangling bonds promotes weak van der Waals coupling with the deposited film. For this work, I used BL-Gr/SiC(0001) substrates obtained by graphitisation of SiC chips heated at 1530° C for 9 minutes in a dedicated UHV chamber. In order to maintain a certain Si partial pressure on the substrate

surface, two SiC chips with dimension (3×7 mm or 3×6 mm) are assembled face to face on a Mo stage and spaced by two Ta foils with a thickness of 0.15 mm as shown in Fig 3.8(a). The area covered by the spacers at the two edges of the substrate is characterised by poor graphene quality and therefore avoided during the successive analysis. An electrical current of $\sim 2 - 3$ A is applied to the parallel SiC chips reaching the desired temperature monitored using a pyrometer. After the process, the resistance of the sample measured using a simple multimeter changes from infinite to $\sim 20\Omega$, suggesting the effective graphitisation of the SiC chips. However, depending on the assembling, the electrical contact can be different between the two SiC chips resulting in a different heating power experienced by the two substrates, which in turn might affect the crystal quality of one or the other.

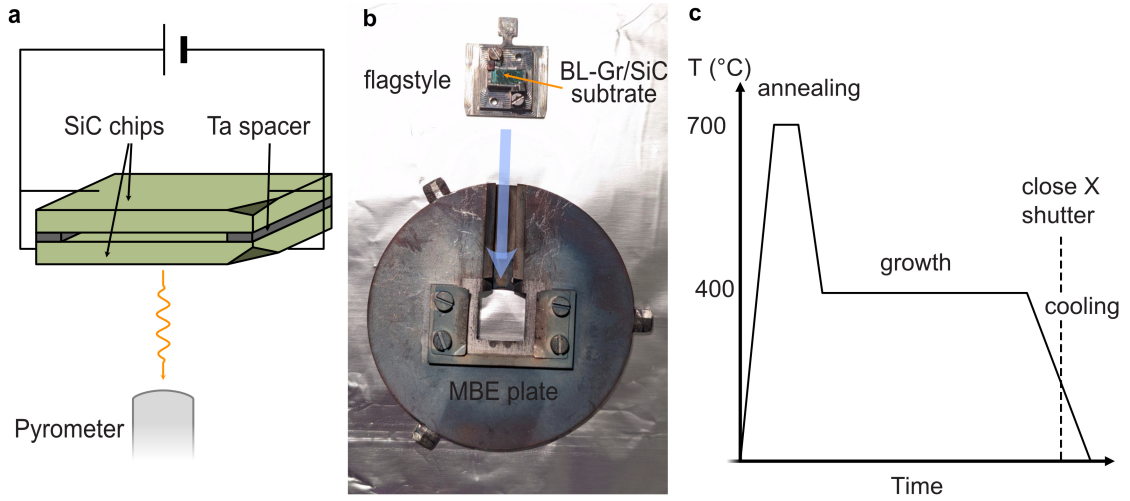

FIGURE 3.8: (a) Schematic of the setup used for the direct current heating of SiC. (b) Flagstyle sample holder and MBE plate used in our UHV system. (b) Schematic of the temperature ramp for the MBE process performed during the growth of ML-TiX_2.

After this process, the substrate is assembled on a stainless steel flagstyle sample holder shown in Fig. 3.8(b), ensuring the electrical and thermal contact with the ARPES manipulator. However, this holder alone is not compatible with the bigger MBE manipulator and a second plate is needed in order to load the substrate inside the MBE chambers. The sample is then loaded in a pre-vacuum chamber (load-lock) where it is heated at $\sim$200°C for 6 hours in order to degas the air contaminants stuck on the substrate and sample holder surfaces. When the pressure in the load-lock reaches $\sim 5 \cdot 10^{-9}$ mbar, the plate is transferred into the growth chamber (GM2), where another annealing up to 700°C is performed to further clean the surface from carbon-derived air contaminants. When the pressure inside the chamber recovers below $\sim 5 \cdot 10^{-9}$ mbar the sample is cooled down to the typical growth temperature of 400°C, and a RHEED image of the substrate before the growth

is typically acquired for reference (Fig. 3.9(a)). The MBE growth starts opening the shutters of the preheated effusion cells, which in turn allows the delivery of the precursor fluxes of Ti and the chalcogen X on the substrate. In order to prevent the formation of chalcogenide vacancies, the growth is performed with a large X overpressure using a flux ratio X/Ti of ~ 100. However, due to the lower sticking coefficient of the chalcogenide atoms at this growth temperature, Se and Te are not able to deposit unless they react with Ti ad-atoms. Therefore, the deposition rate is determined only by the Ti flux, which is typically set to obtain one monolayer of TiX_2 in ~ 70 minutes.

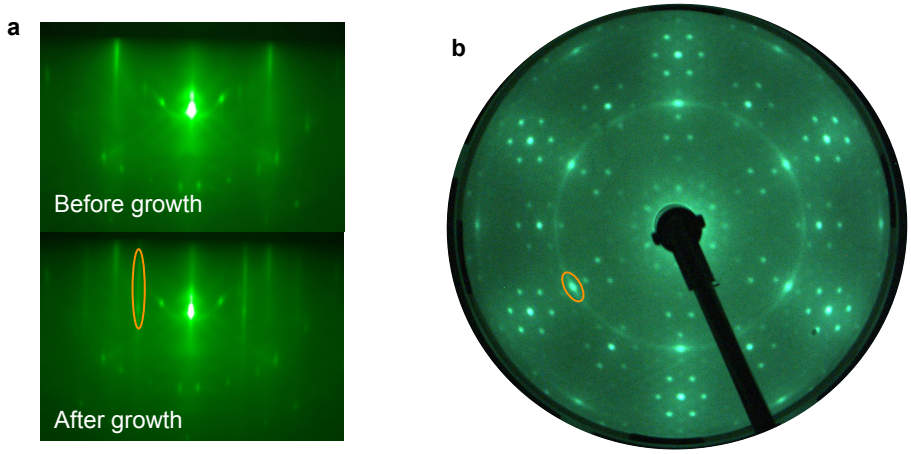

FIGURE 3.9: (a) RHEED images before and after the growth, showing the appearing of the $TiSe_2$ diffraction pattern (orange). (b) LEED measured after the MBE growth (e-beam energy = 110 eV) revealing the angular broadening of the TMD film (orange) due to the partial rotational disorder.

At the end of the growth, the Ti shutter is closed, while the chalcogenide flux remains on during the cooling until the temperature drops below 250°C for Se or 350°C for Te. This procedure allows to minimise the amount of chalcogenide vacancies created during the cooling, but avoid the deposition of elemental Se or Te layer on the surface. Fig. 3.9(a-b) shows the RHEED and LEED images of the sample measured after growth revealing the new diffraction pattern of TMD film (in this case $TiSe_2$) superimposed to the more complex diffraction pattern of the substrate discussed in the previous section. Despite the large lattice mismatch between the two materials, ML-$TiSe_2$ results completely relaxed with a lattice constant of 3.54 ± 0.01 Å, consistent with the experimental value reported in literature [58].

Noticeably, the LEED signal of $TiSe_2$ is sharp in the radial direction but slightly broader in the angular direction resulting in a circular pattern. This is due to the angular misalignment of the 2D $TiSe_2$ mesoscopic domains compared to the graphene substrate orientation, common in all the van der Waals MBE films grown on graphene or graphite. This effect is also present in ML-$TiTe_2$, and it will be discussed in more detail in section 4.7.1.

3.3 Photoemission spectroscopy

Photoemission spectroscopy comprises several characterization techniques able to probe the electronic energy states within a solid [82]. All of them exploit the photoelectric effect, namely the ability of a material to emit electrons when its surface is illuminated with light having energy $h\nu$ larger than the work function of the material. Because the energy is conserved during the process, the kinetic energy E_{kin} of the photoemitted electrons is:

$$E_{kin} = h\nu - E_B(k) - \Phi \tag{3.6}$$

where Φ is the work function of the spectrometer ($\sim$ 4.5 eV) in electrical contact with the sample surface and $E_B(k)$ is the binding energy of the electron in the solid before the excitation. Thus, by measuring the E_{kin} one can extract useful information about the energy level of the electron inside the material as schematically depicted in Fig. 3.10.

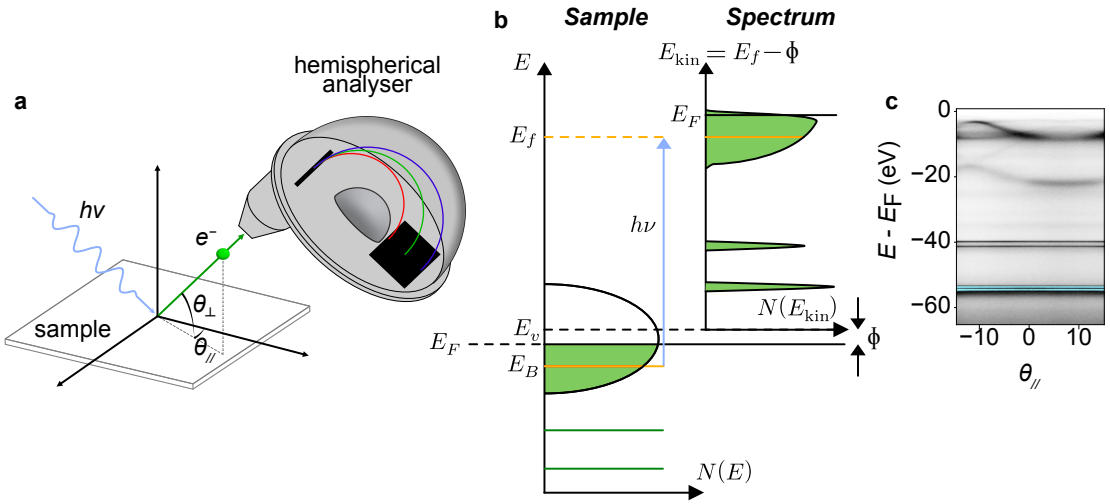

FIGURE 3.10: (a) Photoemission of an electron from the sample surface detected by the hemispherical analyser. (b) Representation of the energy conservation during the photoemission process. (c) Typical ARPES spectrum detected by the analyser.

This is experimentally possible by detecting the escaped electron using a hemispherical analyser. The electrons are firstly focused by passing through electrostatic lenses and then enter the analyser from an entrance slit which selects the particles having a certain $\theta_\perp$, as shown in Fig. 3.10(a). Inside the detector, a hemispherical capacitor generates an electrostatic field that curves the trajectory of the incoming electrons with a radius depending on their kinetic energy *i.e.* on their velocity. The electrons that reach the other end of the analyser are detected by a two-dimensional CCD camera depending on their kinetic energies and their direction entering the

slit at different angles $\theta_{\parallel}$. The direction of the incoming electron can be ultimately related to the momentum of the initial photoexcited state by considering the momentum conservation during the photoemission process. This property is exploited in angle-resolved photoemission spectroscopy (ARPES) to probe the energy-momentum dispersion relation of the analysed material directly. Indeed, the momentum of the electron escaping from the sample can be decomposed in its spatial components:

$$\begin{aligned} K_x &= \frac{1}{\hbar}\sqrt{2mE_{kin}}sin\theta_{\perp}cos\theta_{\parallel} \\ K_y &= \frac{1}{\hbar}\sqrt{2mE_{kin}}sin\theta_{\perp}sin\theta_{\parallel} \\ K_z &= \frac{1}{\hbar}\sqrt{2mE_{kin}}cos\theta_{\parallel}. \end{aligned} \tag{3.7}$$

Because the photon momentum is relatively small for the photon energy used in the experiments (10-100 eV) compared to the typical electron momentum within the solid, the change in the electron momentum due to the photon adsorption can be neglected. Thus, only vertical (*i.e.*, *k*-conserving) transitions are allowed. Since the in-plane translational symmetry of the crystal is preserved on its surface, the in-plane momentum of the excited electron in the solid $k_{\parallel}$ is conserved during the photoemission:

$$k_{\parallel} = K_{\parallel} = \sqrt{K_x^2 + K_y^2} = \frac{1}{\hbar}\sqrt{2mE_{kin}}sin\theta_{\parallel} \tag{3.8}$$

With this relation, one can convert the angular position of the detected electron on the CCD camera to its original in-plane momentum and thus reconstruct the band structure of the sample. A typical ARPES spectrum is shown in Fig. 3.10(c) where several dispersed valence bands are visible close to the Fermi level, while at higher binding energies, the spectrum is dominated by the dispersionless signal of the ionic core levels. Scanning along different $\theta_{\perp}$ by rotating the sample orientation, a complete map of the in-plane 2D band structure can be obtained.

In contrast, information about the out-of-plane direction cannot be extracted directly from the spectrum. At the surface, the out-of-plane translational symmetry is broken, and the out-of-plane component of the electron momentum is not a good quantum number. Considering the approximation that the valence electrons behave as nearly free particles, the energy conservation ensures:

$$E_{kin} = \frac{\hbar^2(k_{\parallel}^2 + k_z^2)}{2m} - V_0 \tag{3.9}$$

where V_0 is the potential barrier at the surface of the solid as shown in Fig. 3.11(a). Substituting $k_{\|}$ with the last expression in eq. 3.8 one can obtain:

$$k_z = \frac{1}{\hbar}\sqrt{2m(E_{kin}cos^2\alpha + V_0} \tag{3.10}$$

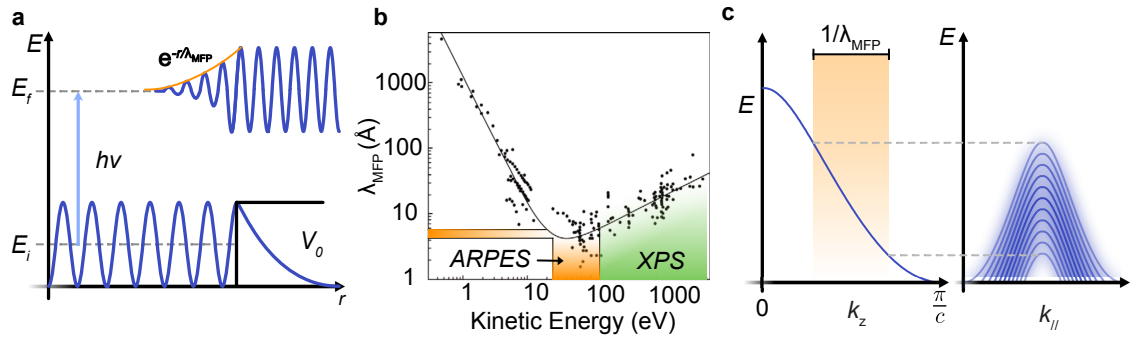

FIGURE 3.11: (a) The wavefunction of the electron in the final state with energy E_f penetrates into the solid for a limited depth related to the elastic mean free path λ_{MFP}, causing a partial loss of coherence with the k_z momentum of the initial state. (b) General trend of λ_{MFP} on the electron kinetic energy, adapted from [83]. (c) Uncertainty on k_z proportional to $1/\lambda_{MFP}$ (orange area) cover a substantial section of the BZ, causing a broadening of the ARPES spectrum measured along $k_{\|}$.

This relation between k_z and E_{kin} allows probing the out-of-plane momentum by changing the kinetic energy of the escaped electron using a light source with different photon energies. However, the uncertainty on k_z is usually a significant fraction of the out-of-plane BZ dimension introducing an intrinsic limitation to this method. Indeed, the penetration depth of ARPES is limited by the elastic mean free path λ_{MFP} of the electrons in the solid. Since λ_{MFP} depends on the photon energy (typically 10-100 eV for ARPES experiments) following the trend in Fig. 3.11(b), only the electron within ~ 5 Å will be emitted from the surface without experiencing an inelastic scattering event. Therefore, the coherence of the plane wave free electron wave function $\phi(k_z)$ along the out-of-plane direction z is partially lost, inducing an intrinsic uncertainty on the probed out-of-plane momentum related to the modulus squared of its Fourier transform $|\phi(k_z)|^2$, which is proportional to:

$$|\phi(k_z)|^2 \alpha \frac{1}{2\pi\lambda_{MFP}} \frac{1}{(k_z - k_{z0})^2 + (1/2\lambda_{MFP})^2} \tag{3.11}$$

where k_{z0} is the value of the out-of-plane momentum for a chosen photon energy. For a specific photon energy, the values of k_z probed in photoemission spectroscopy have a Lorentzian broadening centred at k_{z0} and FWHM of $1/\lambda_{MFP}$ as shown in Fig. 3.11(c). Therefore, the ARPES spectrum will be the superposition of the band structure sliced at different k_z, an effect already observed in the ARPES measurements of bulk $TiSe_2$ discussed in section 2.8.2. In this regard, the

ARPES spectrum of monolayer samples can be easier to interpret since their band structure is not dispersed along the out-of-plane direction.

3.3.1 Spectrum intensity

It is now clear how ARPES provides a direct probe of the band dispersion within a solid. In order to understand the intensity variations and the linewidth of the ARPES spectrum, the photoemission process needs to be decomposed into three independent events (three step model):

1. the photo-excitation of the system from a many particles N-electron initial state Ψ_i^N with energy E_i^N to a final excited state Ψ_f^N with energy E_f^N.

2. the travel of the excited electron to the surface which will depend on λ_{MPF}.

3. The emission of the excited electron from the solid passing through the surface potential barrier breaking the k_z conservation.

The intensity of ARPES spectrum will be the product of the probability associated with each event. Since the second and third steps have been already discussed above, I focus here on the optical transition described in the first step. This process will occur with a probability w_{fi} estimated by the Fermi's golden rule:

$$w_{fi} = \frac{2\pi}{\hbar}|\langle\Psi_f^N|H_{int}|\Psi_i^N\rangle|^2\delta(E_f^N - E_i^N - h\nu) \tag{3.12}$$

where the Hamiltonian H_{int} denotes the dipole interaction with the photon. If the characteristic relaxation time of the system is larger than the time the excited electron spends within the material, which depends on its kinetic energy, one can assume that the excited electron does not suffer any other scattering event during steps 2 and 3 and it is emitted from the surface preserving its total energy. Within this so-called sudden approximation, Ψ_f^N can be factorised into the photoemitted electron wavefunction $\phi_f(k)$ and the N-1 electron excited state of the system Ψ_m^{N-1} having energy E_m^{N-1}, as $\Psi_f^N = A\phi_f(k)\Psi_m^{N-1}$, where A is an antisymmetric operator that ensures the Pauli exclusion principle is satisfied. Thus, the energy of the final N-particle system can be rewritten as follows:

$$E_f^N = E_m^{N-1} + E_{kin} + \Phi. \tag{3.13}$$

Substituting the factorised wavefunction and the corresponding energies in eq. 3.12 the interaction matrix element takes the form of:

$$\langle \Psi_f^N | H_{int} | \Psi_i^N \rangle = \overbrace{\langle \phi_f(k) | H_{int} | \phi_i(k) \rangle}^{M_{fi}(k)} \overbrace{\langle \Psi_m^{N-1} | c_i | \Psi_i^N \rangle}^{c_{mi}} \tag{3.14}$$

where $M_{fi}(k)$ is the dipole matrix element, describing the transmission probability of a single-electron from state $\phi_i(k)$ to the final state $\phi_f(k)$. The second term $|c_{mi}|^2$ denotes the probability that the removal of an electron from the initial state leaves the (N-1) electron system in the excited state m, where c_i is the annihilation operator for the photoelectron. One can calculate the photoemission intensity I by summing w_{fi} over all the possible initial and final states available, obtaining:

$$I = \frac{2\pi}{\hbar} \sum_{fi} |M_{fi}(k)|^2 \sum_m |c_{mi}|^2 \delta(E_m^{N-1} + E_{kin} + \Phi - E_i^N - h\nu) \tag{3.15}$$

The term $\sum_m |c_{mi}|^2$ can be further related to the one-particle spectral function $A(k,\omega)$ that can be written as [83]:

$$\sum_m |c_{mi}|^2 = A(k,\omega) = \frac{1}{\pi} \frac{\Sigma''(k,\omega)}{(\omega - E_B(k) - \Sigma'(k,\omega)^2 + (\Sigma''(k,\omega))^2} \tag{3.16}$$

where E_B is the bare energy of the photoemitted electron, $\Sigma'(k,\omega)$ and $\Sigma''(k,\omega)$ are the real and imaginary parts of the proper self-energy that are connected by the Kramers-Kronig relation. In a correlated system, $\Sigma'(k,\omega)$ represents the renormalisation of the single-particle energy state due to the many-body interaction, while $\Sigma''(k,\omega)$ denotes its lifetime. For non-correlated system $\Sigma'(k,\omega) = 0$ and its $\Sigma''(k,\omega)$ is constant in energy denoting the finite lifetime of the electronic state due to impurity scattering. Considering the self-energy is also momentum independent, the lineshape in the energy distribution curve (EDC) assumes a symmetric Lorentzian profile as shown in Fig. 3.12. The intensity is further modulated by the matrix elements $|M_{fi}(k)|^2$ that depends on the light polarisation vector and the details of the initial and final state wavefunction. For instance, by changing polarisation or the kinetic energy of the final state by choosing a different photon energy, one can enhance or suppress the intensity of the band derived from certain orbitals compared to others. This effect has already been observed in the ARPES spectrum of the bulk $TiSe_2$ described in section 2.8.2, where the intensity of the p_z derived valence band at Γ vanishes for

$k_{\parallel} \sim 0$. Another factor affecting the spectrum broadening is the finite resolution of the analyser along the energy and momentum axis that can be taken into consideration by applying a 2D gaussian convolution $R(\omega, k)$ to the entire spectrum, resulting in:

$$I = [\sum_{fi} |M_{fi}(k)|^2 A(k,\omega) f(\omega, T)] * R(\omega, k) \tag{3.17}$$

where the Fermi function $f(\omega, T)$ has been included to consider the occupation of the initial states. A similar formula will be used in chapter 4 to simulate the ARPES spectrum of ML-$TiTe_2$.

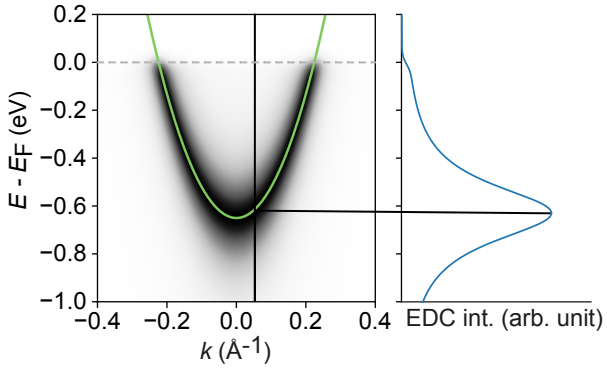

FIGURE 3.12: ARPES spectrum simulated assuming a parabolic bare band (green), a self-energy constant in energy and momentum. Under this condition the energy distribution curve EDC (blue) assumes a Lorentzian lineshape.

3.3.2 X-ray photoemission spectroscopy

ARPES is a powerful technique for analysing the momentum dispersion of the valence energy states at 10's eV below the Fermi level. The ionic core levels localised around the nucleus have, in general, much higher binding energies of the order of $\sim 100 - 1000$ eV, and thus they can be probed only using light sources with much higher energies such as X-rays. X-ray photoemission spectroscopy (XPS) is a sister technique of ARPES mainly dedicated to the analysis of the deep core levels of the elements comprising the material surface. Due to its high sensitivity in detecting small impurities concentrations, XPS is widely used for quality controls in the semiconductor and other industrial sectors, where the surface properties of the materials affect the performance of the manufactured device. Although the mean free path of the electron at such high energies is larger than the one obtained with ARPES, the surface sensitivity of XPS is still on the order of 10 Å as shown in Fig. 3.11(b). Even if the core electrons are not involved in chemical bonds, their energy is affected by the outermost electrons that partially screen the ionic Coulomb potential. Core levels of ions having different oxidation states or surrounded by different chemical environments

will have slightly different energies [82]. Qualitatively, a chemical shift towards higher binding energies is associated with higher oxidation states, while a negative chemical shift could be provoked by an enhanced metallic character of the sample. As in ARPES, the intensity of XPS peaks is proportional to the matrix element $|M_{fi}(k)|^2$, which in turn depends on the photon energy used during the experiment and on the concentration of the element on the sample surface.

3.3.3 ARPES systems

The electronic properties of ML films growth with the MBE are analysed *in-situ* using the ARPES system in our lab in St. Andrews. As discussed in the previous section, photoemission techniques are highly surface sensitive and require UHV environment in order to keep the sample surface clean from air contaminants. For this purpose, the sample is transferred from the MBE system through the UHV tunnel mentioned in section 3.1.2 kept at a base pressure of $\sim 10^{-11}$ mbar that ends in the ARPES preparation chamber (Fig. 3.13(a)). The sample is then moved into the upper chamber equipped with LEED and a six-axis manipulator that can be cooled to cryogenic temperatures using liquid He. The sample is mounted on the manipulator and transferred down into the proper ARPES analysis chamber, namely the lower chamber. Here, an ultraviolet (UV) light beam with energy $h\nu = 21.2$ eV is emitted from a He plasma generated inside the UV lamp. Then, the light passes through a toroidal mirror monochromator and is focused on the sample. The photoemitted electrons are detected by an analyser SPECS PHOIBOS 225 connected to the lower chamber having a base pressure of $\sim 10^{-11}$ mbar. This chamber is also equipped with an X-ray source SPECS XR50M for XPS analysis with higher photon energy. Here, high energy electrons (14 keV) are accelerated towards an Al anode exciting the electron core level of the metal. During the radiative relaxation of the electrons from the core levels with principal quantum number n=2 to the first shell (n=1), photons with energies 1486.6 eV (K_α) and 1557.5 eV (K_β) are emitted. This latter is then removed from the spectrum using a grazing monochromator.

Our equipment in St Andrews is particularly useful for the optimisation of the MBE growth and to obtain high-crystalline films with sharp bands. Further ARPES analyses were also performed at synchrotron facilities such as Diamond and SOLEIL light sources. Here, the electrons are first accelerated in a linear accelerator (LINAC) and then injected into a storage ring. When the electrons pass through an array of magnets (undulator), they travel in an oscillating trajectory emitting photons having a wavelength peaked at the oscillation period of the electron. Changing the magnet positions, different light polarisations can be generated. This synchrotron light passes

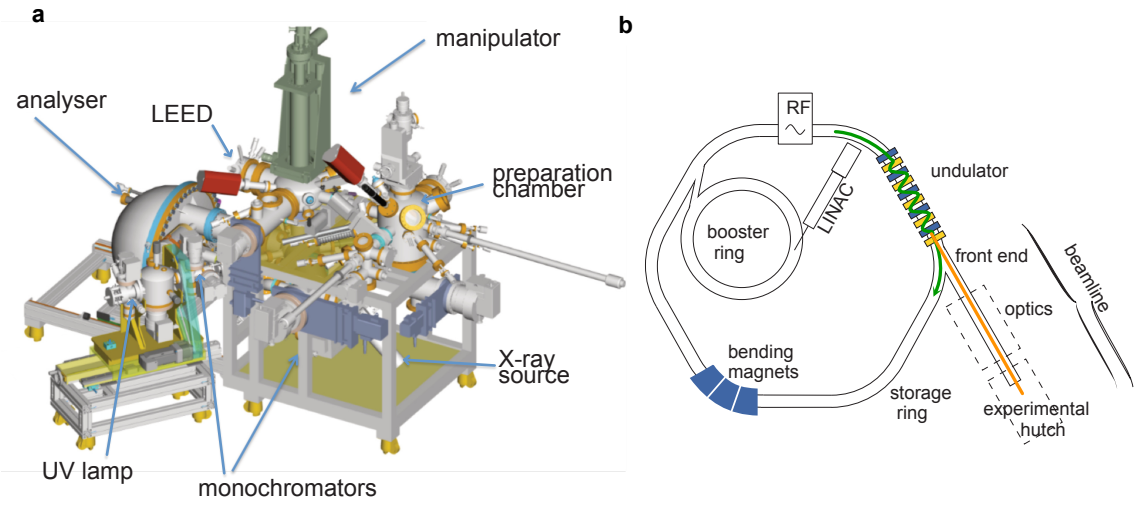

FIGURE 3.13: Schematics of the ARPES system in St Andrews (a) and the generation of synchrotron light (orange) when the electrons in the storage ring pass through an undulator. Adapted from [84].

through several optics comprising a monochromator and finally arrives at the beamline end-station where it is used for characterisation techniques such as photoemission. The possibility to change photon energy and light polarisation enables to vary the matrix elements and the out-of-plane momentum, which is useful to disentangle complex band structures with different orbital characters and resolve the 3D band structure of bulk single crystalline samples. However, the ARPES analysis at synchrotron requires exposing the sample in air during transport. In order to protect the surface of the monolayer film from air contamination, a reproducible capping/decapping procedure has been developed in our research group, which will be discussed in the next section.

3.4 Capping/decapping process

The monolayer TMD films measured at synchrotrons have been previously capped with a chalcogenide layer deposited in our MBE chamber after the growth. Depending on the composition of the film, two different kinds of capping are used. For $TiSe_2$, an amorphous Se layer is deposited by exposing the as-grown TMD surface to high Se flux for 10-20 minutes, long enough to observe the complete disappearance of the RHEED pattern. During this process, the sample is kept at the lowest possible temperature ($\sim 37^\circ$ C), in order to maximise the sticking coefficient of the ad-atoms. Since Se is much more reactive than Te, it cannot be deposited directly onto $TiTe_2$ or TiSeTe alloy, as it will completely selenise the TMD layer. However, neither a single Te capping layer can be used for telluride films since elemental Te is known to oxidise in air, leaving

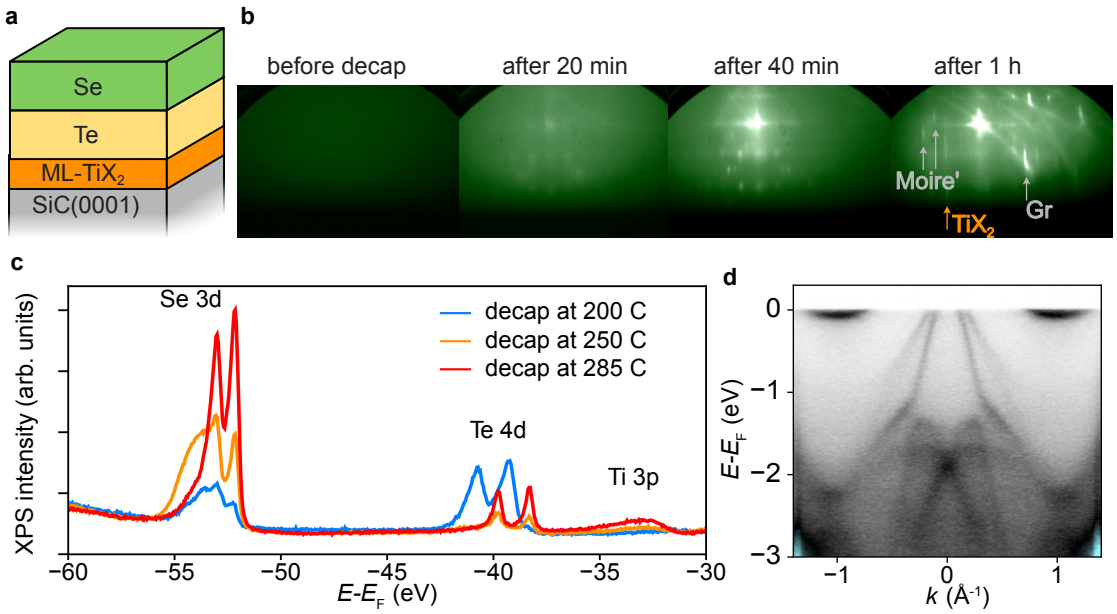

FIGURE 3.14: (a) Stacking of the Se/Te capping layer deposited to protect the ML-TMD film. (b) Typical evolution of RHEED during the decapping, showing the appearance of the pristine TiX_2 and substrate diffraction patterns. (c) The suppression of the shoulder at higher binding energies of the Se $3d$ and Te $4d$ XPS peaks points to the complete desorption of the capping layer. (d) ARPES spectrum of the pristine TMD surface measured at the end of the process.

a thin TeO_x layer on top of the TMD surface even after the capping removal [85]. To avoid the Te capping oxidation, a second Se layer is deposited on top (Fig. 3.14(a)), which remains well separated from the TMD surface in this way. In Fig. 3.14(b), the completely diffused RHEED pattern measured after the capping in GM2 indicates the full coverage of the film with an amorphous layer.

At the synchrotron end station, the sample is then heated up to $\sim 300^\circ$ C in order to desorb the capping layer and restore the pristine TMD surface. During the heating, the chalcogenide atoms rearrange into small crystallites forming a spotty RHEED pattern. After ~ 1 h these spots disappear, leaving behind the pristine diffraction pattern of the monolayer TMD and the Gr substrate. Another useful diagnostic tool to check the complete decapping of the surface is to monitor the chemical shift of the Se $3d$ and Te $4d$ core level peaks as shown in Fig 3.14(c). Both these core levels are split by spin-orbit coupling in a double peak whose energy separation is larger for the heavier Te compared to Se. Before the complete desorption of the protective layer, the XPS spectra show a shoulder at higher binding energies representing the signals from the elemental amorphous film still present on the surface. Gradually, these shoulders decrease in intensity as the Se/Te layers are desorbed at higher temperatures, leaving the sharp peaks associated with the

chalcogenide bound to the Ti atoms in the TMD film. Simultaneously, the weaker Ti $3p$ peak becomes more intense, pointing to the complete removal of the capping layers. The band structure of the TMD film (in this case, an alloy ML-TiSeTe) is then restored as shown in Fig 3.14(d). Therefore, the capping/decapping procedure presented in this section allows us to exploit the versatility of synchrotron light for studying the electronic states of Ti-based dichalcogenides.

Chapter 4

Dimensionality effect on the CDW in ML-$TiTe_2$

The original work discussed in this thesis focuses on the manipulation of the CDW phase transition in Ti-based dichalcogenides. As shown in chapter 2, the film thickness can strongly influence the CDW phase in many transition metal dichalcogenides [56, 86]. A particularly extreme case has recently been discovered in $TiTe_2$, where a CDW phase emerges only in the single-layer, while it is known to be absent in the bulk [28]. The origin of this transition and its dimensionality crossover is still poorly understood. In this chapter, an in-depth analysis of such unconventional lattice instability is presented, revealing the electronic band hybridisation occurring at the CDW transition in the monolayer configuration. The experimental results are rationalised in a minimal model that ultimately provides a natural explanation for the unusual dimensionality crossover of the CDW phase in $TiTe_2$. This simplified model will also be applied in Chapter 5 to the Ti-Se-Te alloys as a new approach for manipulating the CDW in Ti-based dichalcogenides.

This work was carried out in collaboration with:

- Dr Warda Rahim and Prof. Devid Scanlon at the university college London (UCL), who performed *ab-initio* calculations used to support experimental data and model calculations.
- The ARPES spectra reported in this chapter were measured by Matthew Watson, Akhil Rajan, Oliver J. Clark, Kaycee Underwood, Igor Marković, Edgar Abarca-Morales at the SOLEIL synchrotron in Paris, with the support of the beamline scientists Patrick Le Fèvre and François Bertran. Matthew Watson also collaborated on developing the minimal model used to simulate the band hybridisation in the monolayer.

- The crystal growth of monolayer $TiTe_2$ was developed by Akhil Rajan and Alisa Danilenko in our MBE system in St. Andrews, while the bulk $TiTe_2$ single crystal was provided by Kai Rossnagel from Kiel University.

I analysed and interpreted all the experimental data, the *ab-initio* calculations, and performed all other models and tight-binding calculations as well as the ARPES simulations.

4.1 Unusual CDW in monolayer $TiTe_2$

Bulk $TiTe_2$ has long been considered a prototypical example of a Fermi liquid system with a semimetallic ground state that remains stable even at very low temperatures [87–89]. The lack of any CDW transition is often associated with its weaker electron-phonon coupling [90] compared to its semiconducting sister compound $TiSe_2$ (section 2.8). Contrary to its selenide counterpart discussed in chapter 2, $TiTe_2$ is a semimetal having a substantial energy overlap between Ti d-derived conduction band and Te p-derived valence band. The larger extension of the Te $5p$ orbitals cf. the Se $4p$ enhances the hopping between the neighbouring Te and Ti sites leading to a wider valence band dispersion and a stronger hybridisation with the Ti d orbitals. A schematic of its Fermi surface is shown in Fig. 4.1(a) characterised by two barrel-like valence bands (green and red) dispersed along Γ-A and split by SOC, while the conduction band forms large elliptical electron pockets (orange) at M-L. These latter show a significant k_z-dispersion that modulates the size of the pockets in the $k_x - k_y$ plane. As previously discussed in chapter 2, the out-of-plane momentum is not conserved during the photoemission process, and the ARPES spectrum results from an integration of the 3D band structure in a k_z range that depends on the mean free path of the electrons in the solid. This effect is clearly visible in the measured Fermi surface in (b), which shows two concentric ellipses at M-L representing the Fermi contour in the $k_x - k_y$ plane of the rather small electron pocket at M and the larger contour at L. Changing the photon energy, the k_z-integration range can be centred at different values enhancing the sensitivity to the electronic states around a particular k_z. In Fig. 4.1(c), the photon energy ($h\nu = 143$ eV) is tuned to highlight the minimum of the conduction band at L ($k_z = \pi/c$) that reaches energies of $\sim -0.2eV$ below the Fermi level. Noticeably, its spectral weight is significantly broadened at higher energies following the dispersion of such band in the k_z direction. The other extrema at M becomes brighter for $h\nu = 123$ eV instead, where the electron pocket minimum lays just a few meV below the Fermi level. Also the valence bands at $k_{\|} = 0$ show differences between these two spectra. At Γ,

a third valence band associated to Te $5p_z$ states appears below the other two hole pockets, having a maximum at ~ -0.2 eV. As discussed in chapter 2 for bulk $TiSe_2$, the particular directionality of the p_z orbitals promotes a prominent k_z-dispersion of these states. These latter assume much lower energies ~ -2 eV at A, and therefore not visible in the spectrum measured with $h\nu = 143$ eV.

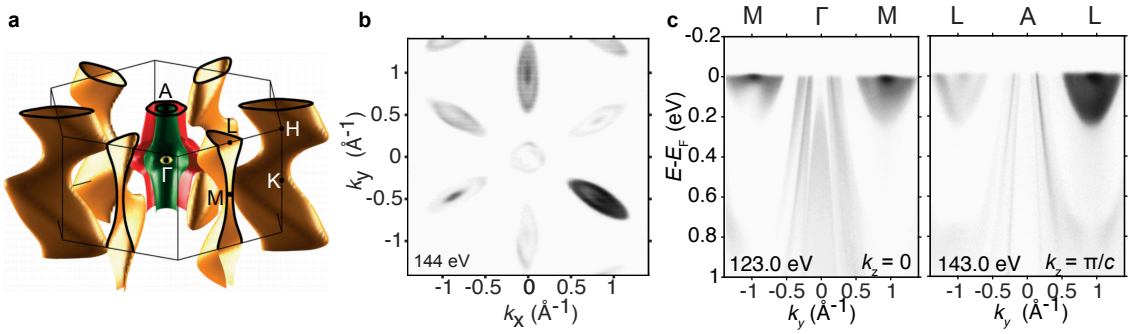

FIGURE 4.1: (a) Illustration of the Fermi surface in bulk $TiTe_2$ in the 3D k-space. (b) Fermi surface as measured with ARPES in the $k_x - k_y$ plane, resulting in a integration along k_z. (c) ARPES spectra of bulk $TiTe_2$ measured at T=20 K along Γ-M ($h\nu = 123$ eV) and A-L $h\nu = 143$ eV direction.

In contrast to the ARPES measurement of bulk $TiSe_2$, the spectra discussed here do not show any signature of CDW instability. Reducing the thickness down to the 2D limit, $TiTe_2$ has revealed an unexpected surprise. In 2017, Chen *et al.* successfully grew ML-$TiTe_2$ on a BL-Gr/SiC(0001) substrate using MBE and observed with ARPES the appearance of a valence band replica at low temperatures below the conduction band at M as indicated by the white arrow in Fig. 4.2(a). This is reminiscent of the folded hole pocket seen in the CDW phase of $TiSe_2$ discussed in chapter 2, pointing to the presence of a (2×2) CDW instability also emerging in the ML limit of $TiTe_2$, despite its absence in the bulk. Several questions were raised regarding the nature of this phase transition and its similarity with the highly controversial counterpart in the selenide compound. According to the conventional CDW mechanism, the band backfolding should occur at a q_{CDW} connecting large segments of the Fermi surface and promoting the opening of band gaps at the crossing point between the original and replica bands. Although TMDs typically show q_{CDW} not matching with the Fermi surface nesting due to their strongly k-dependent electron-phonon coupling, the CDW gap opening is of fundamental importance as it provides the ultimate energy gain for stabilising the ordered phase. In the ARPES data reported by Chen *et al.* instead, there is no clear signature of CDW gaps opening where the backfolded bands cross the conduction band at M as shown in Fig. 4.2(b). Nevertheless, a weak 60 % reduction in the film conductance at the Fermi level was measured by the authors using scanning tunnelling spectroscopy (Fig. 4.2(c)) and

ascribed as proof of a small pseudo-gap induced by the CDW transition. However, its counterpart in the ARPES band structure remains elusive, hidden in the spectrum broadening.

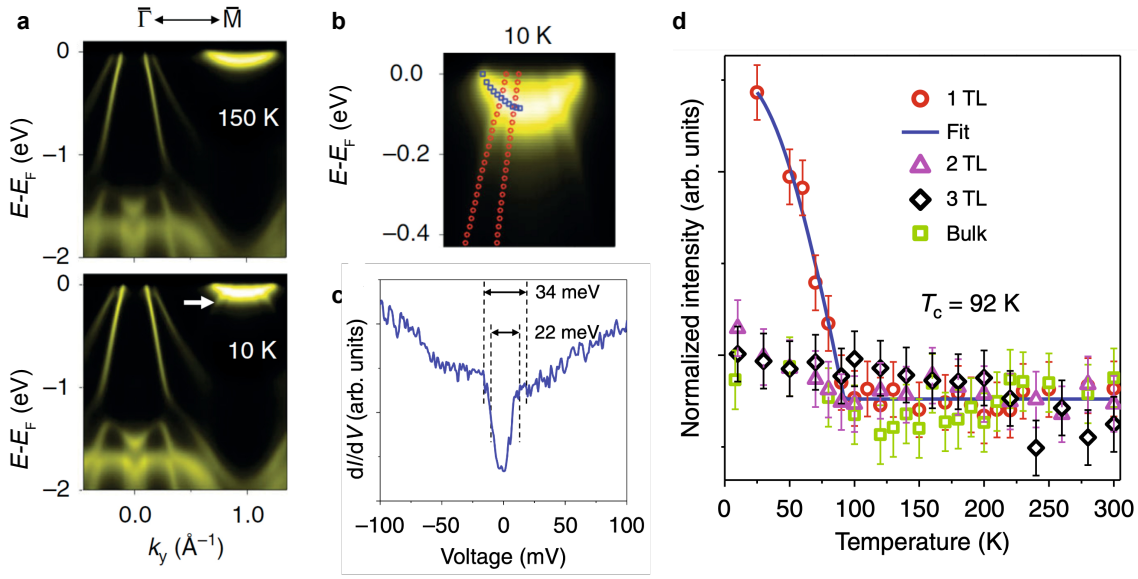

FIGURE 4.2: (a)ARPES spectrum of ML-$TiTe_2$ along Γ-M measured at 150 K (above) and at 10 K (bottom), this showing the backfolded spectral weight of the two valence bands at M (white arrow). (b) Magnification of valence band backfolding at M denoted by the red dots, assuming that the bands do not interact with the conduction band (blue dots). (c) STS spectrum showing the reduction in the film conductance at the Fermi level, taken as evidence of a pseudo-gap opening in the CDW phase. (d) Temperature modulation of the backfolded band intensity revealing the dramatic 2D-3D crossover of the CDW transition. Adapted from [28].

Another unusual behaviour of such phase transition is observed when the thickness of the $TiTe_2$ film is increased. Indeed, the CDW phase emerges exclusively in the monolayer, while it is completely suppressed in the bilayer and multilayer systems (Fig. 4.2(d)). Recent theoretical studies based on DFT calculations suggest different mechanisms to explain such dramatic 2D-3D crossover invoking a strain-driven lattice distortion in the monolayer induced by the substrate or a strong anharmonicity of the phonon dispersion that destabilises the CDW phase in the bulk crystal [91, 92]. A widely accepted explanation for this anomalous phenomenon hasn't been found yet, motivating the necessity for further both theoretical and experimental investigations. At first, we address the question if the lattice instability observed in ML-$TiTe_2$ is an intrinsic property of the material by calculating the vibrational spectrum of the 2D lattice using *ab-initio* methods.

4.2 Phonons in $TiTe_2$

Density-functional theory (DFT) calculations on bulk and monolayer $TiTe_2$ were performed using the same methodology used in chapter 2 to calculate the phonon spectrum of $TiSe_2$, successfully predicting the lattice instability in the selenide. In Fig. 4.3(a), the phonon dispersion of bulk $TiTe_2$ shows only positive phonon frequency indicating the structural stability of the crystal down to 0 K. For a free-standing single-layer instead, the same calculation reveals the softening of one vibrational mode at M, as shown in Fig. 4.3(b), similar to what was discussed in section 2.4.2 for lattice instability in ML-$TiSe_2$. Moreover, the softened mode at M and the phonon responsible for the CDW in $TiSe_2$ belong to the same A_u irreducible representation, strongly suggesting that the two parent compounds indeed undergo the same lattice distortion. Although our calculations don't provide any indication regarding the mechanism underpinning the phonon softening that can be of different nature for the two compounds, they successfully predict the emergence of such lattice instability in ML-$TiTe_2$ without invoking any external driving force, pointing instead to the intrinsic nature of this phase transition.

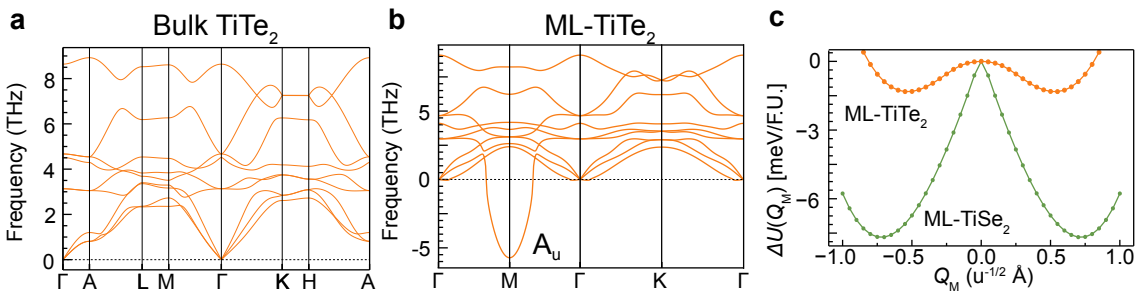

FIGURE 4.3: Phonon spectrum of bulk (a) and monolayer (b) $TiTe_2$, indicating the instability in the ML but not in the bulk crystal. (c) Tracking the potentials energy curve ΔU as a function of the corresponding normal-mode coordinates Q_M, with finite but small energy gain for the distortion; corresponding calculations for ML-$TiSe_2$ (green) indicate a much more pronounced instability at the same wavevector as for the Te case (orange).

A detailed comparison of the energy stabilisation provided by the lattice distortion in the selenide and telluride compounds can bring useful insight for a better understanding of such phenomenon. In Fig 4.3(c), the potential energy curves ΔU for monolayer $TiSe_2$ and $TiTe_2$ were calculated distorting the crystal following the "frozen-in" normal mode at Q_M for different phonon amplitudes. Their classical double well shape reveals the tendency of both systems to distort in order to reach the energy minimum at a finite "frozen-in" phonon amplitude. The smaller depth in the case of ML $TiTe_2$ indicates that the CDW ordering is more vulnerable under thermal fluctuation

and, therefore, would disappear at a relatively lower temperature compared to $TiSe_2$ ($T_c = 220$ K [39]) in agreement with the experiments.

The less stable periodic potential of ML-$TiTe_2$ is also reflected in the weaker spectral weight for the band replica observed in ARPES compared to the selenide. A remarkable energy shift of the top of the valence band is observed in the ordered phase of $TiSe_2$, a signature of strong band hybridisation which seems to be absent in the telluride ARPES spectrum in Fig. 4.2(b). In the following section, I discuss a detailed photoemission analysis aiming to identify the changes in the band structure of ML-$TiTe_2$ across its CDW transition.

4.3 Experimental evidence of hybridisation

High resolution ARPES measurements were performed at the synchrotron of SOLEIL in order to identify the elusive hybridisation in the CDW phase of monolayer $TiTe_2$. Fig. 4.4 (a) shows the ARPES spectra of the conduction and valence bands at different temperatures. As the temperature decreases, the characteristic backfolded bands appear at M crossing the spectral weight of the original conduction band. One of the standard methods to estimate at which temperature the CDW transition occurs consists of tracking the temperature dependence of the backfolded band intensity, which is directly related to the amplitude of the CDW periodic potential. For this purpose, I fitted MDCs (momentum distribution curves) at $E - E_F = -0.14$ eV shown in Fig. 4.4 (b) with four Lorentzian peaks representing the branches of the two backfolded bands (L1 and L4 for the outer valence band, L2 and L3 for the inner valence band), while a fifth Lorentzian accounts for the electron pocket tail. A linear background is also considered in the fitting model. The intensities of the Lorentzian peaks were normalised to their values at 14 K and plotted in Fig. 4.4(c), showing a clear onset of the CDW phase at T $\sim$ 110 K, similar but slightly higher than the value reported by Chen *et al.* [28]. Noticeably, the intensities of the Lorentzian peaks extracted from the fitting assume finite values even above T_c. Although a similar effect was observed in the sister compound $TiSe_2$ and related to its strong CDW fluctuation present in the normal state, here, I consider that the residual weight in the fits may just be due to background intensity since the tail of the conduction band significantly complicates the fitting when the backfolded intensity diminishes above T_c. However, such artefact does not affect the unambiguous onset of the backfolded valence band weight at 110 K. Therefore, I consider this temperature as the T_c of the CDW transition in ML-$TiTe_2$.

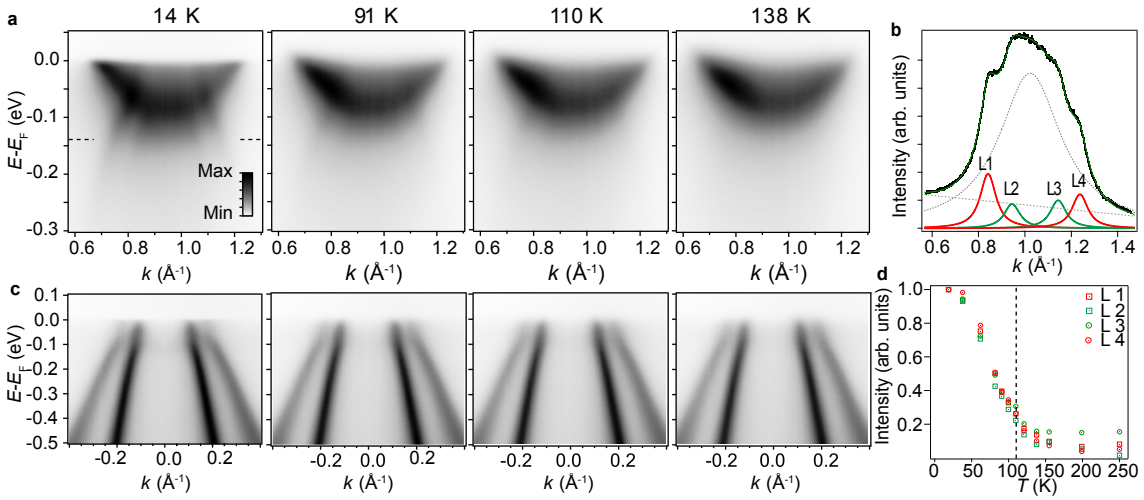

FIGURE 4.4: Temperature-dependent ARPES measurements of ML-$TiTe_2$ ($h\nu = 15$ eV) along the Γ-M direction and centred at the (a) M and (c) Γ points. (b) Fitting of MDC at $E - E_F = -0.14$ eV (along the dashed line in (a)) used to extract the intensity of the backfolded valence bands plotted in (d) for different temperatures, revealing the onset of the CDW transition (dashed line).

In contrast, the valence band at Γ shows a much more subtle variation across the temperature series. Here, a weak spectral weight appears at low temperatures (also shown in Fig. 4.5(b)) in between the inner valence band at energies ~ -0.1 eV. In Fig. 4.5(a), the second order derivative in energy of the spectra at 14 K helps to distinguish this small feature and reveals its parabolic dispersion consistent with a possible backfolded electron pocket. This hypothesis is also sustained by studying its temperature variation. Extracting EDCs at Γ from all the ARPES spectra in the temperature series in Fig. 4.4(a), this weak spectral weight generates a peak whose intensity decreases at high temperatures, as shown in Fig. 4.5(c). A small residual peak persists in the EDC plot even well above T_c, where no backfolded weight would be expected. In fact, detailed analysis shown in Fig. 4.5(d) indicates that there are two components: a small shoulder (blue) near the Fermi level and a sharper peak (orange) at slightly higher binding energy. The latter exhibits a strong temperature dependence and can be related to the backfolded conduction band weight, while the former is roughly temperature-independent, suggesting it derives from impurity scattering. The temperature dependence of the orange peak is extracted by fitting the EDCs with a two Lorentzian model convolved with the instrumental broadening and multiplied by a Fermi function. The background peak (p2) is fixed by the normal state data, while the amplitude and binding energy of the other component (p1) are allowed to vary freely. As evident in Fig 4.5(d), the binding energy of this component is, in fact, almost constant within experimental error (although this becomes impossible to track above T_c where its weight vanishes), while its intensity provides an adequate

representation of the CDW order parameter when compared with the MDC analysis reported in Fig 4.4(c). Noticeably, the energy position of the peak in the EDCs at Γ is $\sim$ 60 meV lower than the conduction band minimum observed at M. A possible cause of such a discrepancy is the partial rotational disorder in the $TiTe_2$ film, which is further discussed in section 4.7.1.

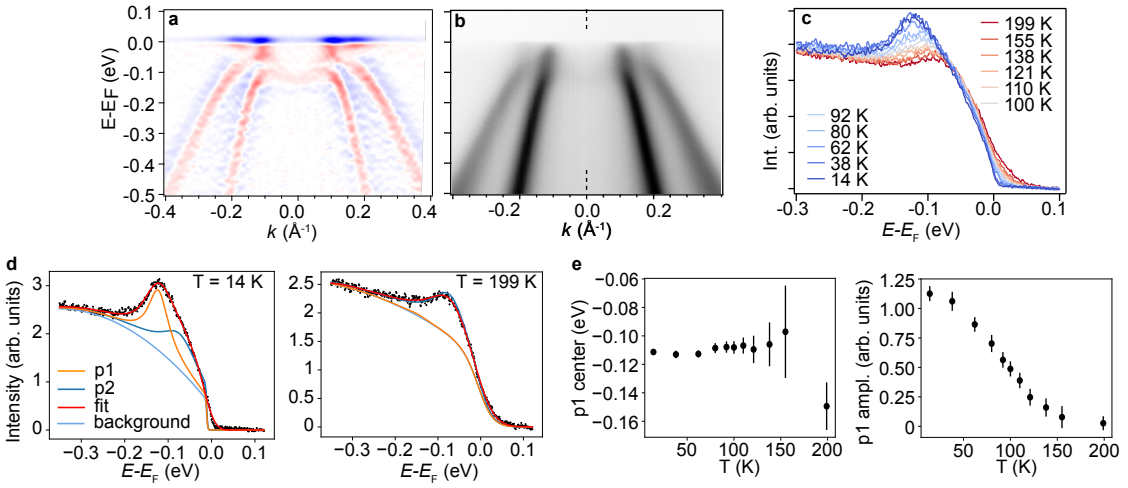

FIGURE 4.5: (a) Second order derivative in energy of the ARPES spectrum in (b), highlighting the dispersion of the backfolded conduction band at Γ. (c) EDCs extracted at Γ for the ARPES spectra measured at different temperatures. (d) Fitting of EDCs at low and high temperatures with two Lorentzian model. (e) center and amplitude of the p1 component representing the backfolded conduction band spectral weight.

Another noticeable change in the valence band ARPES spectrum is the decrease of the outer hole pocket intensity close to the Fermi level, while the inner valence band retains significant spectral weight all the way up to the Fermi level. Enhancing the matrix element of the outer valence band by measuring with $h\nu = 20$ eV, this feature can be slightly highlighted (Fig. 4.6(a)). Here, the outer valence band seems to develop a gap close to the Fermi level, while a more subtle discontinuity in the spectral weight of the inner valence band is also visible at ~ -0.1 eV. Nonetheless, a detailed analysis of the band intensity is needed in order to have a better understanding of such potential hybridisation features.

For this purpose, all the single MDCs between -0.18 eV up and the Fermi level were fitted with four Lorentzian peaks, one for each branch of the two valence bands, and a linear background as summarised in Fig 4.6(c). The so extracted intensity for the inner and outer valence bands were normalised at $E = -0.18$ eV and plotted in Fig. 4.7(a,b) respectively. It is now evident how the band intensities are affected by the CDW transition. The interpretation of such modulation can be simplified by calculating the difference between the intensities at T = 160 K and T=16 K normalised over the high temperature ones, as shown in Fig. 4.7 (c, d). The outer valence

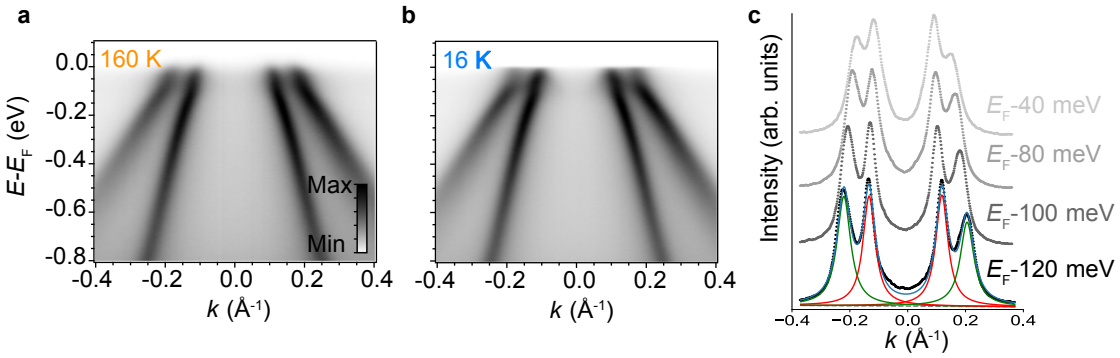

FIGURE 4.6: (a,b) ARPES measurements of ML-$TiTe_2$ ($h\nu = 20$ eV) along the Γ-M direction at 160 K and 16 K, respectively. (c) Fitting of single MDCs with four Lorentzian in order to track the valence band intensity.

band significantly loses spectral weight around -0.06 eV, while a similar but weaker decrease also occurs for the inner hole pocket around -0.11eV. Curiously, these energy values correspond to the interception points between the conduction and the backfolded valence bands at M, indicated with the green and grey arrows in the inset. The characteristic dips in spectral intensity point to clear evidence of the opening of band gaps in the electronic structure. Intriguingly, however, our measurements indicate that these gaps are highly asymmetric, with a pronounced minimum evident for the outer band, while only a small dip is observed at the band crossing energies for the inner valence band. I will show in the following sections that this reflects an orbital- and symmetry-selective band hybridisation, providing key insight into the stabilisation of CDW order in ML-$TiTe_2$.

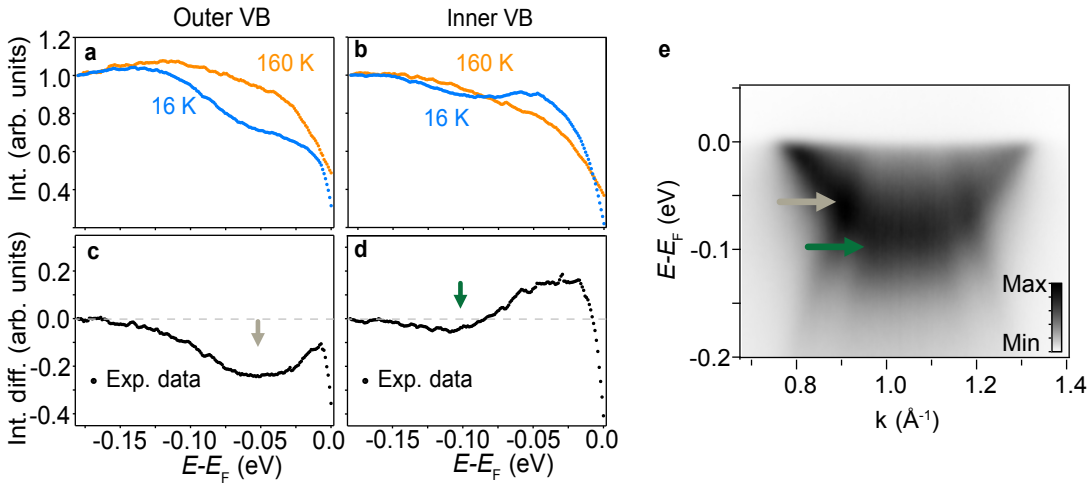

FIGURE 4.7: Change in the outer (a) and inner (b) valence band intensity due to the CDW transition. The difference between the high T and low T intensity curves is plotted in (c-d) revealing dips denoted by the green and gray arrows. These dips occur at the same energy where the backfolded conduction band intercept the valence band at M as visible in the ARPES spectrum in (e).

4.4 Tight-binding of ML-$TiTe_2$

In order to unveil how the electronic energy spectrum of ML-$TiTe_2$ is reshaped by the hybridisation occurring in its CDW state, a deeper understanding of its normal phase band structure is needed. As discussed in chapter 2, Slater-Koster tight-binding calculations can provide a useful description of electronic states on the basis of their atomic orbital character. Following the model used for ML-$TiSe_2$, the band structure of ML-$TiTe_2$ was calculated using the orbital basis in the octahedral coordinates $x'y'z'$, considering the three Te $5p$ orbitals p (p'_x, p'_y, p'_z) for each of the two chalcogen sites (Te(1) and Te(2)), and the five Ti $3d$ orbitals $d\gamma$ ($d_{x'^2-y'^2}, d_{3z'^2-r'^2}$) and $d\epsilon$ ($d_{x'y'}, d_{y'z'}, d_{x'z'}$). However, the input parameters required for such a calculation are not reported in literature and needs to be extracted from experiments or other *ab-initio* calculation. For this purpose, I fitted the simulated band structure along the M-Γ-K path to the DFT band structure provided by our collaborators, as shown in Fig. 4.8(a). The parameters were subsequently refined on the normal phase ARPES spectrum of ML-$TiTe_2$ measured at 203 K as shown in Fig. 4.8(b), obtaining the values reported in Table 4.1.

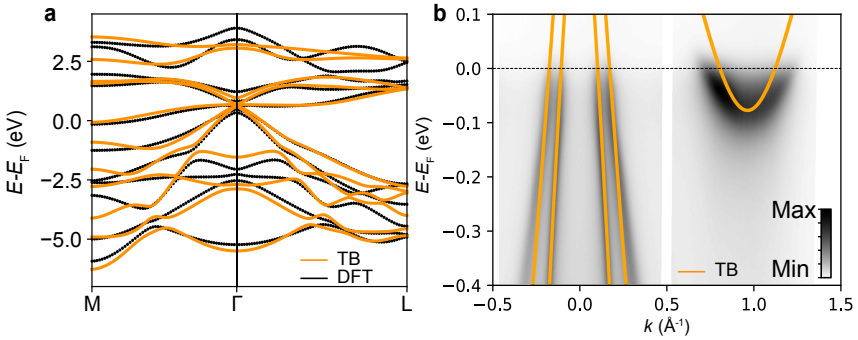

FIGURE 4.8: Fitting the tight-binding band structure of ML-$TiTe_2$ to the DFT calculation (a) and to the normal phase ARPES spectrum measured at T=203 K (b).

An on-site spin-orbit coupling term on the Te sites $\lambda = 0.38$ eV was included in order to match the splitting of Te-derived bands in the DFT and ARPES data. This value is much larger than the one used for the selenide compound (λ =0.105 eV) as Te is much heavier than Se. Moreover, the larger extension of the Te orbitals leads to overall larger hopping parameters ($t(pp)$) and stronger hybridisation with the Ti $3d$ orbitals compared to the selenide crystal. Instead, the crystal field splitting between $d\epsilon$ and $d\gamma$ (0.46 eV for the telluride) is smaller compared to the $TiSe_2$ (1.11 eV) due to the weaker electronegativity of Te. In Fig. 4.9, the Fermi surface of ML-$TiTe_2$ reflects its semimetallic character with two rather circular hole pockets centred at Γ and the elliptical

TABLE 4.1: Tight-binding parameters for ML-$TiTe_2$

On-site energies (eV)		
$e(p)$ = -1.958	$e(d\epsilon)$ = 0.256	$e(d\gamma)$ = 0.721
Hopping parameters (eV)		
$t(pp\sigma)_1$ = 0.904	$t(pp\sigma)_2$ = 0.581	$t(pd\sigma)$ = -1.618
$t(pp\pi)_1$ = -0.139	$t(pp\pi)_2$ = 0.075	$t(pd\pi)$ = 0.992
$t(dd\sigma)$ = -0.427	$t(dd\pi)$ = 0.216	$t(dd\delta)$ = -0.070

conduction pockets at M. The colourmap highlights the orbital polarisation of these latter obtained using the convenient octahedral basis for the Ti $3d$ states.

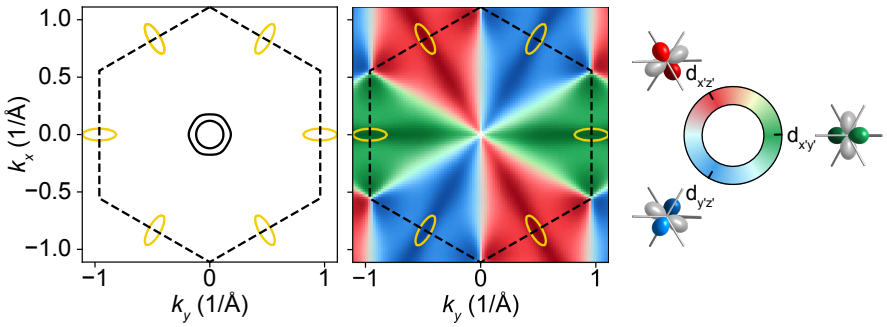

FIGURE 4.9: Fermi contour of the tight-binding band structure of ML-$TiTe_2$ and orbital character of the six elliptical electron pockets.

The global coordinates ($\{x, y, z\}$) are instead beneficial in analysing the orbital character of the valence bands as it allows to isolate the contribution of the Te $5p_z$ that remains confined at lower binding energies as shown in the calculation in Fig. 4.10(a) performed neglecting SOC. The other two valence bands crossing the Fermi level show an interesting orbital composition: the outer valence band character changes from a mainly Te $5p_y$ along Γ-M to a predominant Te $5p_x$ along the perpendicular direction Γ-K, while vice versa occurs for the inner band. Calculating the orbital character of the hole pockets in the 2D k-space around Γ reveals the two valence bands assume radial and tangential orbital textures as shown in Fig. 4.10(b). This property is also found in other materials like in the Rashba states of BiTeI [93] and the topological surface states of Bi_2Se_3 [94, 95]. In ML-$TiTe_2$, this behaviour can be ascribed to the different hopping amplitude of p_x and p_y orbitals in the triangular lattice, which in turns generates dispersions with different bandwidth and

effective masses.

As discussed in chapter 2 for ML-$TiSe_2$ the interaction between the electron spin and orbital angular momentum (SOC) split the degeneracy at the valence band top. Interestingly, in the telluride compound presented here, the inversion of the Te $5p$ and Ti $3d$ states at Γ induces the conduction band minimum at the BZ centre to assume a predominant Te $5p$ character, as shown in Fig. 4.10(a). This orbital character inversion promotes the SOC splitting at the electron band bottom instead of at the hole band top. However, the partial Te $5p$ orbital character is restored quickly at lower energies. The bands already show a predominant but not pure Te $5p$ character at the Fermi level where the tangential and radial orbital character remains largely unchanged by SOC.

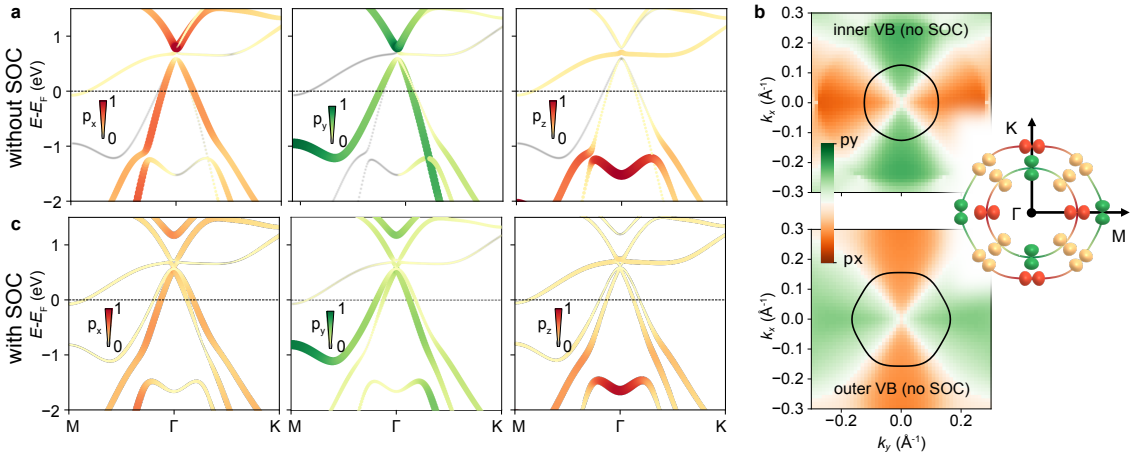

FIGURE 4.10: (a) Te $5p$ tight-binding orbital character along M$-\Gamma-$K path of ML-$TiTe_2$ without SOC. (b) p_x-p_y orbital character in the 2D k-space of the inner and outer valence bands extracted from the tight-binding in (a). (c) Including spin-orbit coupling (SOC) causes a partial mixing of the p_x and p_y states, but the dominant tangential and radial orbital character of the valence band states around the Brillouin zone centre is largely unchanged.

4.5 Orbital selectivity

Having established the low energy band structure of ML-$TiTe_2$ in its normal state, we can now address how its electronic states hybridise in its CDW phase. Our DFT calculations in section 4.2 have confirmed the (2×2) periodic potential emerging in ML-$TiTe_2$ is equivalent to the CDW ordering in the selenide, although weaker in the telluride. As discussed in section 2.8, the lattice reconstruction can be decoupled into three equivalent A_u phonon modes whose wave vectors are related to the three-fold axis of the system. Each of these modes is responsible for the backfolding of the Ti $3d$-derived conduction bands to Γ where they can hybridise with the two Te

5p$_{x,y}$-derived hole pockets. As shown in the previous section, the three electron pockets involved in the process derive from Ti $3d_{x'y'}, 3d_{y'z'}, 3d_{x'z'}$ which are, in fact, related by the three-fold axis. In the following, I will address the hybridisation of the valence bands with a single electron pocket Ti $3d_{x'y'}$ for simplicity. The method will be generalised later for the other two pockets by considering their three-fold symmetry relation.

The overlap between the Ti $d_{x'y'}$ and the Te 5p$_x, y$ orbitals is modelled on an octahedral unit cell as a minimal representation of the hybridisation between one electron pocket and the valence states. In Fig. 4.11(a,b), the p_x and p_y-derived valence states at Γ are represented together with the Ti $d_{x'y'}$ on the transition metal site. In the normal state, the undistorted octahedron has a mirror symmetry plane m, perpendicular to a C_2 rotational symmetry axis. The Ti 3d$_{x'y'}$ at the centre of the octahedron has even parity in both of these, while this is not true for the p_x and p_y-derived states, which possess an odd parity in C_2 or in m, respectively. Thus, the overlap integral $\langle p_x | d_{x'y'} \rangle$ is zero as p_x has opposite parity in m compare to $d_{x'y'}$, and also $\langle p_y | d_{x'y'} \rangle$ assumes zero value since the two orbitals have different parity in C_2. The lattice distortion related to a single A_u phonon displaces the atoms in the octahedron, as indicated by the black arrows breaking the m symmetry. As the symmetry constraint on $\langle p_y | d_{x'y'} \rangle$ is now lifted by the atomic distortion, the hybridisation between these states is allowed in the CDW phase. Instead, the C_2 symmetry is preserved and still continues to forbid the mixing between the p_x-derived state and the $d_{x'y'}$ orbital. Note that the Hamiltonian operator must commute with the system symmetry operators C$_2$ and m, thus also its matrix element $\langle p_y | H | d_{x'y'} \rangle$ are subjected to the same symmetry rules.

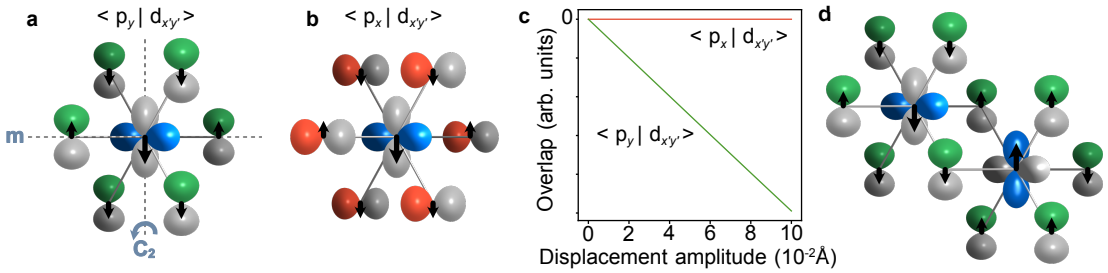

FIGURE 4.11: (a,b) Schematic of the $\langle p_x | d_{x'y'} \rangle$ (green) and $\langle p_y | d_{x'y'} \rangle$ (red) overlap in the octahedral unit cell. (c) Numerical evaluation of the overlap integrals in (a) and (b) as a function of the atomic displacement displacement caused by softening of an A$_u$ phonon mode at M (see black arrows in (a,b). (d) Schematic of the overlap in a (2×1) unit cell.

To show these above arguments hold, I have numerically calculated the overlap matrix elements explicitly taking a $(121 \times 121 \times 121)$ cubic mesh considering only the tesseral harmonics

form of the orbitals wave functions. In this case, the radial part of the wave function can be neglected because it possesses a spherical symmetry and, thus, does not introduce any other symmetry constraint. Since Ti is lighter than Te, its displacement is assumed to be nine times larger than the Te ones. The overlap between p_y and $d_{x'y'}$ orbitals increases linearly with the displacement amplitude, while $\langle p_x | d_{x'y'} \rangle$ remains zero irrespective of the atomic distortion. This result indicates that the symmetry breaking at the CDW transition allows a new hybridisation path between the $d_{x'y'}$-derived electron pocket and p_y-derived valence states at Γ.

Even though the valence and the conduction bands don't cross each other exactly at Γ, this argument is still formally valid within the entire Brillouin zone. As seen in Chapter 2 the electronic states in a crystal are described by Bloch waves composed by a periodic function $u(r)$ multiplied by a complex phase factor that depends on k. Taking in consideration the orbital decomposition described above, $u(k)$ can take the form of $|p_{x,y}\rangle$ and $|d_{x'y'}\rangle$ repeated on the entire crystal. The overlap integral can be rewritten as follows:

$$\left\langle e^{ik_h r} p_{x,y} | e^{ik_e r} d_{x'y'} \right\rangle = \left\langle p_{x,y} | e^{i\pi/ar} d_{x'y'} \right\rangle \tag{4.1}$$

where k_h and k_e are the momentum for the hole (h) and electron (e) pockets. In the CDW phase the backfolding act as a rigid translation of the electron pocket, thus $k_e = k_h + \pi/a$. Substituting this latter and grouping the two complex factors, the integral takes the same form as if calculated exactly at Γ, but with an additional modulation of the $d_{x'y'}$-derived state having a (2×1) periodicity as displayed in Fig. 4.11(d). In the upper-left octahedron, the grey lobe of the d orbitals is pushed closer to the green lobe of the p orbitals by the lattice distortion, giving a negative contribution to the integral. Since both the d-orbital phase and the lattice displacement change sign in the lower-right octahedron, the same negative contribution is given to the integral, proving that the calculation can be effectively restricted into a (1×1) unit cell as done above.

The orbital selectivity discussed so far for the $d_{x'y'}$-derived conduction band hybridisation can be generalised for the other two electron pockets by rotating the Ti d-orbital by $120°$ and considering the relative C_2 axis. Their hybridisation will be allowed only with the p-orbital component of the valence bands that is parallel to the relative C_2 axis. The argument discussed in this section is formally valid only for pure $d_{x'y'}$ and $p_{x,y}$-derived Bloch states. Although the conduction and valence bands of ML-$TiTe_2$ are mainly formed by these orbitals, they possess other orbital contributions that haven't been addressed here. In principle, one can estimate the hybridisation due to

the lattice distortion (Δ) between all the orbitals used in the tight-binding model and then calculate the effective hybridisation term between two Bloch states of the band structure as the linear combination of such Δ multiplied by the relative orbital character of these states. For the sake of simplicity, only Ti t_{2g} and p_x, y orbitals will be considered in the next section as the minimal basis to simulate the effects of the CDW distortion on the low energy band structure.

4.6 Minimal model

In this section, an intuitive model is introduced to describe the orbital selective hybridisation occurring in the CDW phase of ML-$TiTe_2$. The states involved in the process are the three electron pockets e_1, e_2 and e_3 backfolded at Γ and the two hole pockets h_{in} and h_{out} denoting the inner and outer valence bands, respectively. Simple polynomials are chosen to describe the band dispersions in the normal states: e_1, e_2 and e_3 take the form of 2D elliptic paraboloids, while the two hole bands are approximated by circular non-parabolic band as their hexagonal warping is negligible for energies close to the Fermi level:

$$e_1 = e_c + \mu k^2 \tag{4.2}$$

$$e_3 = e_c + \mu(-\frac{1}{2}k_x + \frac{\sqrt{3}}{2}k_y)^2 + \nu(-\frac{\sqrt{3}}{2}k_x - \frac{1}{2}k_y)^2 \tag{4.3}$$

$$e_3 = e_c + \mu(-\frac{1}{2}k_x - \frac{\sqrt{3}}{2}k_y)^2 + \nu(\frac{\sqrt{3}}{2}k_x - \frac{1}{2}k_y)^2 \tag{4.4}$$

$$h_{in} = e_h + (\sqrt{2} - \sqrt{2 + 4\alpha_{in}\mu_{in}k^2})/(2\alpha_{in}) \tag{4.5}$$

$$h_{out} = e_h + (\sqrt{2} - \sqrt{2 + 4\alpha_{out}\mu_{out}k^2})/(2\alpha_{out}) \tag{4.6}$$

where e_h and e_c are the on-site energy for the conduction and hole pockets. μ and ν are the effective masses along the major and minor axis of the elliptical parabola, while μ_{in} and μ_{out} are the ones for the circular valence bands. α_{in} and α_{out} are the non-parabolic terms for the hole bands derived from the $k \cdot p$ approximation [96].

The hybridisation between the three backfolded electron pockets and two valence bands is captured by off-diagonal terms of a (5×5) Hamiltonian. All such hybridisation terms have to satisfy the orbital constraints described in the previous section. For instance, the electron pocket derived from Ti $3d_{x'y'}$ (e_1) has an non-zero hybridisation strength Δ only with the p_y orbital component of the valence states. Thus, the off-diagonal terms can be considered as Δ multiplied by a form factor representing the p_y character of the hole pockets. Since the inner and outer valence

bands have a radial and tangential orbital texture (section 4.4) respectively, the form factor takes the form of $cos(\theta)$ for h_{out} and $sin(\theta)$ for h_{in}, where $\theta = arctan(k_y/k_x)$ as shown in Fig. 4.12(a). Considering the three-fold symmetry relation between the three electron pockets, the Hamiltonian matrix takes the form:

$$\mathcal{H} = \begin{pmatrix} e_1 & 0 & 0 & \Delta cos(\theta) & \Delta sin(\theta) \\ 0 & e_2 & 0 & \Delta cos(\theta-\frac{2\pi}{3}) & \Delta sin(\theta-\frac{2\pi}{3}) \\ 0 & 0 & e_3 & \Delta cos(\theta-\frac{4\pi}{3}) & \Delta sin(\theta-\frac{4\pi}{3}) \\ \Delta cos(\theta) & \Delta cos(\theta-\frac{2\pi}{3}) & \Delta cos(\theta-\frac{4\pi}{3}) & h_{out} & i\lambda_{SO} \\ \Delta sin(\theta) & \Delta sin(\theta-\frac{2\pi}{3}) & \Delta sin(\theta-\frac{4\pi}{3}) & -i\lambda_{SO} & h_{in} \end{pmatrix} \tag{4.7}$$

Spin-orbit coupling λ_{SO} is included for the valence bands in order to take into account their energy splitting at Γ and the partial mixing of their orbital texture.

Turning on Δ, the hybridised Fermi surface develops gaps whose amplitude is modulated by the orbital character of the valence bands as shown in Fig. 4.12(b) for three different Δ values. The influence of the orbital selectivity is also evident taking a cut of the band structure along a high symmetry direction. For example, along Γ-M only a small gap is opened between e_1 and h_{in} as the inner valence state has a predominantly p_x character, while the hybridisation generates a larger energy split for h_{out} as shown in Fig. 4.12(c). The opposite occurs along $\Gamma - K$ where the orbital character of the valence band is inverted. The overall hybridisation scheme is qualitatively consistent with the DFT calculation of ML-$TiTe_2$ in the (2×2) phase reported so far [92], [91], proving that our minimal model correctly considers the essential system symmetries.

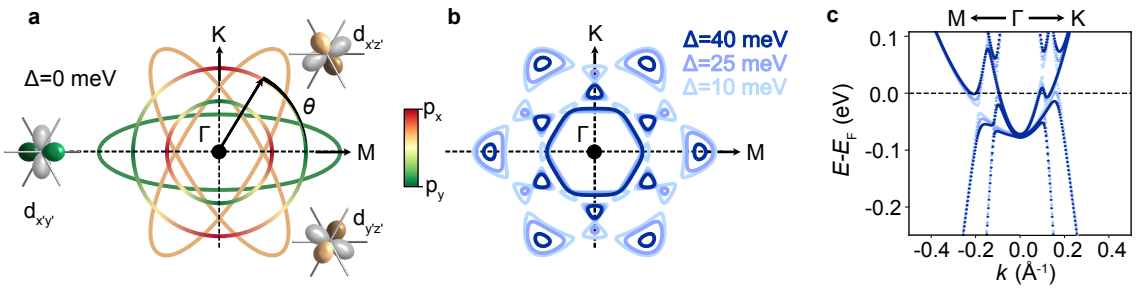

FIGURE 4.12: (a) Fermi surface of the five bands chosen as basis for our minimal model. Their hybridisation is allowed if the states have compatible orbital character, i.e., the same colour. (b) Fermi surface predicted for different hybridisation strengths (Δ). (c) Hybridised bands along Γ-M and Γ-K for the same simulation in (b).

4.6.1 Shift of the chemical potential

As the hybridisation becomes larger, more electronic states are pushed above the Fermi level, which might cause the non-physical artefact of losing electrons from the system. Considering

the shift of the chemical potential across the CDW transition is important in order to avoid such unrealistic effects and to compare our model with the experimental ARPES data. The number of electrons per unit cell (n) was extracted by integrating the occupied DOS between 0.1 eV to -0.3 eV for each Δ (Fig. 4.13(a)). Since the number of electrons has to remain constant across the transition, we determine the new chemical potential by minimising the quantity $n(0) - n(\Delta, E_F)$. Applying the chemical potential shift shown in Fig. 4.13(b), the new Fermi level is shifted accordingly and the occupied DOS recalculated (Fig. 4.13(c)), showing the effective conservation of the total electron number.

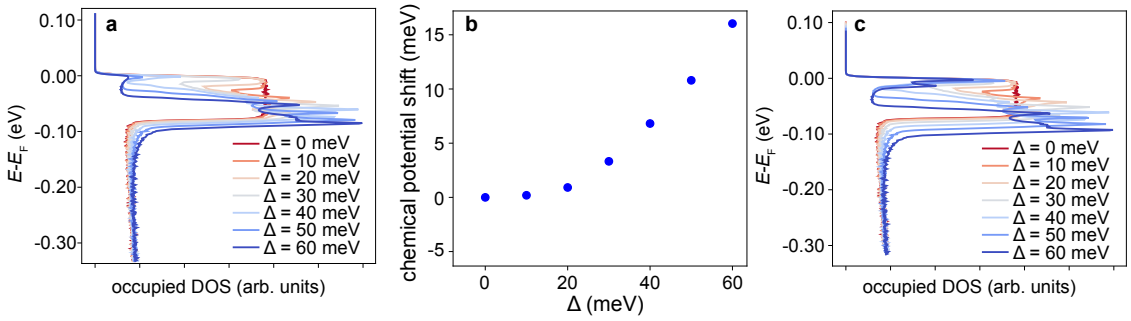

FIGURE 4.13: (a) Uncorrected occupied DOS for different Δ calculated with the minimal model at constant $T = 16$ K. (c) shift in the chemical potential in order to preserve the number of electrons. (c) Occupied DOS corrected by applying the chemical potential values in (b). Now all the curves have the same area.

4.7 ARPES simulation

Having established the hybridisation scheme, we can directly compare the experimental data in Fig. 4.6(a,b) to our minimal model by simulating the spectral weight derived from each band. As discussed in chapter 3, the ARPES intensity can be calculated using the following equation:

$$I(k,\omega) = [M(k)A(k,\omega)f(T,\omega)] * R(\Delta k, \Delta\omega) \tag{4.8}$$

where M is a functional form of the matrix element term $\sum_{fi} |M_{fi}(k)|^2$ in eq. 3.17, $f(T,\omega)$ is the Fermi-Dirac distribution at temperature T. The entire expression is then convoluted with a 2D Gaussian (R) to simulate the experimental energy and momentum resolution. For simplicity, the spectral function $A(k,\omega)$ can be considered as a Lorentzian broadening along the energy axis ω

centred at the electronic energy level $e_b(k)$:

$$A(k,\omega) = \frac{\Sigma_b}{(\omega - e_b(k))^2 + \Sigma_b^2} \tag{4.9}$$

where Σ_b is the Lorentzian $FWHM$. As experimentally observed, the matrix element for the p-derived and d-derived states are very different at Γ and are expected to approximately follow that of the original band character [97, 98]. Moreover, the outer valence band intensity is weaker at positive k, while the inner valence band doesn't show any significant modulation in k as visible in Fig. 4.6(c). This effect is taken into account by assuming M to linearly vary in k and be dependent on the original band character C_b:

$$M = \sum_{b=1}^{5} m_b C_b^2 k + n_b C_b^2 \tag{4.10}$$

where m_b and n_b are linear coefficients for each band $b = (e_1, e_2, e_3, h_{in}, h_{out})$. The input parameters were extracted by fitting the intensity of the simulated spectrum directly on the experimental data measured above T_c, enabling a careful optimisation of the band positions for both the conduction band and valence band as shown in Fig. 4.14(a). The ratio between the effective mass along the major and minor axis of the elliptical conduction pocket was instead estimated from the Fermi surface of the bulk compound shown in Fig. 4.1 and assumed to be the same for the monolayer crystal.

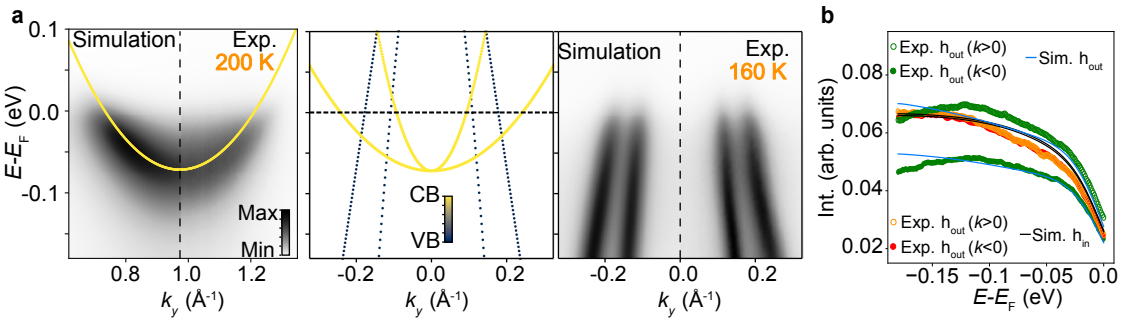

FIGURE 4.14: (a) Comparison between the ARPES simulation of the bare bands calculated by the minimal model and the experimental data, for the high temperature normal phase and the hybridised CDW phase at $T = 16$ K. (b) The simulation replicate closely the intensity variation of the inner and outer valence band extracted by fitting MDC.

As noted in section 4.3, further intensity modulation is present in the spectrum of the hole bands where the intensity of both h_{in} and h_{out} decreases monotonically from -0.16 eV up to

the Fermi level for both the high and low T spectra. Such feature seems to be temperature-independent, and it might be due to the presence of defects in the ML-$TiTe_2$ or a more pronounced d-character at higher binding energy. In order to achieve a better agreement with the experimental data, we include a temperature-independent intensity decay, I_{dec}, of the from:

$$I_{dec} = \begin{cases} cos\left[\frac{\pi(\omega - E_i)}{2(E_f - E_i)}\right], & \text{if } \omega \leq E_i \\ 1, & \text{if } \omega > E_i \end{cases} \tag{4.11}$$

where the coefficients E_f and E_i were determined fitting the high temperature data and kept constant for all the simulations at different temperatures. Thus, this contribution will be cancelled out by calculating the intensity difference between the high and low temperature data as in Fig. 4.6(f,g). Using the same procedure discussed in section 4.3, the experimental and simulated band intensities are extracted by fitting the respective spectra around Γ and plotted in Fig. 4.14(b). The simulation is in good qualitative agreement with the experimental intensities, replicating the intensity decay described by eq. 4.11 and the pronounced k-dependent modulation of the outer valence band.

In Fig. 4.14(a), the optimised conduction dispersion is backfolded to Γ and crosses the hole pockets (blue dots) at different energies below the Fermi level for the inner and outer valence bands. When the other two replica hole pockets cut the Γ M direction, they form two degenerate bands with larger effective mass that cross both the hole pockets above the Fermi level. Using these five bare bands as basis for our minimal model, a realistic description of the CDW hybridisation can be obtained. In Fig. 4.15(a), the low energy spectrum of ML-$TiTe_2$ is simulated by considering a hybridisation strength $\Delta = 42$ meV, inducing the band gap opening at the crossing points discussed above. Assuming this new band configuration, the ARPES spectrum of the hybridised state was simulated and fitted to the experimental data in order to optimise the broadening and intensity parameters of the simulation. As shown in Fig. 4.15(b), the simulated spectrum accurately replicates the subtle evolution of the ARPES spectrum across the CDW transition, such as the reduced outer valence band intensity around the Fermi level. Since the intensity of the three conduction bands is abruptly suppressed by the matrix elements at Γ, the spectra are dominated by the states with strong valence band character (dark blue in bare band plots).

As discussed in the previous section for the experimental data, the intensity of the simulated bands is extracted by fitting MDCs between -0.18eV and the Fermi level. The intensity difference

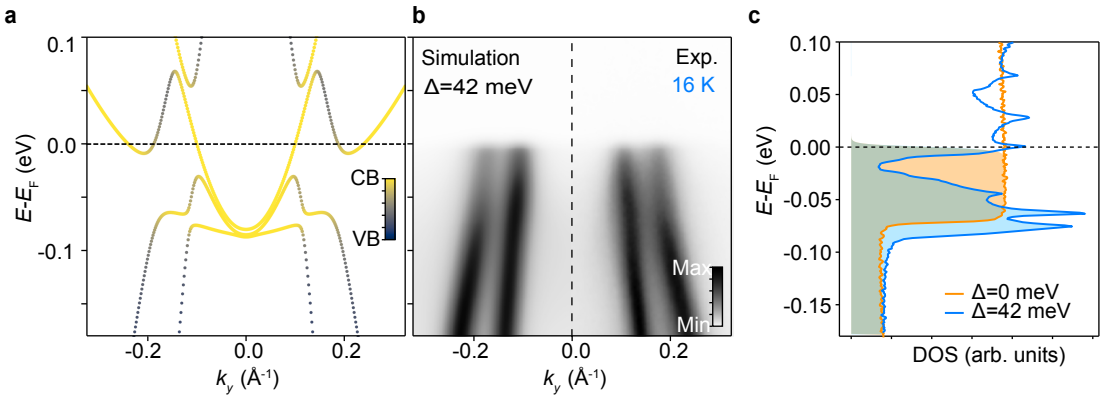

FIGURE 4.15: (a) Hybridised band structure of ML-$TiTe_2$ calculated using the minimal model with $\Delta = 42$ meV. The colorscale denotes the conduction (CB) and valence (VB) character. (b) Comparison between the ARPES simulation of the bare bands in (a) and the experimental data in the CDW phase at $T = 16$ K. (c) Calculated DOS from the model, indicating the effects of band hybridisation, providing a significant electronic energy gain in the occupied states (shaded region). Spin-orbit coupling is included for all the shown calculations.

between the unhybridised and hybridised simulated band intensities is shown in Fig. 4.16 (red lines) for three different Δ values. Increasing the hybridisation strength, the dip in the outer valence band intensity becomes wider and more pronounced since the simulated CDW gap becomes larger. The best match with the experimental intensity is obtained for Δ = 42meV, where also the simulated inner valence band curve well replicates the dip at ~ -0.1 eV and the successive increment of the data extracted from experiments. Thus, our model provides a suitable rationale for the ARPES spectrum evolution across the CDW transition of ML-$TiTe_2$. However, due to the simplified band scheme and the approximation used to simulate the spectra, I cannot perfectly replicate the complexity of the experimental data limiting the accuracy with which Δ can be determined. For example, the presence of a partial rotational disorder in the deposited film might induce modifications in the ARPES spectrum that are not taken into account by our simulation, as discussed in the next section.

Another important consideration can be extracted by calculating the density of states (DOS) in the 2D k-space for the un-hybridised and hybridised bare bands, as shown in Fig. 4.15(c). The hybridisation induces a substantial drop in the occupied DOS just below the Fermi level, which significantly decreases the total electronic energy consistent with the incomplete gap in the STS spectrum measured by Chen *et al.* (Fig. 4.1). The minimal approach undertaken here provides a flexible tool to extract a rough estimate of the CDW gap from ARPES measurements. The results discussed above firmly establish that hybridisation gaps open up at the CDW transition and that they are modulated by orbital selectivity imposed by the symmetry of the system. Ultimately, this

mechanism provides a route to lower the electronic total energy and stabilise the CDW ordering.

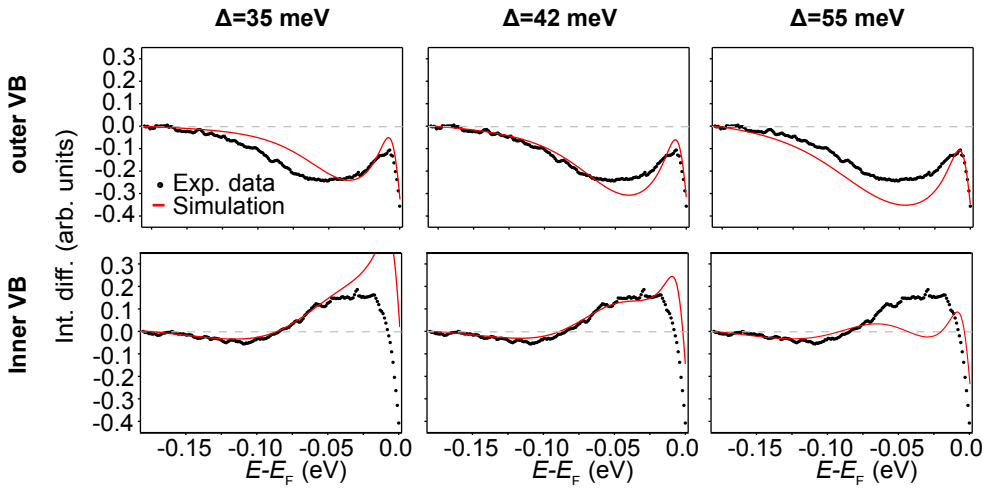

FIGURE 4.16: Intensity difference between the hybridised and unhybridised bands extracted by fitting the ARPES simulated spectra (red lines) for three different Δ values. A good agreement with the experimental data (black dots) is achieved for $\Delta = 42$ meV.

4.7.1 Effect of the rotational disorder

The weak interaction between the sample and substrate allows to investigate the electronic structure of the deposited film in a "quasi-freestanding" configuration. However, the resulting relaxation of the epitaxial registry constraint between the two lattices induces a certain degree of freedom in the rotational orientation of the $TiTe_2$ crystal domains, as evident in the Low-Energy Electron Diffraction (LEED) image shown in Fig. 4.17(a). Fitting the $TiTe_2$ Bragg intensity following the radial path in Fig. 4.17(a, b) I estimate an azimuthal FWHM = 11°. The effect of this partial rotational disorder on the ARPES spectrum can be simulated along Γ-M by cutting the 2D hybridised-band dispersion calculated with our minimal model at a slightly different orientation. As evident in Fig. 4.17 (c), this partial orientational disorder of the film does not significantly impact the spectra of the valence bands at Γ, while at M, the Fermi surface is spanned almost entirely by the misaligned radial cuts. Thus, the broadening of the ARPES spectrum tends to gradually increase and move towards larger k as visible in the bare band plot around Γ and M shown in Fig. 4.17 (d). Here the gaps are no more resolved in agreement with the observation of an almost continuous conduction band in the ARPES spectrum at M measured at 14 K shown in Fig. 4.4 (c). Another relevant consequence is the large broadening at the bottom of the electron pocket, which is skewed to higher binding energy due to the additional cut away from the exact Γ-M direction.

Considering the ARPES spectrum resulting from the sum of such dispersion, the bottom of the conduction band spectral weight at M appears at higher binding energy with respect to a hypothetical sample without any rotational disorder. However, the weak spectral weight related to the backfolded conduction band at Γ will be almost not affected by such an artefact, and it will appear at slightly higher binding energy. Such discrepancy is indeed visible in our ARPES spectrum as discussed in section 4.3. Considering the low temperature spectrum in Fig. 4.4(c), the bottom of the conduction band at M lies at -0.08 eV, while its weak backfolded spectral weight shows its minimum at ~ -0.12 eV at Γ, where rotational disorder doesn't introduce any additional asymmetric broadening in energy. While the rotational disorder strongly influences the spectra at M, the modelling here shows that it has only a rather small influence on the spectra measured close to Γ. Since the analysis presented in the previous section focused on the electronic dispersion around the BZ centre, our findings are robust against this rotational disorder.

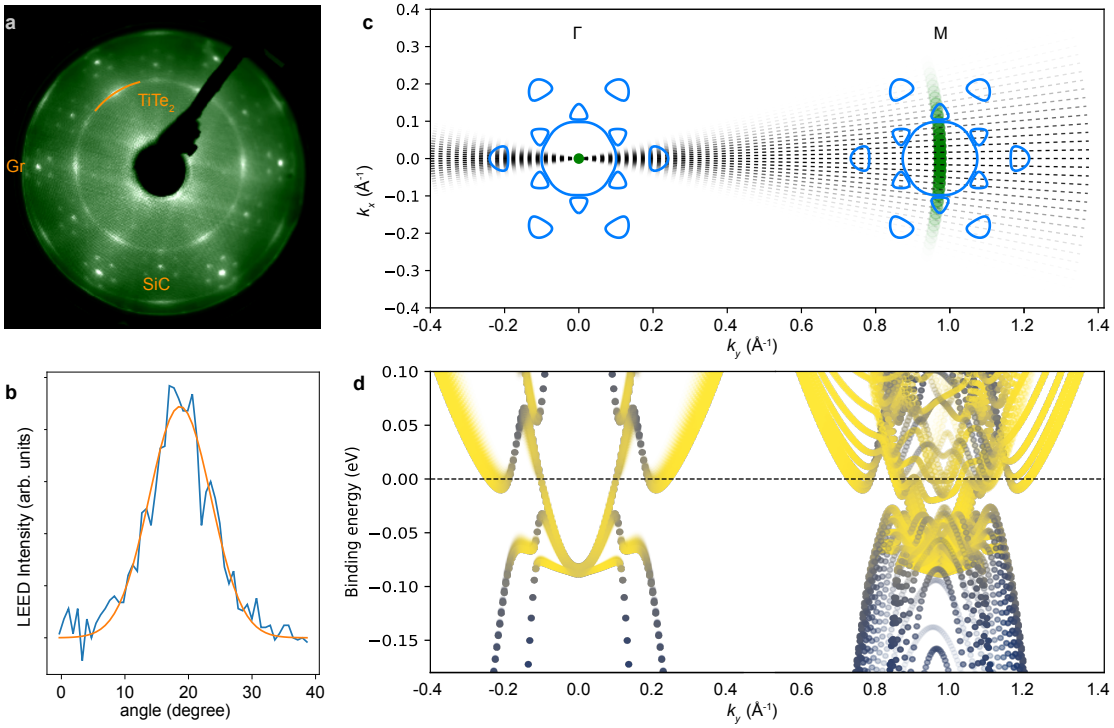

FIGURE 4.17: (a) LEED pattern of the sample measured with ARPES in the previous section revealing a substantial rotational disorder of the grown film. (b) Extraction of the rotational disorder magnitude by fitting the $TiTe_2$ Bragg peak along the orange radial cut in (a). (c) Calculated Fermi surface of $TiTe_2$ in the CDW phase with the misaligned cuts used to simulate the orientational disorder at Γ and M. (d) Bare bands along all the misaligned Γ-M cut generating an additional broadening of the ARPES spectrum, especially at M.

4.8 Bulk vs monolayer

The lattice instability in $TiTe_2$ is drastically affected by the dimensionality of the system as no CDW phase has been observed in multilayer $TiTe_2$. In this section, our minimal model is applied to the bulk case to understand how the 3D band dispersion in the bulk crystal affects the electronic energy gain uncovered for the ML system above. As described in section 4.6 our minimal model largely depends on the energy position of the band and their orbital character. Bulk $TiTe_2$ presents a 3D band structure where the size of the electron and hole pockets varies along the out-of-plane momentum k_z. The conduction band states yield large Fermi pockets for $k_z = \pi/c$, while they are barely occupied for $k_z = 0$. The opposite trend is observed for the valence bands, which are pushed at higher energy approaching the BZ centre. Taking advantage of the intrinsic broadening of the ARPES k_z resolution, the valence and conduction band dispersions at $k_z = 0$ and at $k_z = \pi/c$ can be extracted from the ARPES spectra in Fig 4.18(a) (dark blue bands) using the polynomial bands introduced in section 4.6. The p_z-derived band appearing at Γ remains ~ -0.1 eV below the Fermi level, too far away for having a significant contribution to the CDW hybridisation, and is therefore neglected. In order to simulate a hypothetical $(2 \times 2 \times 2)$ CDW distortion mimicking the lattice instability in bulk $TiSe_2$, the extracted polynomial bands at M and L are backfolded at A and Γ respectively. The crossing points are now spread in energy from ~ -0.18 eV to energies well above the Fermi, a situation that unlikely would lead to any significant electronic energy gain as instead occur for the monolayer. Additionally, a (2×2) reconstruction characterised by the backfolding of the electron pockets from M and L to Γ and A, respectively, would result to an even worse configuration with the crossing points either well below the Fermi level or at too high positive energies. In order to adapt our minimal model to the bulk case the following cosine out-of-plane dispersion is added to the polynomial forms in eq. 4.6:

$$e_c = (e_c(L) - e_c(M))cos(k_z c) + (e_c(L) + e_c(M))/2$$

$$e_h = (e_h(\Gamma) - e_h(A))cos(k_z c) + (e_h(\Gamma) + e_h(A))/2$$

where e_c and e_h are the on-site energies for the CB and VB, respectively. The out-of-plane dispersion used in the calculation is shown Fig. 4.18(b) as extracted by fitting the ARPES data. Turning on the hybridisation using the hamiltonian (4.7), the density of states is reduced at different energies varying with k_z as shown in Fig. 4.18(c) for $\Delta = 42meV$. However, these dips

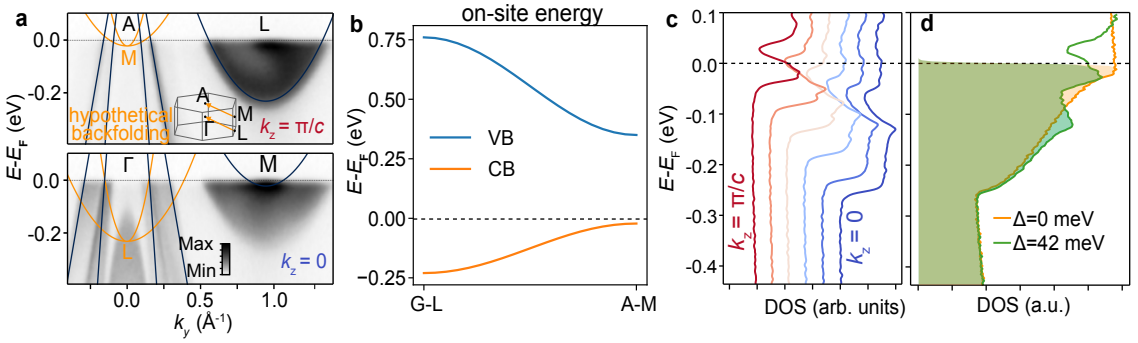

FIGURE 4.18: (a) ARPES measurements ($T = 14$ K) of bulk $TiTe_2$ at $k_z = \pi/c$ ($h\nu = 144$ eV, top) and at $k_z = 0$ ($h\nu = 121$ eV, bottom). The adapted minimal model bare bands are indicated in dark blue. Those are artifically backfolded at A and Γ simulating a hypothetical $(2 \times 2 \times 2)$ CDW phase (orange bands). No such CDW backfolding is observed in the experiment. (b) Valence and backfolded conduction band on-site energy dispersions along k_z considered in the minimal model for bulk $TiTe_2$. (c) DOS at different k_z simulated with $\Delta = 42$ meV revealing the energy spread of the energy gain. (d) The DOS integrated over k_z is only marginally affected by the hybridisation.

in the DOS are smaller than their energy spread along k_z, and they do not completely overlap. The hybridisation is not able to effectively lower the electronic energy as evident in the total DOS calculated integrating over k_z shown in Fig. 4.18(d). However, a weak energy gain is still present in the system even though significantly suppressed compared to the monolayer case.

4.8.1 Band inversion in bulk $TiTe_2$

As unveiled by our minimal model, the CDW hybridisation is also sensitive to the orbital character of the bands. In the discussion above, the orbital character of the valence bands is assumed to be equivalent to the ML compound and independent on k_z. The DFT band structure of bulk $TiTe_2$ reveals, instead, that the large $d - p$ hybridisation in the bulk band structure results in an inversion of the energetic ordering of the p and d derived states along $\Gamma - A$. As shown in Fig .4.19(a), the inner valence band at A cross the non-dispersed d-derived outer valence band at half of the Γ-A path.

Such k_z-dependent band inversion is also observed in other TMDs where it generates interesting electronic states such as bulk Dirac points and topological surface states [18]. As shown in Fig. 4.19(b), this causes the orbital character of the inner and outer valence bands to become inverted between the Γ- and the A-plane. In addition, there are p_z-derived states which were neglected in the monolayer case. In the bulk, they are widely dispersed along k_z and significantly mixed with the p_x states along Γ-M even at energies close to the Fermi level. Since also these states are now at energies comparable to the conduction band minimum, it becomes essential to

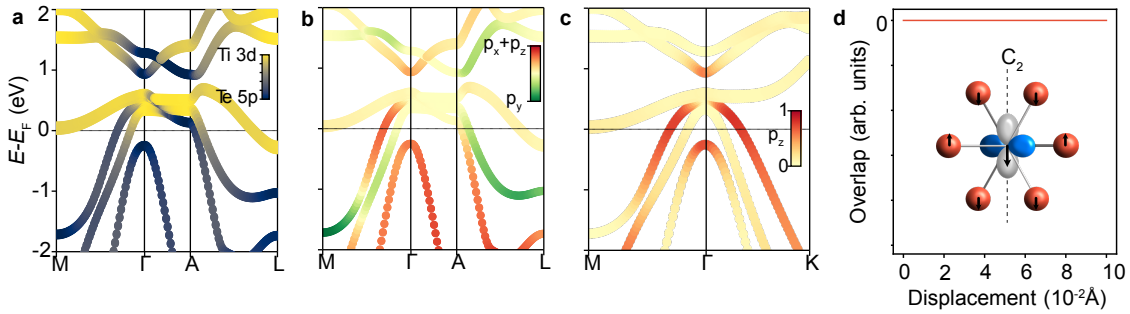

FIGURE 4.19: (a-c) Orbital character of the bulk $TiTe_2$ band structure. (d) Numerically integrated value of $< d_{x'y'}|p_z >$ versus the atomic displacement caused by a A_u phonon mode at M. The Te p_z state in inset is odd in C_2, while the Ti$d_{x'y'}$ has opposite parity, resulting in a zero overlap.

consider their role in the orbital selective hybridisation. In Fig. 4.19(d) the overlap $\langle p_z|d_{x'y'}\rangle$ is calculated as previously done for the other p orbitals in section 4.6. These two states have a different parity with respect to the C_2 axis and therefore their overlap remains zero even when the lattice is distorted. Thus, p_z-derived states do not hybridise with $d_{x'y'}$, and neither with the other two electron pockets as the p_z state also preserves its odd parity with respect to the other two C_2 axis. This is due to the in-plane rotational symmetry of the p_z orbitals, which is also reflected in the isotropic p_z character of the outer valence band at Γ, shown in Fig. 4.19(c). The bulk Hamiltonian 4.7 for our minimal model thus takes the following form when k_z is close to zero:

$$\mathcal{H} = \begin{pmatrix} e_1 & 0 & 0 & 0 & \Delta sin(\theta) \\ 0 & e_2 & 0 & 0 & \Delta sin(\theta - \frac{2\pi}{3}) \\ 0 & 0 & e_3 & 0 & \Delta sin(\theta - \frac{4\pi}{3}) \\ 0 & 0 & 0 & h_{out} & i\lambda_{SO} \\ \Delta sin(\theta) & \Delta sin(\theta - \frac{2\pi}{3}) & \Delta sin(\theta - \frac{4\pi}{3}) & -i\lambda_{SO} & h_{in} \end{pmatrix} \tag{4.12}$$

Since the bands invert each other at roughly halfway through along $\Gamma - A$, for k_z>$\pi/2c$, the monolayer hybridisation scheme (eq. 4.7) is restored, producing the familiar dips in the DOS as shown in Fig. 4.20(b). It is now clear that the orbital texture in bulk $TiTe_2$ is highly unfavourable since the outer valence band remains completely unhybridised for $k_z = 0$, while for $k_z = \pi/c$ the electron pockets become too small, reducing the DOS mainly above the Fermi level. The total DOS shown in Fig. 4.20(c) is only minimally affected by a hybridisation with $\Delta = 42$ meV providing an almost null energy gain. The above results, therefore, show that the out-of-plane band dispersions in bulk $TiTe_2$ and the inverted orbital character of the valence band cooperatively suppress the electronic driving force for a $(2 \times 2 \times 2)$ CDW instability, explaining the unusual thickness-dependence of the CDW tendency in $TiTe_2$.

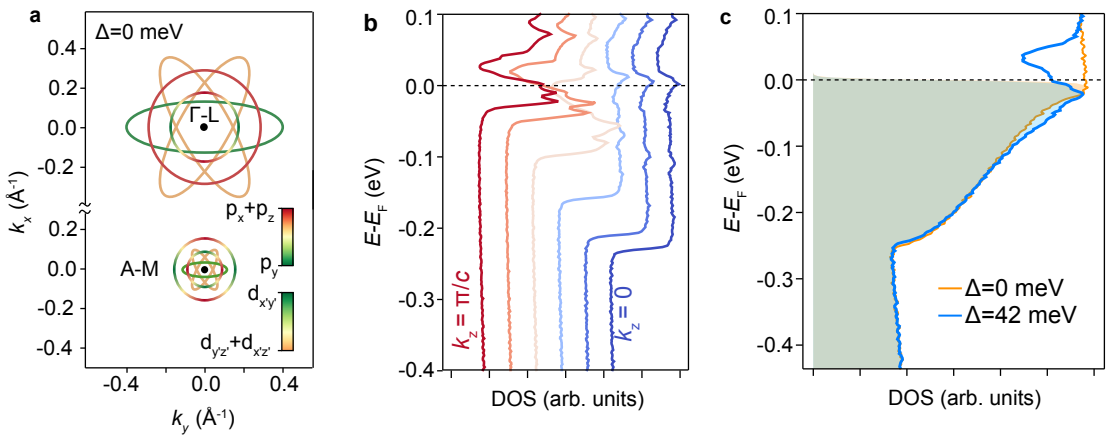

FIGURE 4.20: (a) Unhybridised Fermi surface at $k_z = 0$ and $k_z = \pi/c$ revealing the inverted orbital character of the valence bands. (b) DOS at different k_z simulated with $\Delta = 42$ meV and including the new p_z orbital character in the hybridisation scheme. (c) The DOS integrated over k_z remains almost untouched by the hybridisation, resulting in a complete suppression of the energy gain.

4.9 Conclusion and Outlook

$TiTe_2$ is an extreme example of how a dimensionality of the system can affect collective electronic phases in solids. The work presented in this chapter brings new understanding of such dramatic 2D-3D cross over of the CDW phase in this material. The temperature dependent ARPES measurements reported here reveal for the first time the onset of a clear band hybridization observed in the ordered phase of ML-$TiTe_2$. With the support of both first principles and model calculations I described how the orbital-selective band couplings shape the low-energy electronic structure in this system, and ultimately provide the electronic incentive for the CDW to occur in the first place. Moreover, the minimal model proposed here shows how this energy gain is almost completely suppressed in the bulk due to three-dimensionality in the band structure, including the formation of a k_z-dependent band inversion.

The orbital selection rules are therefore essential in order to describe the CDW phase in this material. Since ML-$TiSe_2$ is also affected by the same lattice instability and has a similar orbital character to the relevant electronic states [40], such orbital selectivity can be considered valid also for the selenide case. To explore this further, I applied the minimal model to simulate the band hybridisation in ML-$TiSe_2$ starting from simple parabolic bare bands extracted from the ARPES spectrum in the normal state from Ref. [39]. As shown in Fig. 4.21(a), our calculation reproduces the splitting of the three conduction bands discussed in chapter 2 with one electron pocket that remains only partially hybridised and still crosses the Fermi level. This hybridisation

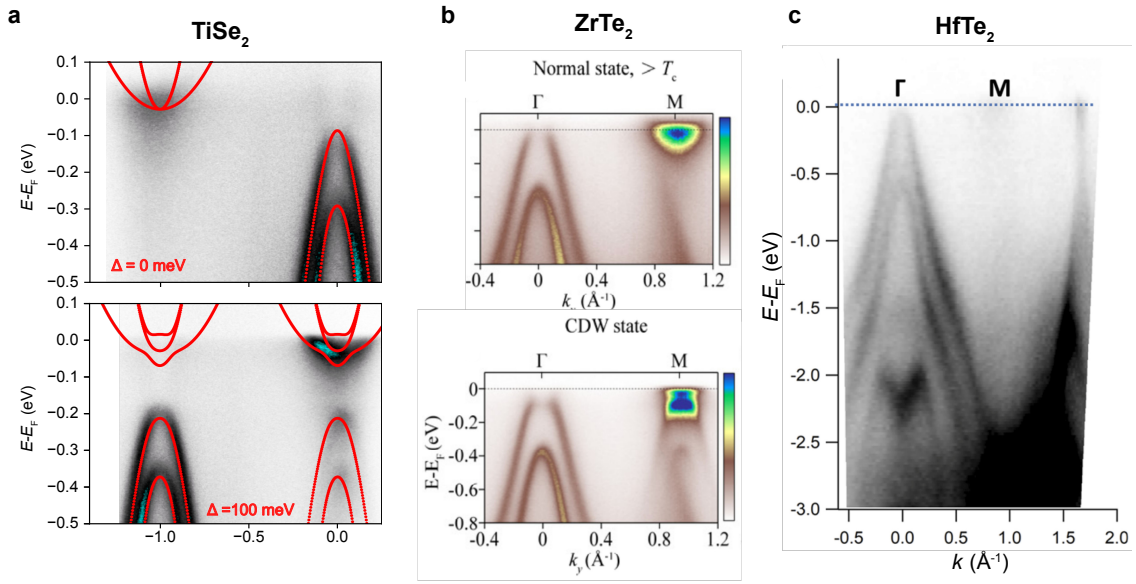

FIGURE 4.21: (a) Minimal model applied to ML-$TiSe_2$ (red line) showing a similar splitting of the bands to the one simulated using the tight-binding method discussed in chapter 2. ARPES data adapted from Ref. [39]. (b) Recently measured band structure of monolayer $ZrTe_2$ along Γ-M in the normal and (2×2) CDW phases, adapted from [99] (c) ARPES spectrum of $HfTe_2$ revealing a quasi zero gap band structure, adapted from [100].

scheme is very similar to that obtained from first-principles calculations [58, 101, 102], but with the benefit here that the band extrema can be located in agreement with experiment, while first principles calculations typically significantly underestimate the band gap. Moreover, the minimal model can be useful to estimate the hybridisation strength Δ directly from experiments. For instance, the calculations for ML-$TiSe_2$ were performed using $\Delta = 0.1$ eV consistent to the value reported in Ref. [39], and much larger than the value extracted for ML-$TiTe_2$. To make a more quantitative analysis, however (for example, to predict T_c), requires additional microscopic information considering, e.g., the details of the electron-phonon coupling strength and the role of possible excitonic correlations. In our model, the Δ is just a mere free parameter representing the effective hybridisation strength between the valence and conduction states and it is not explicitly linked to any specific microscopic driving force. Nonetheless, the putative excitonic condensation in $TiSe_2$ is unlikely to occur in ML-$TiTe_2$, because the large energy overlap between the valence and conduction band and the stronger screening in the semimetal compound is expected to heavily suppress the exciton formation.

Recently, also another IV-group TMD $ZrTe_2$ has been reported to host a (2×2) CDW phase emerging at the 2D limit [99]. In Fig. 4.21(b) the ARPES spectrum of ML-$ZrTe_2$ shows the well recognisable backfolded valence band, which appears below 130 ± 20 K, a critical temperature

not dissimilar to the one reported for ML-$TiTe_2$. In the normal state, the large spin-orbit splitting between the two valence bands indicates that the top of the valence band has a predominant Te $5p$ character and a consequently weaker $d-p$ hybridisation compared to $TiTe_2$. The top of the valence band at Γ is almost aligned in energy with the bottom of the conduction band at M. Indeed, such almost zero-gap alignment of the hole and electron pockets is expected to increase the energy gain induced by the hybridisation. A similar normal phase band alignment has been recently observed in ML-$HfTe_2$ as shown in Fig. 4.21(c). Here the SOC splitting of the valence band is even larger than in ML-$ZrTe_2$, and only a faint tail of the spectral weight related to the conduction band is visible below the Fermi level at M. No lattice instability has been observed yet in this recently synthesised compound, and further studies are needed to verify if it undergoes, or not, a CDW transition at low temperatures. For this purpose, our minimal model would provide a flexible tool that can be applied to the extended material family and explore if the emergence of this controversial ground state follows or not a trend along the periodic table.

Chapter 5

CDW in ML $TiTe_{2x}Se_{2(1-x)}$ alloys

In the previous chapter, the emergence of the controversial CDW phase in ML-$TiTe_2$ has been rationalised in terms of an orbital selective hybridisation between the valence and conduction bands. Such interaction generates an electronic energy gain in the monolayer, which is instead suppressed in the bulk due to the different band structure of the 3D crystal. Rather than changing the dimensionality of the system, another interesting route for manipulating the low energy electronic state consists in chemically substituting the atoms in the material. In the past years, several efforts have been made to synthesise 2D alloys, especially for semiconducting TMDs such as WSe_2 and MoS_2 due to their appealing properties for next-generation electronic and optoelectronic applications [103, 104]. In our case, reducing the energy gap between the valence and conduction bands in ML $TiSe_2$ might alter the band hybridisation at the CDW transition and its microscopic driving force in a way never explored so far. Ti-based dichalcogenides are a versatile platform, in this sense, as they undergo a semiconductor to semimetal transition by chemical substitution of the chalcogenide from Se to Te. In this chapter, the MBE synthesis of 2D $TiTe_{2x}Se_{2(1-x)}$ alloys is discussed as a new route to chemically engineer the CDW instability.

5.1 Controlling the composition by MBE

Multi-element materials are well known to be much more complex to synthesise compared to single element crystals: the increased entropy inevitably leads to a larger number of defects and competitive phases. Alloys are intrinsically disordered systems where the elements are homogeneously mixed together. Only a few studies have been reported so far regarding the growth of homogeneous 1T-$TiTe_{2x}Se_{2(1-x)}$ bulk single crystals [105, 106] using chemical vapour transport. M. May [106] observed a characteristic backfolded valence band at the L point with ARPES in bulk $TiTe_{0.05}Se_{2-0.05}$ at T$=$ 30 K indicating that the CDW phase in $TiSe_2$ is preserved when the

crystal is slightly doped with Te. However, no temperature dependent measurements were performed to estimate the critical temperature, and no other compositions were explored. Chen *et al.* instead attempted the direct selenisation of ML-$TiTe_2$ heating the film up to 330° C in a Se-rich environment. Here, Se substitutes Te starting from the edges of the 2D domains where Te is loosely bound with only one Ti, resulting in an almost pure $TiTe_2$ core surrounded by a $TiSe_2$ lateral shell [107]. The film obtained can hardly be considered an alloy but rather a lateral heterostructure between the two materials. Moreover, to accommodate the strain at the interface generated by the mismatched lattice constant, several misfit holes are introduced, degrading the crystal quality even more. Recently, C. Linderalv *et al.* simulated the thermodynamic stability of several TMD alloys including $TiTe_{2x}Se_{2(1-x)}$ systems using first principles calculations and alloy cluster expansions [108]. From their calculations, a solid solution of the $TiTe_{2x}Se_{2(1-x)}$ can be thermodynamically stabilised at temperatures above 350 K, while below this critical temperature, the alloy separates in domains with different compositions as shown in Fig. 5.1(a). Close to $x = 0.5$, the system is also predicted to assume a Janus crystal structure where the Te and Se layers are alternated in the out-of-plane direction, breaking the inversion symmetry of the lattice.

The challenge of such 2D binary alloy synthesis can be tackled by exploiting the high versatility of our MBE system described in chapter 3 where the growth of high quality pure ML-$TiSe_2$ and ML-$TiTe_2$ on BL-Gr-SiC(0001) has already been optimised by A. Rajan. Depositing Ti on the substrate in a Se and Te mixed partial pressure should provide a suitable synthesis route for $TiTe_{2x}Se_{2(1-x)}$ alloys. The film composition is expected to vary depending on the Se/Te flux ratio used during the MBE process.

First growth trials using a Te/Se flux ratio of 1:1 and 3:1 resulted in almost pure $TiSe_2$ films indicating the higher reactivity of Se compared to Te. In MBE, the atomic flux is usually controlled by changing the temperature of the effusion cell. However, the Se cell temperature required here falls below the stability range of the PID parameters of the Eurotherm controller that adjusts the crucible heater power. Thus, the cell temperature fluctuations are too large, altering the atomic flux during the growth and hence the composition. Our Se cell consists of a crucible where the raw material is evaporated, generating a beam of Se_n molecules that are split in atomic Se by a cracker kept at 500° C. The Se tank and the cracker are separated by a valve (in the following called cracker valve), while a shutter is placed between the cracker and the substrate in order to mask the Se beam before and after the growth. However, this shutter doesn't seal the cell completely from the deposition chamber, and a partial Se beam is introduced in the MBE when the cracker valve is

opened, but the shutter is closed. This suggests an unconventional method to suppress the Se flux by keeping the main shutter always closed during growth but opening only the cracker valve. In this way, the Se cell temperature fluctuations are minimised, improving the control of the Se flux and, consequently, the composition.

As described in Chapter 3, the diffraction pattern of the deposited film can be monitored in real-time during the growth using RHEED, providing information about the lattice constant, which is expected to vary accordingly with the film composition. Fig. 5.1(d) shows the RHEED images of ML-$Te_{2x}Se_{2(1-x)}$ grown on BL-Gr/SiC(0001) substrate, revealing the different reciprocal lattice spacing between the two materials. The diffraction pattern of the alloys is also as sharp as the substrate, suggesting that the quality of the substrate mainly limits the crystal quality of the deposited film. The lattice constant of the alloys spans from 3.54 Å($TiSe_2$) to 3.77 Å($TiTe_2$), producing diffraction patterns with relatively similar spacing. In the inset of Fig. 5.1(b), RHEED pattern horizontal cuts of pure $TiSe_2$ (green) and pure $TiTe_2$ (red) are compared, showing a lattice mismatch of 6.8 $\%$ between the two compounds, thus the RHEED pattern of the deposited alloy will fall within this relatively narrow range. Fitting the RHEED pattern cuts with Lorentzian peaks and a quadratic background, the lattice constant can be estimated with an uncertainty of ± 0.01 Å. Following the so-called Vegard's law, which approximates the lattice parameters of a binary solid solution varying linearly with the composition of the material, a first estimation of the alloy content can be estimated just after the growth. As shown in Fig. 5.1(b), the lattice constant gradually decreases for the alloy samples grown with higher Se temperature *i.e.* flux, demonstrating good control of the chemical composition.

The method reported so far allows to grow 2D $TiTe_{2x}Se_{2(1-x)}$ films with the desired composition but presents some practical limitations. In order to prevent the formation of Se/Te vacancies, TMDs are typically grown in a rich chalcogenide environment. Therefore, the Se and Te effusion cells are equipped with a relatively large crucible filled with enough precursor material for many growths. In order to obtain stable chalcogen fluxes, these effusion cells need to thermalise for a few hours, limiting the machine throughput. To avoid this problem, both Te and Se cell temperatures are kept at constant temperatures, and the Se flux can be tuned by changing the cracker valve opening. This allows a more accurate and faster control on the Se flux, as shown in Fig. 5.1(c). Here, the Se flux is calibrated versus the cracker valve opening waiting only 10 minutes between each point in order to let the chamber pressure restores to its background value.

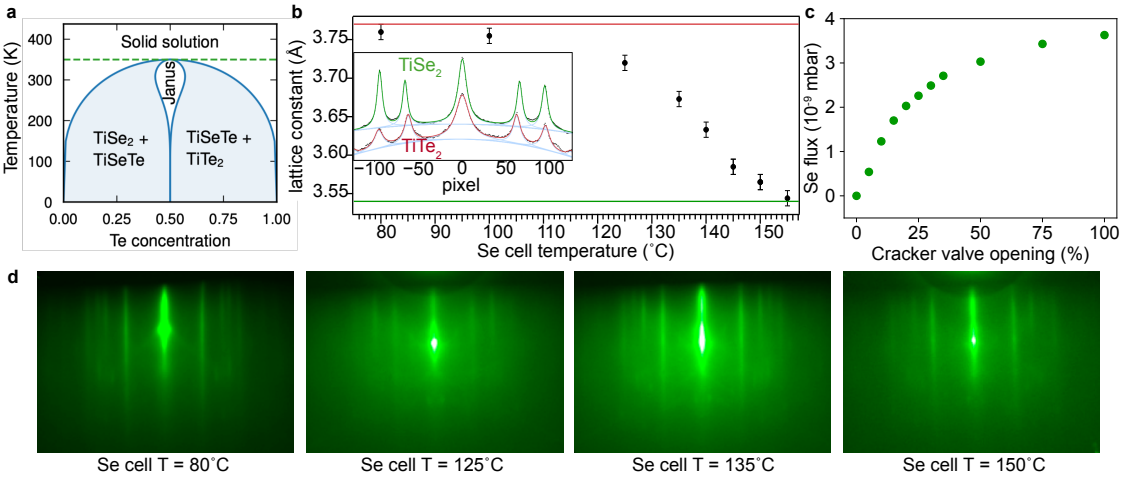

FIGURE 5.1: (a) Phase diagram of 1T-$TiTe_{2x}Se_{2(1-x)}$ reproduced from Ref. [108]. (b) Lattice constant of the monolayer alloy films versus the Se cell temperature. In inset the fitting of RHEED pattern horizontal cuts of pure $TiSe_2$ (green) and pure $TiTe_2$ (red). (c) Se flux measured by changing the Se cracker valve opening. (d) RHEED patterns of the alloy samples grown at different Se cell temperatures.

5.1.1 Chamber conditioning

As discussed in the previous section, the synthesis of 1T-$TiTe_{2x}Se_{2(1-x)}$ alloys requires a superior control of the chalcogenide fluxes compared to the pure selenide and telluride compounds. During the MBE process, only a very small amount of the atoms sticks and crystallises on the substrate, while the majority of the evaporated material is pumped away or condenses on the cold chamber walls. During the deposition, the hot manipulator and the effusion cells warm the chamber slightly, and the coated material can be partially released in vacuum and eventually participates in the growth. Thus, the conditioning of the chamber walls introduces an additional source of material which affects the alloy composition. Moreover, the composition of the chamber coating is hard to control and varies on a daily basis since our MBE system is used to synthesise a wide variety of selenides and tellurides. The effect of the chamber conditioning is not negligible even for the pure selenides/tellurides, as shown in Fig. 5.2(a). Growing pure $TiSe_2$ after a 70 min long growth of pure $TiTe_2$, the lattice constant is shifted toward the telluride (green dots), while the symmetric behaviour occurs for $TiTe_2$ deposited after several minutes of pure selenide growth (red dots). The effect of the chamber conditioning was also tested on the alloy system by growing two films in the same growth condition but with a Te or Se conditioned chamber, resulting in a marked shift in the lattice constant between the two nominally equivalent films (orange and blue dots). The difference in the film composition is also evident by measuring the band structure of the two alloy films with ARPES (Fig. 5.2(b)). The valence band at Γ is clearly shifted at lower energies for the film grown

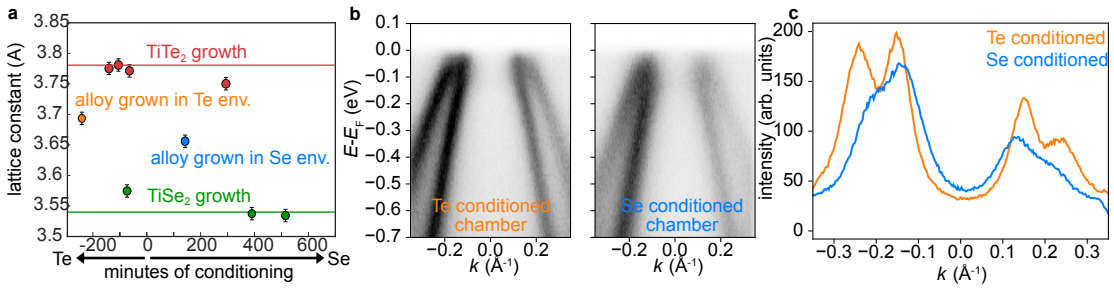

FIGURE 5.2: Effect of the MBE chamber conditioning on the alloy composition: (a) shift in the lattice constant versus the Se/Te conditioning estimated considering the Se or Te evaporation time before the growth. (b) Valence band at Γ of two nominally equivalent samples grown with a different chamber conditioning. (c) MDC at -0.2 eV extracted from the ARPES spectra in (b) revealing the shift in the valence band position.

in a Se conditioned environment, as also captured by comparing MDCs in Fig. 5.2(c) extracted from the two ARPES spectra at -0.2 eV from the Fermi level. Thus, the chamber conditioning has a direct impact on the alloy band structure that needs to be taken into account. A good practice to mitigate such undesired shifts consists in growing a test sample at first. This procedure brings the double advance to have a first estimation of the compositional offset that needs to be compensated in the following growths and to partially condition the chamber environment into a composition closer to the desired alloy.

5.1.2 XPS analysis of alloy content

Having established a suitable synthesis procedure that allows good control of the film composition, it is possible to investigate the electronic structure of the new 2D alloys using photoemission spectroscopy (see Chapter 3 for methods on XPS and ARPES). In Fig. 5.3(a) the peaks in the photo-emission spectra represents the core-level of the elements composing the surface of pure ML-$TiTe_2$ (red) and ML-$TiSe_2$ (green) measured with our *in-situ* XPS after the film deposition. Since the XPS penetration depth is about $5 - 7$ nm and the monolayer film is only ~ 4 Å thick, the spectra are dominated by the C and Si signals from the Gr/SiC(0001) substrate. The Se $3d$ and Te $4d$ peaks from the TMD films at $E - E_F$ = -50 and -40 eV, respectively, are weaker due to low surface coverage. Although both these peaks are expected to be split by spin orbit coupling in two components $d_{1/2}$ and $d_{3/2}$, these latter are not completely resolved in our measurements resulting in a convoluted asymmetric peak. The pure $TiSe_2$ spectrum also shows several other peaks consistent with the extensive LMM Auger structure of Se [109]. Instead, no core level of Ti was detected. Also, the synchrotron data discussed in chapter 3 shows only a faint peak related to the transition metal, whose intensity is probably suppressed by geometrical effect due

to the specific configuration of the experimental set-up. Nonetheless, the presence of Ti in our sample is proved by the lattice constant and the band structure measured with ARPES consistent with pure $TiSe_2$, $TiTe_2$ and related alloys. In Fig. 5.3(b), the XPS spectra of ML Ti-Se-Te alloy films show the gradual rise of the Te $4d$ peak accompanied by the decrease of the Se intensity as expected when the Te content is increased. Since the pure $TiTe_2$ sample in this growth run was deposited in a Se conditioned chamber, some residual Se is still present in the film, consistent with its slightly smaller lattice constant (3.768 ± 0.01 Å) compared to the value reported in the literature (3.777 ± 0.003 Å for the bulk compound [105]).

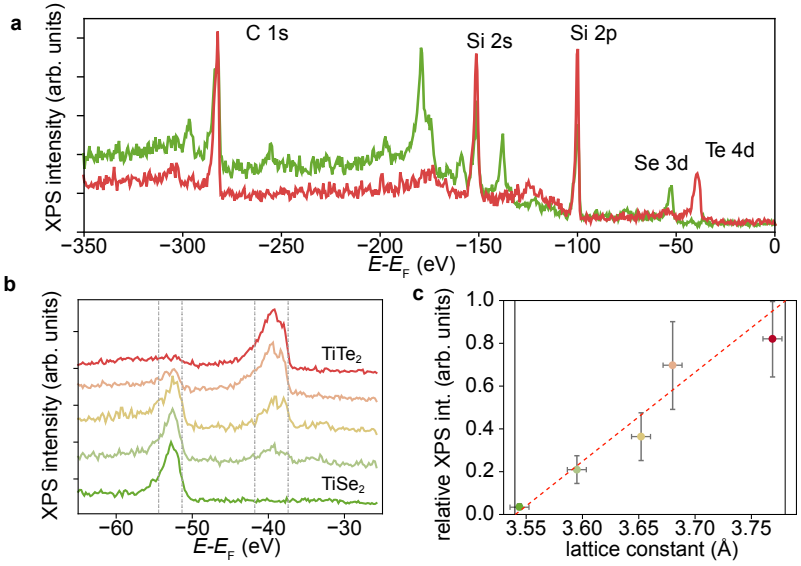

FIGURE 5.3: (a) XPS spectra of pure ML-$TiSe_2$ (green) and ML-$TiTe_2$ (red) on BL-Gr/SiC(0001). (b) Intensity evolution of the Se $3d$ and Te $4d$ peaks at different alloy contents. (c) Chemical composition extracted from the XPS data versus the alloy lattice constant.

The alloy content can be estimated by calculating the relative intensity between the Se and Te peaks normalised over their respective cross sections (0.0314 Mbarn for Se $3d$ and 0.04979 Mbarn for Te $4d$). A Shirley background was subtracted from each spectrum, and the peak intensity was numerically extracted integrating the curve within a range of $\sim 1FWHM$ of the peak in order to avoid spurious components from materials on the sample holder. Indeed, the X-ray beam spot is slightly larger than the sample and part of the signal measured by the hemispherical analyser might come from the flagstyle plate. The resulting Se/Te XPS relative intensity is plotted in Fig. 5.3(c) versus the lattice constant extracted from the RHEED pattern. The uncertainty of the intensity was estimated by considering the difference between the area evaluated integrating over the range indicated by the grey dashed lines and the wider integration range from -65 eV to -50 eV for Se

and -35 eV to -50 eV for Te. Our experimental data are consistent with the Vegard's approximation of a linear dependence between the lattice constant and the alloy content, which allows us to take the former as a measure of the film composition.

5.2 Film inhomogeneity

In this section, examples of strong inhomogeneity observed in some of the alloy samples are reported. As previously discussed, the film composition is assessed mainly by extracting the lattice constant from the RHEED pattern measured just after the growth. Due to its grazing angle geometry, the area under the electron beam spot is elongated in the direction of the beam covering the entire sample width. An inhomogeneous alloy composition is expected to increase the RHEED streaks broadening resulting from the superposition of all the different domain contributions. As visible in Fig 5.1(b), the RHEED linewidth of the grown film is similar to the substrate one, meaning that the deposited crystal quality is limited by the substrate quality rather than the MBE process itself. Unfortunately, the substrate quality might vary significantly between different samples, complicating a systematic comparison of the RHEED linewidth. Also, the XPS analysis performed with our lab equipment is an averaged measurement of the sample chemical composition since the X-ray spot size has the same dimension of the sample.

Taking advantage of the ~ 100 μm spot size of the CASSIOPEE end station at the SOLEIL synchrotron, a more local investigation of the sample composition was performed using ARPES and XPS. As the other samples were measured *ex-situ*, the films shown here were previously capped with a double Te and Se capping layer that was removed at the CASSIOPEE end-station before the measurements following the method described in chapter 3. In Fig 5.4(a), the XPS spectrum acquired close to the edge of the sample shows a predominant Te content ($x = 0.66$), in agreement with the semimetallic band dispersion measured with ARPES on the same spot as shown in Fig. 5.4(b). At the centre of the sample, instead, a domain with a predominant Se content is detected by XPS and ARPES, showing a band dispersion very similar to the pure ML-$TiSe_2$. Moreover, the characteristic backfolding of the valence band (signature of the (2×2) CDW phase) is present below the conduction band at M. The Te content in this part of the sample ($x = 0.14$ from XPS) is close to the composition $x = 0.15$ estimated with RHEED (lattice constant $= 3.577 \pm 0.01$Å), which suggests that the majority of the sample has this lower Te content and only the sample edges show a different composition. However, a smaller compositional variation on a

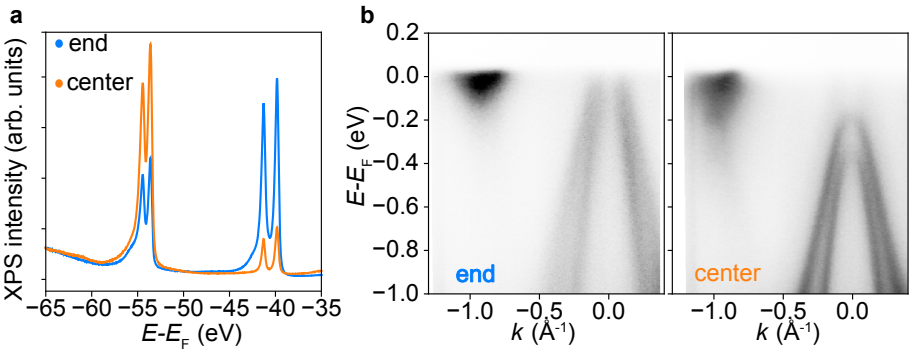

FIGURE 5.4: XPS (a) and ARPES along Γ - M path (b) measured at the edge and at the center of a decapped sample, showing a significant change in the alloy composition.

few μm scale cannot be excluded and might generate the broadening of the valence band skewed towards higher energies visible in the ARPES spectrum measured at the centre of the sample.

Another possible source of defects is the prolonged exposure of the film to the electron beam during the RHEED measurement. A test sample was grown as normal by blanking the RHEED beam for the first 50 minutes, resulting in a weak diffraction pattern of the alloy with a lattice constant of $= 3.557 \pm 0.01$Å. Then, the sample was left growing but exposed to the RHEED beam for 30 min, as indicated by the green area in Fig. 5.5(a), resulting in a smaller lattice constant. High energy electrons are expected to have a high chemical reducing power that is expected to lower the oxidation state of the transition metal by forming chalcogenide vacancies, consistent with the smaller lattice constant observed here. After having blanked the electron beam again, the growth continued, and the lattice constant slowly recovered, suggesting the formation of a film with lower Te content. Indeed, the ARPES spectrum in Fig. 5.5(b) measured after the growth shows an almost pure ML-$TiSe_2$ band structure in the CDW phase, but with an additional huge electron pocket at M induced by the interaction with the high energy electrons. Interestingly the damaged domain is not healed by the successive growth, leaving on the sample surface two distinct doped and undoped domains. Therefore, prolonged exposure to the high energy electron used to measure the diffraction pattern during the growth changes the sample composition as well as its lattice constant. Apart from this specific sample, the other films reported in this chapter were minimally exposed to the RHEED beam as their diffraction patterns are acquired rapidly in only a few seconds and typically just before and after the growth.

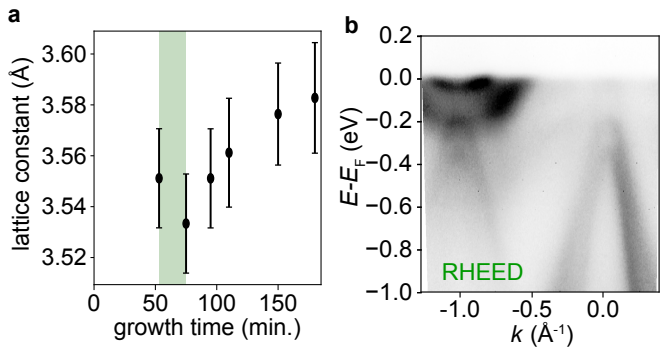

FIGURE 5.5: (a) Lattice constant shift observed for a sample exposed to the RHEED beam during the growth. The green area represents the exposure time. (b) Effect induced by the high energy electron beam on the band structure measured with ARPES at T= 20 K after the growth of the sample in (a).

5.3 Normal phase band structure vs. alloy content

The low energy electronic structure of the as-grown $TiTe_{2x}Se_{2(1-x)}$ is measured *in-situ* with our ARPES system connected to the MBE chamber. In Fig. 5.6 the dispersion of the hole and the electron pocket at Γ and M appears without any CDW backfolded valence band at temperatures close to RT. Only for pure $TiSe_2$ a weak spectral weight is visible below the electron pocket as a precursor of the lattice instability induced by the strong CDW coupling in this material, as discussed in chapter 2. The ARPES spectrum of the alloys is overall broader than the pure limit materials due to their intrinsic disorder or slightly inhomogeneous film composition. Increasing the Te content, the band minimum is pushed to lower energies, while the valence band at Γ approaches and crosses the Fermi level for composition slightly larger than $x = 0.12$. Including even more Te in the system, also the outer valence band top reaches positive energies for x > 0.4. The valence and conduction pockets continue to enlarge, compensating the number of electrons and holes until Se is completely substituted with Te.

A first estimation of the indirect gap amplitude can be extracted from the ARPES spectra by fitting the two valence and the conduction bands with parabolic dispersions as shown for $TiSe_2$ and $TiTe_2$ in Fig. 5.7. As previously noted in chapter 4, the hole bands of ML-$TiTe_2$ are highly non parabolic and are better approximated using a function derived by the $k \cdot p$ model. However, a simpler second order polynomial is preferred here in order to minimise the number of free parameters varying between the alloy series. This approach might lead to an overestimate of the valence band top energy position for compositions close to pure $TiTe_2$, and therefore of the indirect energy overlap between the hole and electron pockets, too. Nevertheless, an overall good match

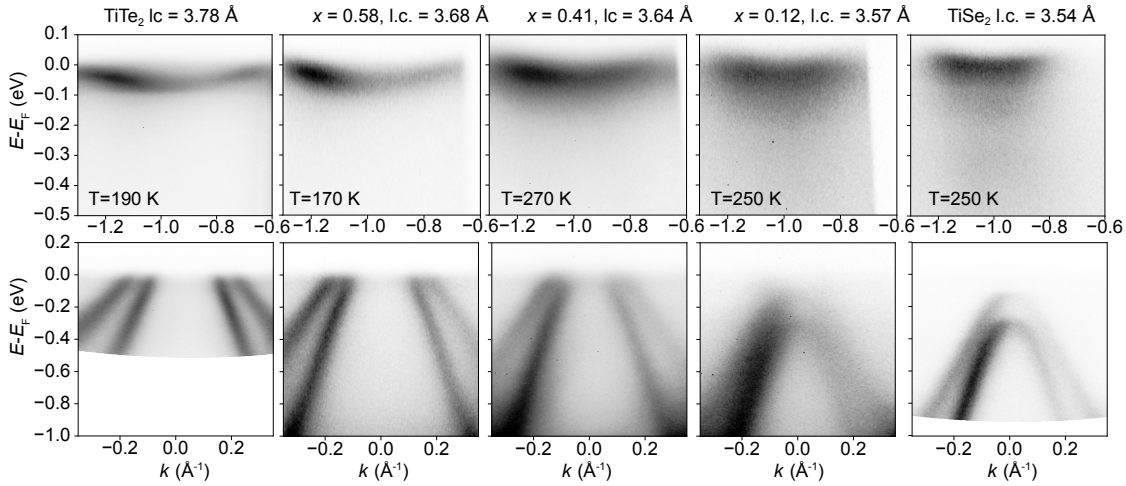

FIGURE 5.6: Band structure of ML-$TiTe_{2x}Se_{2(1-x)}$ in the normal phase at different composition (x) and lattice constant (l.c.) measured with $in-situ$ ARPES ($h\nu = 21.1$ eV).

with the ARPES data is obtained in the region of interest above -0.2 eV where the band crossing is expected to happen in the CDW phase. The energy gap monotonically decreases from ~ 0.08 eV in the selenide to ~ -0.46 eV in the telluride. The band extrema extracted from the alloys are well represented, approximating a linear variation of the valence band top and conduction band bottom with the composition x.

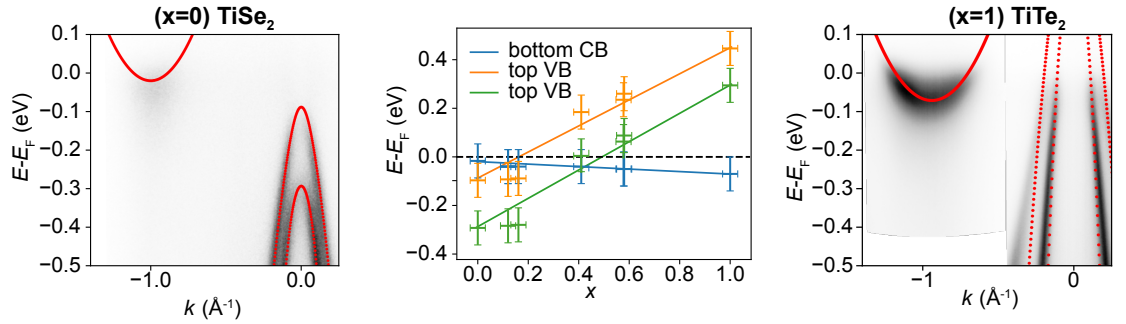

FIGURE 5.7: Fitting the normal state ARPES dispersion with parabolas (shown for pure ML-$TiSe_2$ and pure ML-$TiTe_2$) allows a first estimation of how the energy position of the conduction band (CB) bottom and the two valence band (VB) maxima varies across the alloy series.

5.4 CDW in $TiTe_{2x}Se_{2(1-x)}$

The ARPES measurement shown in the previous section reveals the manipulation of the normal phase band gap in the ML-$TiTe_{2x}Se_{2(1-x)}$ system achieved by tuning the alloy composition. The realisation of a such smooth transition from semiconductor ($x = 0$) to semimetal ($x = 1$) makes this 2D material a remarkable platform for studying quantum phase transitions and how

they are affected by the low energy band structure. The increased number of free charge carriers at the Fermi level is also expected to largely enhance the electronic screening environment inside the 2D crystal, which might have a direct impact on the electron-phonon and, in particular, electron-hole interaction.

The ARPES spectra measured at cryogenic temperatures for the same samples discussed in the previous section are reported in Fig. 5.8. Here, the characteristic replica valence band appears at the M point not only for the pure selenide and telluride samples but also at all the intermediate compositions, meaning the (2×2) CDW instability is preserved across the alloy series. The lattice distortion double the unit cell making Γ and M equivalent reciprocal space points and allowing the interaction between the conduction and the valence band. The hybridisation reshapes the band dispersions accordingly with their relative energy position in the normal state, which in turn is dictated by the alloy composition. Similar to the pure selenide case, the valence band top is pushed to lower energies in the CDW phase for $x = 0.12$, enhancing the indirect band gap in the ordered phase. However, an anomalous spectral weight with a triangular-like shape appears in between the gap at M connecting the two bands, while only a weak shadow above the valence band top is visible at Γ. Such peculiar features might be induced by the complex interplay between the CDW interaction and the intrinsic disorder in the alloy system.

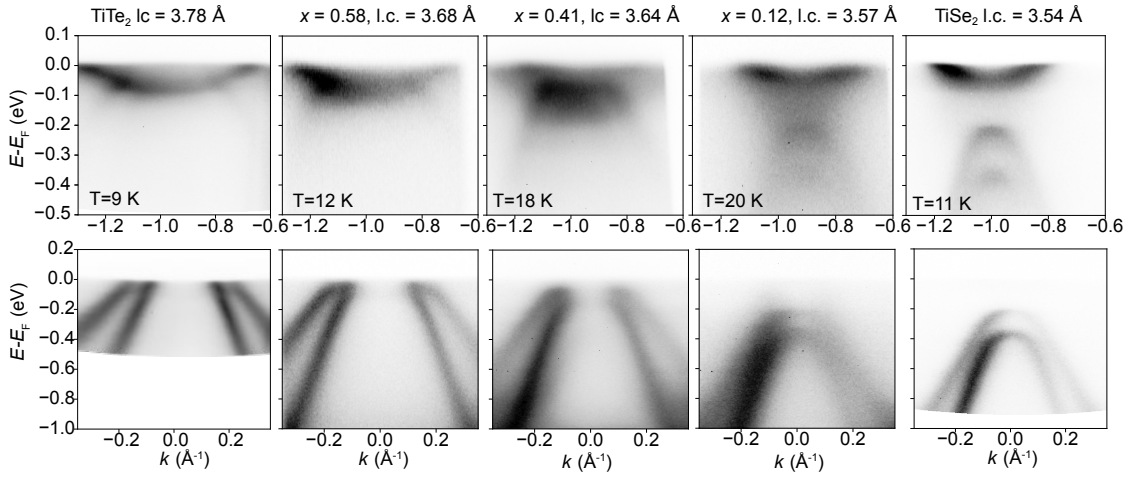

FIGURE 5.8: ARPES spectrum at M (top) and Γ (bottom) of the same samples of Fig. 5.6 cooled to low temperatures. All the samples show the valence band backfolding at M characteristic of the (2×2) CDW phase.

Increasing the Te content to $x = 0.41$, the conduction band acquires a remarkable discontinuous dispersion due to the CDW gap opening at the crossing points between the backfolded outer valence band and the electron pockets, resulting in an almost flat dispersion around M. Also the

inner valence band top that was just above the Fermi level in the normal state is now observed just below the flat spectral weight at M, assuming a parabolic-like dispersion. At Γ, the intensity of the valence bands is significantly suppressed at their top, but clear signatures of hybridisation are well recognisable. For instance, the outer valence band spectral weight doesn't intersect the Fermi level anymore and strongly flattens, mimicking the quasi dispersionless spectral weight at M. A similar effect is also visible at the inner valence band top, although its dispersion is more pronounced than the outer pocket. The intensity suppression at the BZ centre can be ascribed to the strong mixing with the backfolded Ti $3d$-derived states, which are much less intense at Γ as noticed also for pure $TiSe_2$ and $TiTe_2$.

Increasing even more the Te content, the bands significantly overlap in energy, and the backfolding at M becomes weaker assuming a shape more similar to the pure $TiTe_2$ case. The signature of the CDW interaction is still clearly visible at Γ as shown in a close comparison between the normal and CDW phase ARPES spectra of the valence band for another sample with $x = 0.58$ in Fig. 5.9(a). At low temperatures, both the valence bands flatten under the effects of the hybridisation, as illustrated by the dashed lines. A weak spectral weight is also visible in between the inner valence band, mimicking the faint backfolded conduction band signal identified in the ARPES spectrum of ML-$TiTe_2$ reported in the previous chapter. EDCs extracted at $k = 0$ for the high and low temperature spectra show the energy profile of this signal disappearing in the normal phase and leaving behind a second component closer to the Fermi level at 245 K (Fig. 5.9(b)). This high temperature feature was also observed in ML-$TiTe_2$ (Fig. 4.5) and was associated to some possible impurity localised states since it was almost temperature-independent. In the alloy presented here instead, the intensity of this second component is significantly suppressed at T = 7 K. Such temperature dependence might suggest this component could be generated by the spectral weight tail of the inner valence band top, which starts appearing below $E = 0$ eV at high temperatures when the spectral broadening is large.

5.4.1 T-dependent ARPES for $x = 0.58$

Systematic T-dependent ARPES measurements were performed on this sample in our lab to estimate the critical temperature of its CDW transition. As shown in Fig. 5.10, the backfolded valence band at M gradually disappears with warming up following the vanishing of the order parameter *i.e.* the (2×2) CDW amplitude.

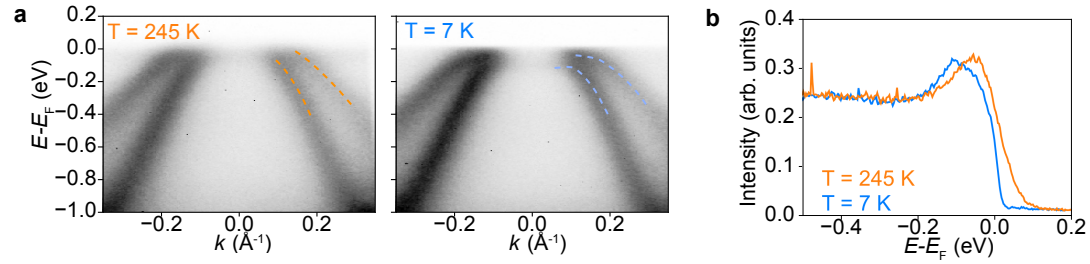

FIGURE 5.9: (a) Changes in the valence band ARPES spectrum at Γ above and below T_c for a sample with $x = 0.58$. The dashed line in both spectra are a guide to the eye, highlighting the effects of the hybridisation in the low temperature phase. (b) EDCs at $k = 0$ reveals the disappearing of the backfolded conduction band at 245 K.

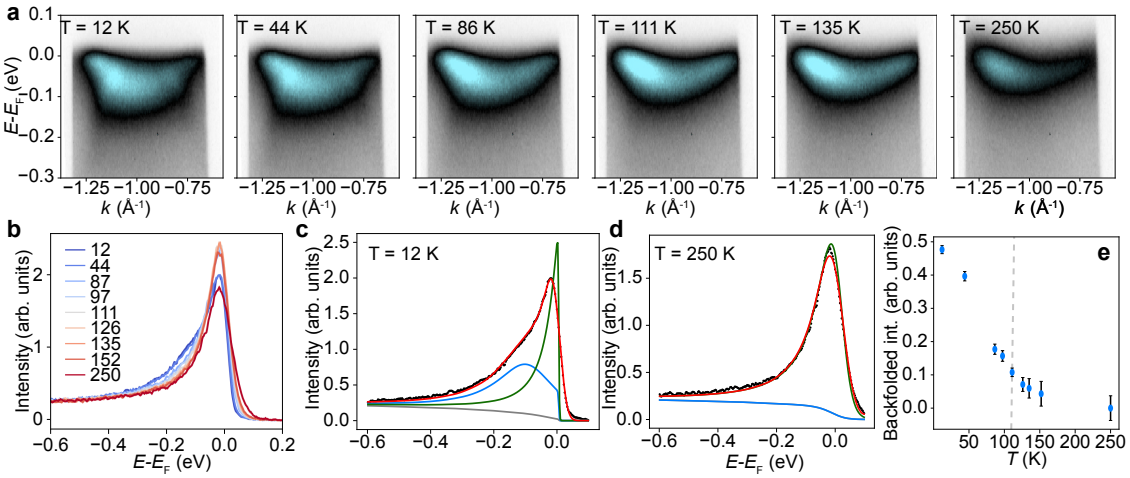

FIGURE 5.10: (a) T-dependent ARPES measurement for $TiTe_{2x}Se_{2(1-x)}$ with $x = 0.58$ at M ($h\nu = 21.1$ eV). (b) EDCs extracted at $k = -1.2$Å^{-1} for different temperature used to extract the backfolded spectral weight represented by the blue peak component in (c). (c-d) Example of fitting of the EDCs at 7 K and 250 K, where the green components represent the conduction band intensity. (e) p1 amplitude vs temperature revealing the intensity suppression of the backfolded spectral weight.

For pure ML-$TiTe_2$, the backfolded intensity was extracted by fitting MDCs below the conduction band minimum. However, here the signal to noise ratio is not as high as for synchrotron measurements, and the backfolded intensity quickly becomes part of the background making it difficult to follow its energy dispersion. Another possible way is to take EDCs at $k = -1.2$Å^{-1} where the distribution curves show a long asymmetric tail due to the presence of the replica bands below the electron pocket as shown in Fig. 5.10 (b). The two components are deconvolved by fitting the curve using two Lorentzian peaks and a Shirley background. A Fermi function and a Gaussian convolution with standard deviation = 17 meV are also considered. The position and the $FWHM$ of the blue peak representing the backfolded intensity were kept constant for all the temperatures. Although the backfolded weight is expected to broaden due to the smaller correlation lengths at the transition, the constraint on its width is necessary in order to avoid unphysical

results during the fitting. The intensity of the backfolded spectral weight is plotted in Fig. 5.10(e), showing the gradual suppression of the CDW order similar to what was observed in pure $TiTe_2$. Since the intensity values above 111 K can be considered statistically equivalent, this temperature is taken as the best estimate for Tc. The chemical substitution of Te with Se up to $x = 0.58$, therefore, doesn't appear to significantly affect the CDW transition, which occurs at a critical temperature similar to the one reported for pure $TiTe_2$.

5.4.2 T-dependent ARPES for $x = 0.12$

In this section, the band structure evolution across the CDW transition is analysed for a sample at the other end of the alloy series ($x = 0.12$), close to where the zero gap transition is expected to occur in the normal phase. The ARPES spectra reported here were measured at SOLEIL synchrotron with the support of Chiara Bigi, Anđela Zivanovic and the beamline scientist Patrick Le Fevre. The sample was grown with MBE using the method described in section 5.1 and capped with a first Te and a second Se capping layer in order to prevent the oxidation of the film during the transport. The protective layer was then decapped *in-situ* heating the sample up to $T \sim 270°C$ for one hour (see chapter 3 for the capping and decapping methods).

Fig. 5.11(a) shows the ARPES spectrum using a photon energy of $h\nu = 45$ eV, which allows to measure simultaneously the bands at Γ and M. The pristine 2D alloy surface is restored after the decap showing the appearing of the replica bands at M. However, the backfolded spectral weight is relatively blurred and mixed with the long tail of the conduction band suggesting a degraded crystal quality compared to a similar sample measured *in-situ* just after growth (see Fig. 5.8). This fact is also reflected in the long shadow of the valence band at Γ, whose spectral weight is largely skewed toward higher energy suggesting a non-uniform composition. For such reason, it is hard to determine the critical temperature by extracting the backfolded intensity as done for the pure selenide case. An alternative approach consists in tracking the position of the valence band maxima at Γ, which is modulated across the phase transition by the interaction with the conduction band. Despite the substantial suppression of the intensity at the top of the bands, two peaks are clearly revolved in the EDCs at $k = 0$ shown in Fig. 5.11(b), revealing the movement in energy of the two hole pocket tops as the CDW hybridisation is weakened at higher temperatures. The peak positions were extracted at each temperature by fitting the curves using two Lorentzians plus a Shirley background multiplied by a Fermi distribution and convoluted with a Gaussian with a standard deviation of 20 meV determined by fitting the Fermi edge in the low temperature data

as shown in Fig. 5.11(c-d). The temperature evolution in energy of the outer (green) and inner (blue) valence band maxima is plotted in Fig. 5.11(e), revealing a shift of $\sim$ 60 meV for both bands. Since the inner valence band is further away from the conduction band, its energy position saturates earlier in temperature compared to the outer valence band, similarly to what was also observed in ML-$TiSe_2$ [39]. In the pure selenide, the valence band energy shift is slightly larger ($\sim$ 80 meV), suggesting a weaker CDW ordering in this alloy film. Moreover, the inner and outer valence band position saturates respectively at T above $\sim$ 210 K and $\sim$ 230 K in ML-$TiSe_2$, while in the slightly Te doped sample reported here, this occurs only at $\sim$ 160 K and $\sim$ 180 K. Thus, substituting a relatively small percentage of chalcogenide in $TiSe_2$ with Te provokes a significant shift in the CDW critical temperature.

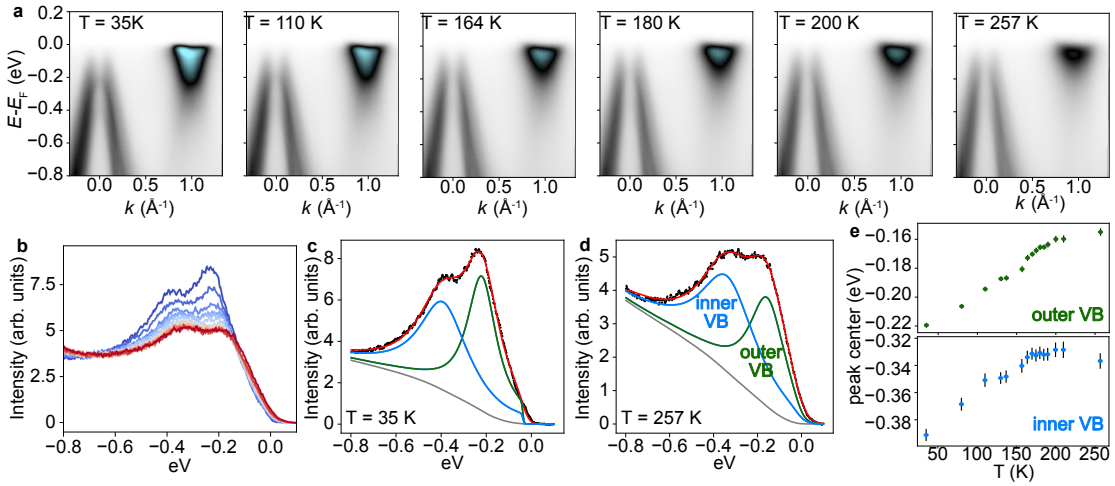

FIGURE 5.11: (a) T-dependent ARPES measurement for $TiTe_{2x}Se_{2(1-x)}$ with $x = 0.12$ ($h\nu = 45$ eV). (b) EDCs extracted at $k = 0$Å^{-1} for different temperatures used in the fitting in order to extract the backfolded spectral weight represented by the blue peak component in (c). (c-d) Example of fitting of the EDCs at 35 K and 257 K with two components representing the inner and outer valence band maxima. (e) Peak position extracted from the fitting revealing the shift in energy of the outer and inner valence band top due to the hybridisation in the CDW phase emerging below $T_c = 170$K.

5.5 CDW phase diagram of ML-$TiTe_{2x}Se_{2(1-x)}$

The temperature dependent ARPES measurement discussed so far and others performed on similar samples are summarised in a phase diagram showing how T_{CDW} varies across the alloy series (Fig.5.12). The critical temperature drops relatively quickly as soon as Te is substituted in the selenide 2D crystal. Similar fast suppression of the CDW order was reported in pure $TiSe_2$ samples $n-$doped with Se vacancies [39] associated with the increased electron pocket size and leading to complete destruction of the lattice instability already for $TiSe_{1.94}$. In our case, the

chemical substitution of Se with an element having an equivalent oxidation state (Te) is expected to have a milder effect on the doping level and, in turn, on the transition temperature, in agreement with the partial suppression of the CDW instability observed in our experiment. The critical temperature might be attenuated by the intrinsic disorder present in the alloy which is expected to limit the coherence of the CDW ordering and thus ease its melting induced by the thermal fluctuations. However, such a disorder effect does not seem to affect the other end of the series at $x \sim 1$. Here T_{CDW} seems to remain almost constant at least down to $x = 0.58$, although more measurements are needed to confirm this plateau in the phase diagram. Therefore, the modulation of T_{CDW} seems rather to follow the semimetal to semiconductor transition occurring at compositions close to pure $TiSe_2$, pointing to the successful tuning of the CDW interaction induced by variations in the low energy band structure in Ti-based dichalcogenides.

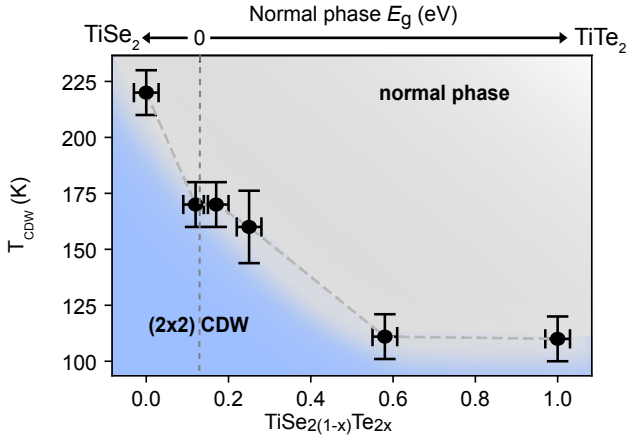

FIGURE 5.12: Proposed phase diagram of ML-$TiTe_{2x}Se_{2(1-x)}$ showing the suppression of the CDW phase close to the pure selenide composition and the plateau for $x > 0.58$.

5.6 Minimal model across the alloy series

As reported in the previous sections of this chapter, the band gap engineering in $TiTe_{2x}Se_{2(1-x)}$ is achieved experimentally by combining the synthesis of new 2D alloy films by MBE and the measurement of their band dispersions with ARPES. The backfolding of the valence band to M is observed for all the compositions explored so far, pointing to the emergence of the same (2×2) CDW phase discussed in chapters 2 and 4 for pure ML-$TiSe_2$ and $TiTe_2$ respectively. Such lattice instability is characterised by the softening of three equivalent A_u phonon modes whose symmetry induces important orbital constraints in the coupling between the valence and conduction

bands. Using the same Hamiltonian-based model developed for ML-$TiTe_2$ in chapter 4, such orbital selective hybridisation can be simulated across the alloy series bringing useful insight for understanding the band structure modification induced by the CDW transition.

The parabolic bands extracted in section 5.3 provide a suitable basis to apply the Hamiltonian in eq. 4.7 describing how the CDW coupling mixes the three electron pockets backfolded at Γ with the two hole bands. In Fig. 5.13(a-c), a hybridisation strength Δ of 42 meV is applied for both the end series compounds showing the mix of the conduction (yellow) and valence (blue) states and the related changes in their total DOS. For $TiSe_2$, the CDW interaction enlarges the full gap already present in the normal phase, pointing to an effective lowering of the total electronic energy. In the real material, the CDW hybridisation is much stronger ($\Delta = 100$ meV) leading to a larger energy gain. Here a reduced coupling that matches the value extracted for the telluride is instead useful to have a systematic comparison with the other alloy members. In the semimetallic compound $TiTe_2$, the hybridised DOS never reaches zero value. Still, a substantial dip just below the Fermi level is developed, providing the electronic energy gain stabilising the CDW phase.

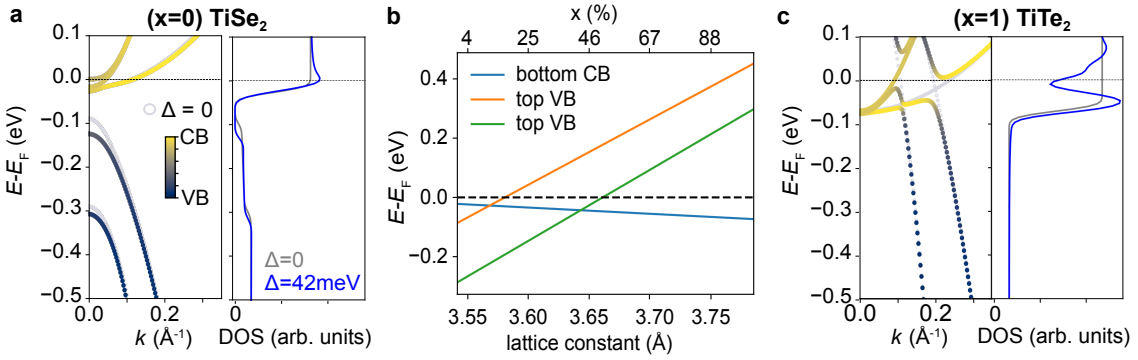

FIGURE 5.13: ML-$TiSe_2$ (a) ML-$TiTe_2$ (c) band structure along $\Gamma - M$ fitted with parabolic dispersion and their simulated DOS. (b) Energy variation of the conduction band (CB) and valence band (VB) extrema in $TiTe_{2x}Se_{2(1-x)}$ calculated following a linear interpolation of the values extracted from the two end series compounds shown in (a) and (c).

The band structure of ML-$TiTe_{2x}Se_{2(1-x)}$ at different compositions can now be extracted by approximating a linear dependence of the parabolic band parameters. As discussed in section 5.3 this assumption is consistent with ARPES measurements performed on films grown with MBE. Fig 5.13(b) shows the trend for the band extrema considered in our model, revealing the energy cross-over between the conduction band and the outer valence band for $x \sim 0.16$ (lattice constant of ~ 3.58Å) that marks the semiconductor to semimetal transition in the normal phase. A second relevant crossing occurs instead with the inner valence band at $x \sim 0.42$ (lattice constant $\sim$

3.64Å), slightly before the half composition. Applying an interaction strength of $\Delta = 42meV$ constant for all the compositions, the band structure of the alloy system in the CDW phase is simulated as shown in Fig. 5.14(a).

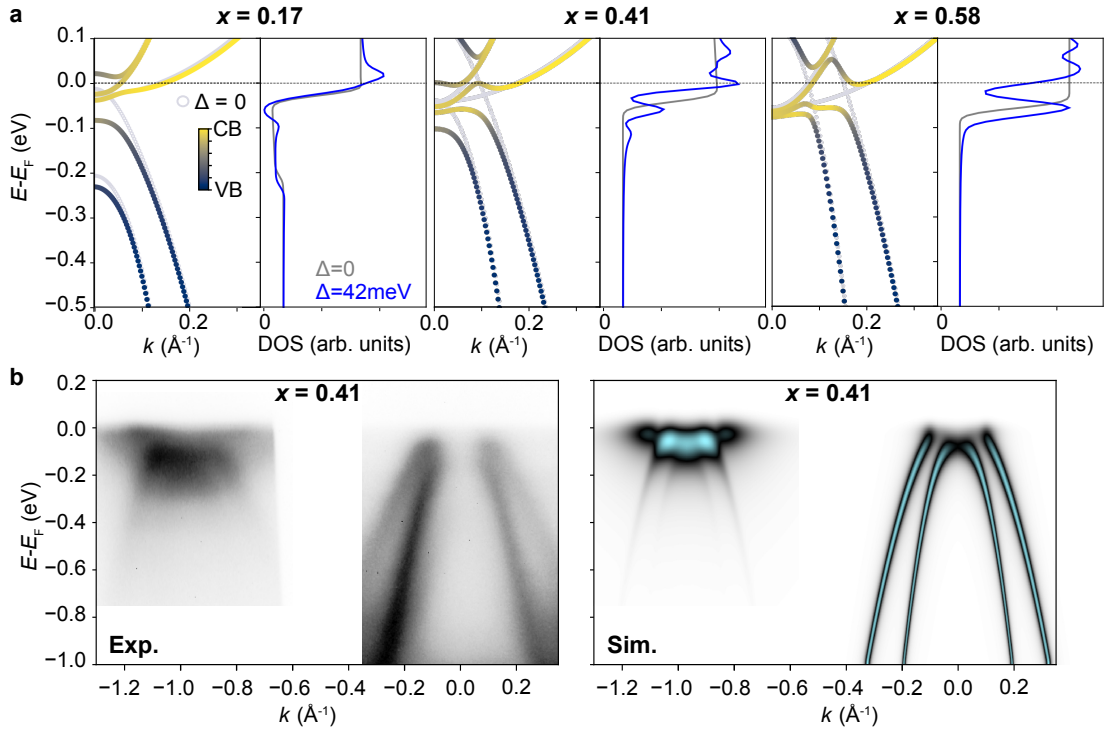

FIGURE 5.14: (a) Minimal model band dispersion and DOS for the normal ($\Delta = 0$ and hybridised phases ($\Delta = 42$ meV) calculated for different compositions. (b) Experimental and simulated ARPES spectra of a sample with $x = 0.41$.

For slightly Te-doped films, the valence band starts approaching the electron pockets promoting a stronger mixing between these states. At $x = 0.17$, the normal phase band gap is closed, but the hybridisation is able to re-open it in the CDW state, as visible also in the total DOS plot. Introducing even more Te in the system, the energy overlap between the original states increases, and the hybridisation is not strong enough to separate the bands completely but generates an almost flat dispersion at the top of the outer valence band that acquires a significant Ti $3d$ character. Such effects are also experimentally observed in the film with composition $x = 0.41$ here reported in Fig. 5.14(b). From the bare band calculated with the minimal model, the ARPES spectrum for such composition is simulated, replicating the same flat spectral weight just below the Fermi level at M and the tails of the backfolded valence bands that vanish at lower energies as they lose Ti character. Also at Γ the simulated valence bands mimic the flattening of the hole bands and the suppressed spectral weight at the BZ centre, although this effect is much more pronounced in the experimental data due to the matrix element effect that is not included in the ARPES calculation

reported here. However, the measurements show the flat spectral weight at higher binding energies suggesting a stronger hybridisation than the one assumed for the simulation, which is held to the value estimated for pure ML-$TiTe_2$. Such putative enhancement of the CDW coupling at this composition might be consistent with the phase diagram proposed in Fig. 5.12, where T_{CDW} at $x = 0.41$ is predicted to grow from the plateau observed for $x > 0.58$. Further minimal model calculations were performed within this latter compositional range. At $x = 0.7$, the crossing points move far away from Γ and in turn from the band extrema, resulting in a situation similar to pure $TiTe_2$ as also observed experimentally with ARPES (Fig 5.8).

5.7 Energy gain in the alloy series

Analysing in more detail how the DOS is affected by the hybridisation tells us if an effective electronic energy gain enables the energetic stabilisation of the CDW phase. As discussed in detail in Chapter 4, a partial gap in the DOS of pure ML-$TiTe_2$ is opened for $\Delta \neq 0$ eV, redistributing the electrons just below the Fermi level towards lower energies. From the simulation concerning $TiSe_2$ in Fig. 5.13 where I applied the same Δ used for the telluride, the largest energy shift induced by the hybridisation is instead experienced by the electrons at the top of the valence band at ~ -0.1 and ~ -0.3 eV. Calculating the difference between the hybridised (blue) and normal state DOS (orange) multiplied by the energy scale, it is possible to visualise the different contributions to the energy gain (red curve) as shown in 5.15. It is worth highlighting that every electron below the Fermi level brings with it a negative energy contribution to the energy gain curve. Therefore, negative values indicate where the hybridisation lowers the electronic energy at that specific binding energy, while the red curve is above zero where the normal phase has a higher DOS than the hybridised one.

In $TiSe_2$, the electrons are mainly redistributed from the positive peak at the valence band top to lower energies as pointed by the negative contribution of the red curve, which is spread over a large energy range. Increasing the Te content, negative peaks are developed, representing a localisation of such contribution (which I will refer to as energy gain in the following) at energies closer to the Fermi level. In order to highlight such evolution of the energy gain from spread to localised, the electronic energy difference is simulated assuming a constant hybridisation strength of $\Delta = 42$ meV across the entire compositional range (Fig.5.16(a)).

Here the localisation of the energy gain is highlighted by the flat red feature spanning from

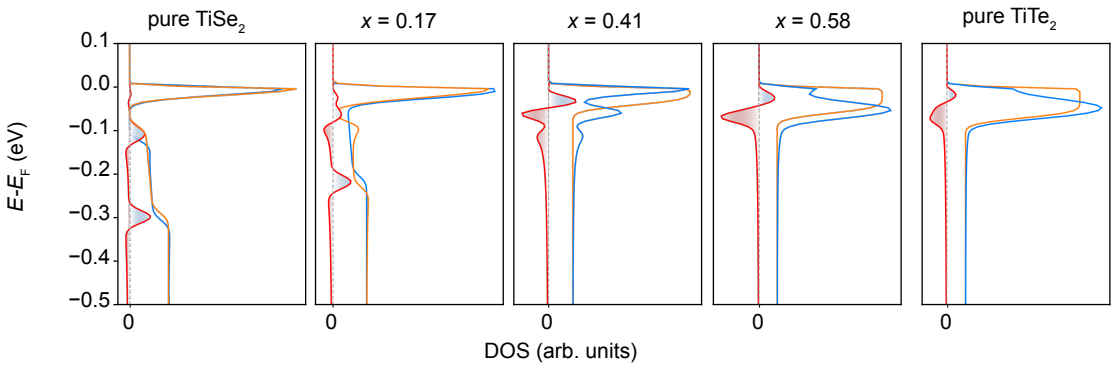

FIGURE 5.15: Normal (orange) and hybridised (blue) occupied DOS at different composition. The energy contribution of the electrons (red curve) is estimated by calculating the difference between the normal and hybridised occupied DOS multiplied by the energy scale.

pure $TiTe_2$ to $x \sim 0.5$ where the normal phase assumes a relatively strong semimetallic character. For lower Te content, such negative energy contribution splits into two branches following the energy shift of the hole bands in the normal phase until the semiconducting limit of the alloy series.

However, Δ is expected to vary in the real case with x depending on how the electron-hole and electron-phonon couplings change with the Te content. In Fig. 5.13(c), the energy gain is calculated assuming a linear dependence of Δ with the alloy composition, varying from 102 meV for the pure selenide to 42 meV for the telluride end. The increased hybridisation strength for $x \sim 0$ pushes the top of the two valence bands at much lower energies, enhancing the total energy gain at this end of the alloy series. As described in Chapter 2, one of the electron pocket in pure ML-$TiSe_2$ is only marginally involved in the hybridisation due to symmetry constraints and remains partially occupied even in the CDW phase. Actually, its minimum is pushed to slightly lower energies contributing to the reduction of the electronic energy. This additional contribution is now clearly visible in our simulation, represented by the negative (red) feature just below the Fermi level. Also in this calculation, the different energy gain branches are eventually merged together just below the Fermi level at larger x. Although the calculations presented in this section represent the energy difference of each electron between the normal and CDW states, an estimate of the total electronic energy difference between the two phases cannot be extracted from them. In order to extract such information, one has also to consider the modification of the periodic Coulomb potential induced by the lattice distortion that is expected to alter the potential energy of the electrons in the CDW phase.

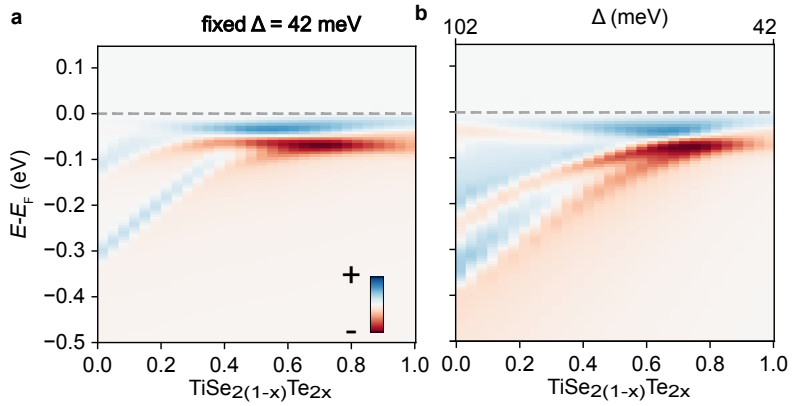

FIGURE 5.16: Evolution of the energy gain across the entire alloy series calculated with a constant $\Delta = 42$ meV (a) and a more realistic linear interpolation of Δ from 102 meV to 42 meV (b) for the selenide and telluride limits respectively.

5.8 Discussion and outlook:

This chapter reports the proof of principle that the CDW phase in 2D Ti-base dichalcogenides can be engineered by chemical substitution tuning the composition of the $TiTe_{2x}Se_{2(1-x)}$ alloy. Preliminary estimation of the critical temperature suggests a fast suppression of the CDW strength as soon as $TiSe_2$ is doped with Te ($x = 0.15$), while for $x = 0.58$ the critical temperature is already equivalent to pure ML-$TiTe_2$ one. For compositions close to pure $TiTe_2$, our minimal model predicts a localised energy gain just below the Fermi level, which is spread on a wider energy range approaching the selenide limit. Such evolution in the energy gain seems to correlate with the variation of T_{CDW} observed experimentally, although the relationship between these two trends if it exists, is still unclear. In fact, the critical temperature depends strongly on the strength of the CDW interaction, which may vary from the linear approximation used in the calculation of the electronic energy gain. Thus, further ARPES measurements are needed in order to fill the proposed phase diagram and provide information about the hybridisation strength at different compositions, which can be extracted by fitting the ARPES data with spectrum simulations based on our minimal model as done for ML-$TiTe_2$ in Chapter 4.

Further studies on the CDW microscopic mechanism would also be beneficial to determine how the electron-hole and electron-phonon couplings vary across the alloy series. These two microscopic mechanisms are both Coulomb interactions in nature; thus, both can be weakened by electronic screening. The low energy band structure of these materials can be approximated by 2D parabolic bands that generate a constant DOS along their bandwidth. For composition $x > 0.5$ where the extrema of both electron and hole pockets are above the Fermi level, the number of free

charges remains almost constant in the normal state; thus, the screening environment is expected to remain almost equivalent to pure ML-$TiTe_2$ there. Instead, a much lower overall screening is expected for alloy contents close to the pure selenide limit since the only band crossing the Fermi level is the conduction band, which is only populated due to defects anyway. When the valence band approaches the Fermi level, it starts contributing significantly to the screening as some electronic states become unoccupied. Moreover, the electronic susceptibility at this composition is expected to vary strongly with the temperature as also predicted by the calculation in Ref. [40] for pure $TiSe_2$. Thus, calculating the electronic susceptibility from our tight binding model would bring further insight to understand how the hybridisation strength varies across the alloy series. Another important contribution to the energy of the system is provided by the lattice potential. The atomic distortion forms trimers comprising two chalcogenides and one Ti ion that attract the electrons stabilising further the periodic charge density. However, such lattice displacement costs elastic energy limiting the amplitude of the distortion as described in Chapter 2. Thus, the intimate interplay between the electron and ionic subsystems is an essential ingredient in order to describe the temperature dynamics of the CDW phase.

Chapter 6

CDW of $TiSe_2$ on functional substrates

In the previous two chapters, the CDW instability in Ti-based dichalcogenides was manipulated by controlling intrinsic properties of the film: its dimensionality and low energy band structure. A third method is proposed in this chapter involving an extrinsic property of the system instead: the external screening environment imposed by the substrate. As discussed in chapter 2, the CDW transition is driven by the electron-hole and/or electron-phonon interactions that are both electrostatic forces in nature. The electric field between electrons and positive charges (holes or ions) propagates inside and outside the 2D material, as shown in Fig. 6.1(a). The free electrons within a metallic substrate are expected to screen the external part of the electric field, partially reducing the coupling strength between the two particles and resulting in a weaker CDW instability. For substrates with lower charge carrier density, the screening becomes less effective, and the electric field lines permeate deeper inside the underlying material strengthening the CDW. In the case of an insulating substrate, the CDW coupling would be completely unscreened and thus maximal. In the last few years, this paradigm has been explored by growing ML-$TiSe_2$ showing an enhancement of the CDW critical temperature reported up to 242 ± 10 K using the semiconducting substrate MoS_2 compared to the semimetal HOPG [30] (T_c = 200 K) as shown in Fig. 6.1(b). Bilayer graphene can be considered an intermediate substrate with a lower carrier density than HOPG, where T_c is only slightly increased to 220 K.

Such a trend is consistent with the modification in the external screening environment induced by the three different substrates, although the experimental evidence reported so far does not exclude the possibility that other factors can cause such deviation in T_c. One would expect that the band bending at the interface induced by the different chemical potential of the two materials might change to occupation of the conduction band and effectively dope the dichalcogenide layer affecting in turn the CDW instability. However, as observed with ARPES in Ref. [30], the different substrates don't induce a variation in the $TiSe_2$ chemical potential. Moreover, the substrate work

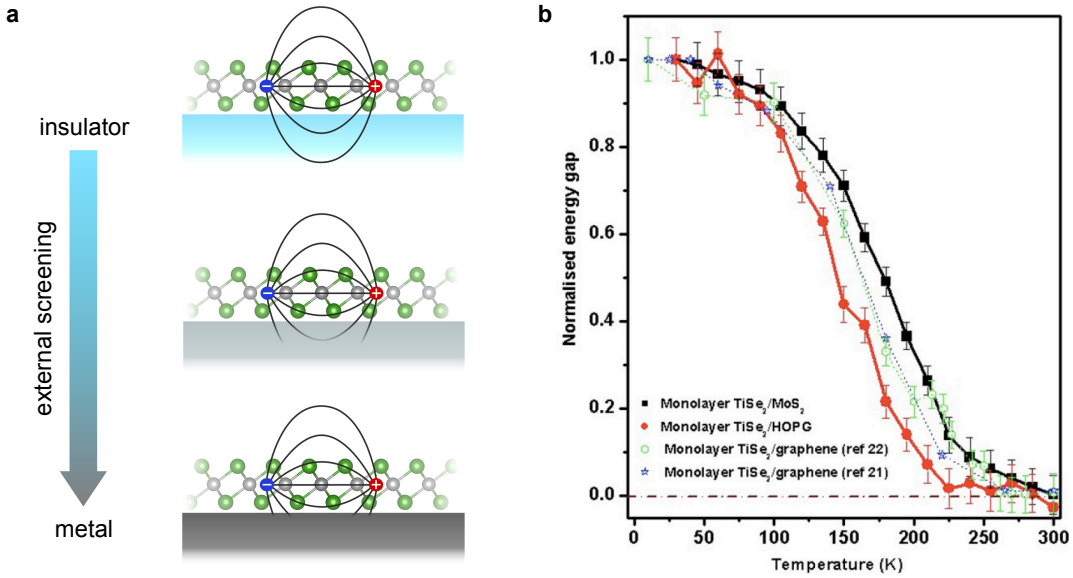

FIGURE 6.1: (a) The microscopic interaction driving the CDW transition in ML-$TiSe_2$ can be screened using a metallic material as substrate. (b) Temperature dependence of the CDW gap in ML-$TiSe_2$ grown on different substrates showing a higher critical temperature for ML-$TiSe_2$/ MoS_2 (semiconducting substrate) than ML-$TiSe_2$/ HOPG (semimetallic substrate). Adapted from Ref [30].

functions (4.55-4.9 for MoS_2 eV [110], 4.3 eV for BLGr/SiC and 4.55 eV for HOPG [111]) don't correlate with the observed trend in T_c. Another factor is the different phonon-phonon coupling at the interface between $TiSe_2$ and the various substrates which might affect the CDW phase in a way that hasn't been investigated yet. In order to exclude such undesired variations in the substrate film coupling, it would be ideal to use a substrate able to switch between an insulating and metallic state. Additionally, such material has to provide a triangular surface lattice suitable for the van der Waals epitaxy of 2D 1T-$TiSe_2$. A promising candidate is V_2O_3(0001) which undergoes a dramatic metal-to-insulator transition, one of the most pronounced among all materials known so far.

6.1 Metal to insulator transition in V_2O_3

Many stoichiometries of vanadium oxides exist due to the tendency of this transition element to assume a wide range of different oxidation states from +2 to +5. As a result, its phase diagram is populated with no less than 16 homogeneous structures [112], most of them showing a metal-to-insulator transition (MIT) as shown in Fig 6.2(a). In particular, the electrical resistivity (ρ) of V_2O_3 shows a very sharp discontinuity with a step of more than seven orders of magnitude at 140 K [113]. At high temperatures, this material is stable in a paramagnetic metallic phase having a corundum-like crystal structure (Fig 6.2(b)), where oxygen ions arrange in a hexagonal

closest packing (HCP), and V(III) ions occupy $2/3$ of the octahedral sites. The crystal field splits the V $3d$ orbitals into the doubly degenerate e_g and triply degenerate t_{2g} states, similar to that which occurs for the Ti $3d$ orbitals in $TiSe_2$. The t_{2g} levels are further split in a_{1g} and $e_{g\pi}$ due to trigonal distortion of the octahedron. However, the energy gap between these states is closed by the finite width of the bands derived from these orbitals. As a result, both a_{1g} and e_g^{π}-derived bands are partially filled, allowing for the metallic character of the material. Cooling V_2O_3 below T_c, an antiferromagnetic insulator phase emerges characterised by a monoclinic structure due to the displacement of the V atoms inside the octahedral sites [113]. The formation of V-V pairing through the edge-sharing oxygen bound in the distorted phase promotes the antiferromagnetic ordering between the t_{2g} orbitals. The large Coulomb repulsion ($U = 2.5$ eV) between the electrons on the same V site splits the $e_{g\pi}$ states in the so-called lower and upper Hubbard sub-bands, inducing an effective gap of 0.5 eV with the a_{1g} state that is now completely unfilled. The dramatic change in the metallic character of V_2O_3 makes this material a promising functional substrate able to switch the external screening environment experienced by $TiSe_2$ placed on top. Above the MIT critical temperature T_{MIT}, the CDW phase in the TMD film would be expected to be completely or partially suppressed, showing, in the latter case, a weaker hybridisation between the conduction and valence bands. Below T_{MIT} instead, the substrate would become insulating, leading to an enhancement of the CDW band gap in $TiSe_2$. For this purpose, the hysteresis of the substrate MIT would allow a direct comparison between the CDW gap measured at the same temperature but with the substrate in two different phases. T_{MIT} can also be tuned accordingly with the phase diagram in Fig. 6.2(b), for example, by doping the material with Cr or Ti [114].

Moreover, its (0001) surface shows a triangular lattice in principle suitable for the epitaxy of $TiSe_2$. The large lattice mismatch between V_2O_3 and $TiSe_2$ (V_2O_3= 4.972 Å; $TiSe_2$= 3.533 Å) would be completely relaxed if the two materials interact through van der Waals coupling. According to the current literature, the unconventional epitaxy of 1T-$TiSe_2$ on V_2O_3(0001) has not been attempted yet. Wang et al. [116] have successfully grown a few layers of $TiSe_2$ on an isostructural substrate, namely Al_2O_3(0001) where $TiSe_2$ grows rotated by 30° with respect to the underlying lattice in order to minimise the high lattice mismatch. However, their epitaxial process involves the preliminary deposition of a buffer layer between the two materials, while, for our purpose, a sharp interface is required. Since V_2O_3 substrates are not commercially available, the first step consists of growing such material in our oxide MBE system.

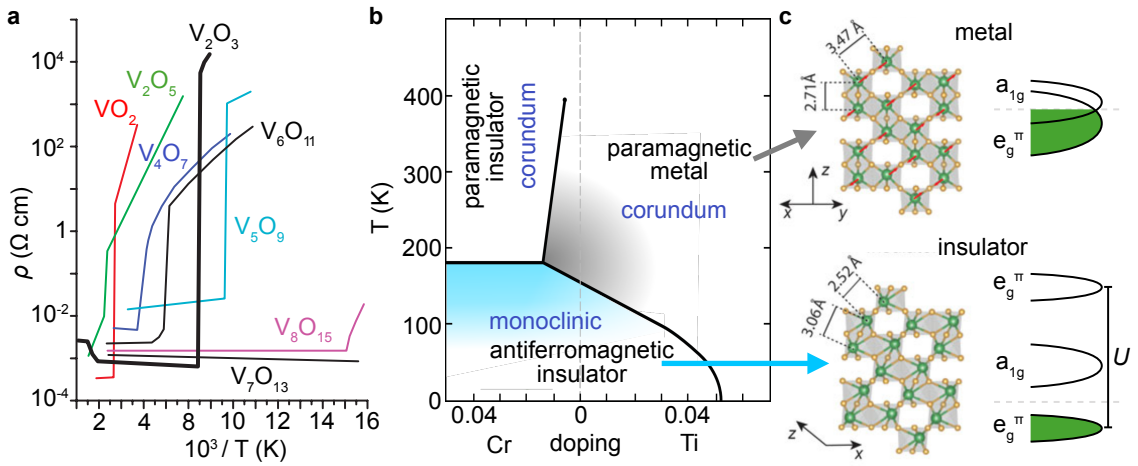

FIGURE 6.2: (a) Metal to insulator transition in vanadium oxides, adapted from Ref. [115]. (b) Phase diagram of V_2O_3, adapted from Ref. [114]. (c) Schematics of the lattice distortion and relative change in the electronic energy levels occurring at the MIT of V_2O_3. adapted from Ref. [113]

.

6.2 Growth of V_2O_3

In this section, the preliminary deposition of V_2O_3 is discussed. Sapphire or α-Al_2O_3(0001) is the most common substrate for V_2O_3 epitaxy because it has the same corundum crystal structure and an in-plane lattice constant of 4.765, which is $\approx 4.5\%$ smaller than the epilayer. In Fig. 6.3(a), the RHEED pattern of sapphire (0001) shows strong Kikuchi lines and sharp diffraction spots split vertically due to the step-terrace morphology of the surface visible in the AFM image in (b). Despite the large number of different vanadium oxides, the growth of stoichiometric V_2O_3 is achievable within a relatively large range of temperatures from 770 to 1120 K and deposition rates as reported by Dillemans et al. [117].

For this growth, I used the oxide MBE chamber (GM1) connected to the UHV facility in St. Andrews (see section 3.1.2 for details and the whole apparatus). GM1 is equipped with a piezo leak valve for delivering the desired partial pressure of oxygen inside the chamber and a high-temperature effusion cell filled with vanadium. A quartz microbalance is installed on a retractable arm and positioned just under the sample in order to calibrate the V flux before the deposition. Since the MIT in V_2O_3 becomes broader in temperature for films thinner than $\sim$10 nm [118], a V flux of 0.065 Å/s was chosen for this growth in order to obtain a V_2O_3 film with a nominal thickness of several tens of nm. Because Se might severely contaminate the oxide chamber, the flagstyle sample holder, which will be covered with Se after the successive growth of $TiSe_2$ in GM2, has to be carefully decontaminated before being used again in GM1.

The process starts by loading the sapphire substrate in GM1 and heating the substrate up to the growth temperature of 900° C under an O_2 partial pressure of $2{\cdot}10^{-6}$ mbar in order to avoid the formation of oxygen vacancies on the Al_2O_3 surface. During the first minutes of the growth, the RHEED pattern becomes more diffuse, with new blurred streaks appearing over the Al_2O_3 spots indicating the deposition of the first layers of V_2O_3. During the growth, the new pattern becomes more intense and starts developing elongated spots suggesting a roughening of the surface morphology. Fig. 6.3(a) shows the sharp RHEED pattern obtained after 2 hours of growth, where the V_2O_3 film results completely relaxed from the epitaxial strain since the new reciprocal lattice constant is $4.5{\pm}0.5\%$ smaller than the original substrate pattern.

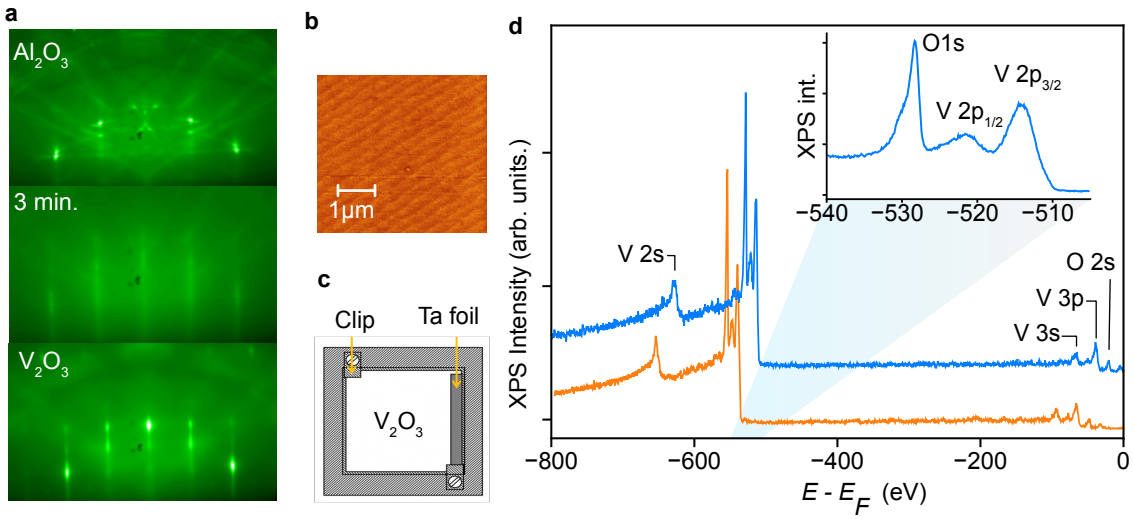

FIGURE 6.3: (a) RHEED pattern at different stage of the V_2O_3 epitaxy on Al_2O_3. (b) AFM image of the Al_2O_3 substrate measured before the growth showing the well ordered step terrace morphology of the surface. (c) Schematic of the Ta foil introduced to improve the contact with V_2O_3 layer and avoid charging effects during the photoemission or LEED characterisations. (d) XPS spectra of epitaxial V_2O_3 measured *in situ* with (blue) and without (orange) Ta foil.

The XPS spectrum of the as-grown film was measured *in situ* to check its chemical composition. However, the insulating substrate prevents the V_2O_3 film from being in electrical contact with the analyser resulting in a positive charging of the sample during the measurement as the photoemitted electrons are not adequately replaced. In order to prevent the sample charging, a Ta foil was placed at the edge of the Al_2O_3 substrate before the growth, allowing a direct electrical connection with the deposited V_2O_3 film as shown in Fig. 6.3(c). As a result, the XPS spectrum measured with Ta contact is shifted by $\sim$ 25 eV towards lower binding energies, showing the core levels of V (3p, 3s, 2p, 2s) and O (2s and 1s) at energies consistent with the values reported in the literature. The inset shows in detail the O 1s and the V 2p peaks; these latter split further

in V $2p_{1/2}$, V $2p_{3/2}$ duplet by spin-orbit coupling. Asymmetric shoulders at higher binding energies are clearly visible for both the O and V peaks, indicating at least two different chemical environments surrounding these elements at the surface. Indeed the surface of V_2O_3 is usually terminated by a vanadyl (V=O) group, where the top most O atom saturates the dangling bond of the underlying V [119]. The high energy electrons used for the RHEED measurements can desorb the top most O atom leaving a V-rich surface having an XPS spectrum characterised by the shoulders observed in our data [120]. In order to exclude the presence of other parasitic phases, the as-grown films were characterised with X-ray diffraction (XRD). This technique measures the intensity of X-rays diffracted by the bulk crystal lattice, probing the out-of-plane lattice constant of the materials composing the sample. Fig. 6.4(a) shows the (0001) diffraction peaks of Al_2O_3 and V_2O_3, the latter characterised by the typical fringes caused by the thin film interference of the X-ray radiation. No diffraction pattern related to other V_yO_x phases was observed in the XRD spectrum, demonstrating the successful epitaxy of single phase V_2O_3 thin film. Moreover, the temperature-dependent resistance measurements performed by the master student Paddy Hogan (Andreas Rost group) confirm the deposited film undergoes a MIT at ~ 150 K, consistent with the typical T_{MIT} of V_2O_3 thin films as reported in Ref. [121]. As shown in Fig. 6.4(b), the film resistance starts increasing already at $\sim$200 K, suggesting the presence of domain boundaries, probably at the interface with the sapphire substrate. Nevertheless, the abrupt change in the film resistance provides the desired functionality to switch the external screening environment and manipulate the CDW instability in the $TiSe_2$ layer deposited on top of V_2O_3(0001). As shown in Fig. 6.4(c), the AFM topographic images of the sample surface reveal the presence of small islands a few nm high and having lateral size of $100 - 200$ nm. These islands are not randomly distributed on the surface but partially aligned in parallel lines, probably following the step terrace morphology of the underlying substrate. Such nano-islands on the V_2O_3 surface can be detrimental to the successive growth of $TiSe_2$, limiting the lateral extension of the TMD domains and, in general, its crystal quality. However, despite the rough surface morphology, the LEED pattern shown in Fig. 6.3(d) suggests a sufficiently ordered surface, at least on the atomic scale, that can provide a suitable epitaxial template for the $TiSe_2$ deposition.

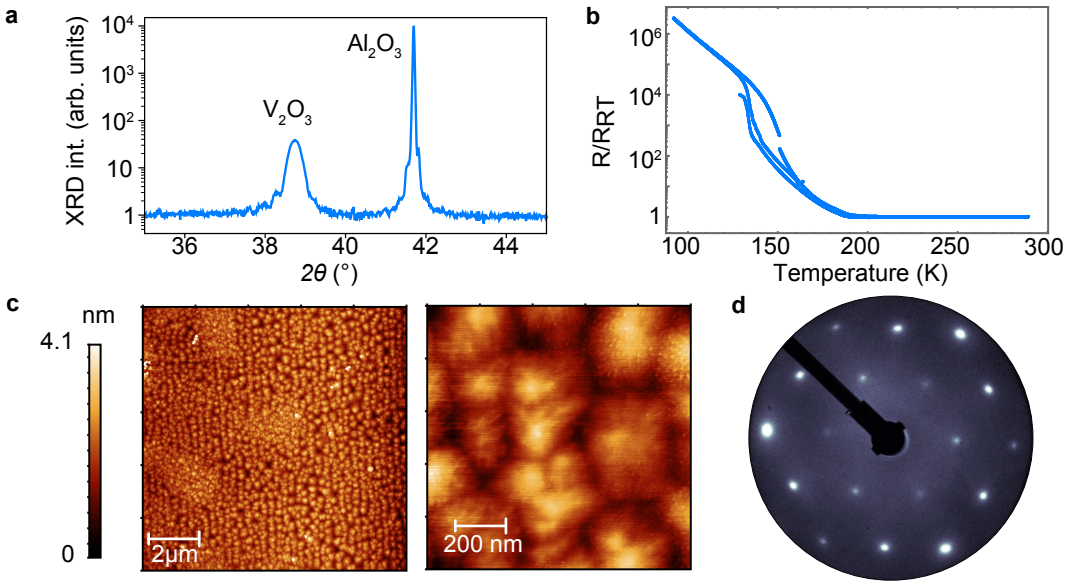

FIGURE 6.4: (a) XRD (0002) peaks of V_2O_3 thin film grown on Al_2O_3. (b) Resistance measurements of the sample in (a) showing the signature of the MIT in V_2O_3. (c) AFM images of the V_2O_3 surface characterised by small islands. (d) LEED pattern of the surface showing the sharp pattern of the V_2O_3 surface.

6.3 Growth of $TiSe_2$

After the growth of V_2O_3 on Al_2O_3, the samples were transferred *in situ* into the chalcogenide MBE chamber (GM2) for the next step: the ML-$TiSe_2$ epitaxy. The first deposition attempts using a growth temperature of $\sim 600°$ C resulted in a very blurred RHEED pattern indicating the poor crystal quality of the chalcogenide film. Growing the TMD at higher temperatures ($\sim 900°$ C) instead, new sharp RHEED streaks appears during the growth, as shown in Fig. 6.5. During the first 10 minutes, a new weak pattern appears, having a periodicity of $1/3$ compared to V_2O_3 reciprocal lattice constant. The microscopic structure of this initial reconstruction is still unknown, although the Ti or Se ad-atoms clearly induce it. However, its RHEED pattern remains weak and is quickly replaced by a more complex diffraction signal. This latter comprises multiple peaks with different intensities and becomes gradually more intense as the growth continues. Noticeably, the deposition rate at such a high growth temperature is much slower than the 1 ML/70 minutes achieved at $400°$C during the conventional growth of ML-$TiSe_2$ on BL-Gr/SiC(0001). Indeed, after two hours of deposition, the substrate RHEED pattern is still clearly visible.

In order to understand the origin and the new periodicity of the deposited film, the line cut extracted from the RHEED pattern measured after growth is fitted with several Lorentzian peaks and a cubic background (green) as shown in Fig. 6.6(a). The light blue peaks represent the RHEED

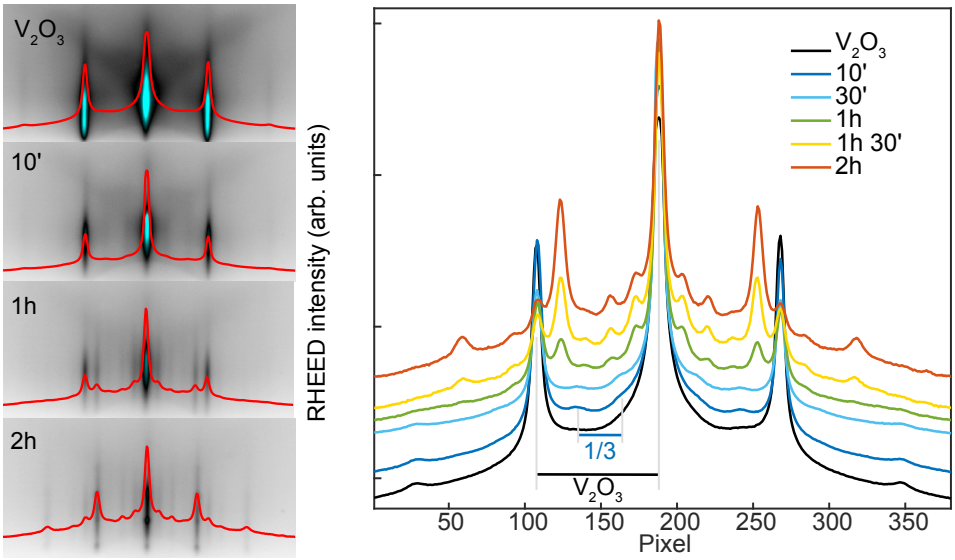

FIGURE 6.5: RHEED pattern evolution during the growth of $TiSe_2$ on V_2O_3(0001) showing at first the appearing of an unknown 1/3 reconstruction and a successive more complex pattern with different periodicity.

streaks of the V_2O_3 substrate, while the peaks related to the chalcogenide film are coloured in orange. These latter are equally spaced and superimpose the substrate peaks after five repetitions, suggesting the deposited layer generates a commensurate (5×5) superlattice on the V_2O_3 surface.

Rotating the crystal by 30°, the surface reciprocal lattice is now probed along the (11) surface direction indicated in Fig. 6.6(a). Since the distance between V atoms is larger in this direction, the spacing of the V_2O_3 pattern is reduced by a factor of$\sqrt{3}/2$ compared to the RHEED measured along the (10) direction. Curiously, the periodicity of the TMD film is instead larger compared to the (10) direction by a factor of $2/\sqrt{3}$. This strongly suggests that the deposited film has a triangular symmetry and is rotated 30° with respect to the V_2O_3 substrate. Assuming such a rotated configuration, the unit cell of the R30°-$TiSe_2$/V_2O_3 heterostructure would appear as shown in Fig. 6.6(b), where the light blue dots denote the uppermost V layer of the substrate surface, while the orange and green dots represent the Ti and the Se atoms respectively. After five V_2O_3 unit cells two lattices become almost commensurate, resembling the $1/5$ periodicity observed in the RHEED pattern along the (10) direction. Using the Matlab app RHEEDsim [122], the RHEED pattern of such heterostructure is simulated within the kinematic approximation. In order to have a well defined unit cell the $TiSe_2$ lattice was slightly strained by $+0.122\%$ obtaining a perfectly commensurate superstructure. Such weak tensile strain is too small to be identified with RHEED, and might actually be present in the deposited film. The simulated diffraction peaks are shown with green lines in Fig. 6.6(a) for both crystallographic orientations. The calculation correctly simulates

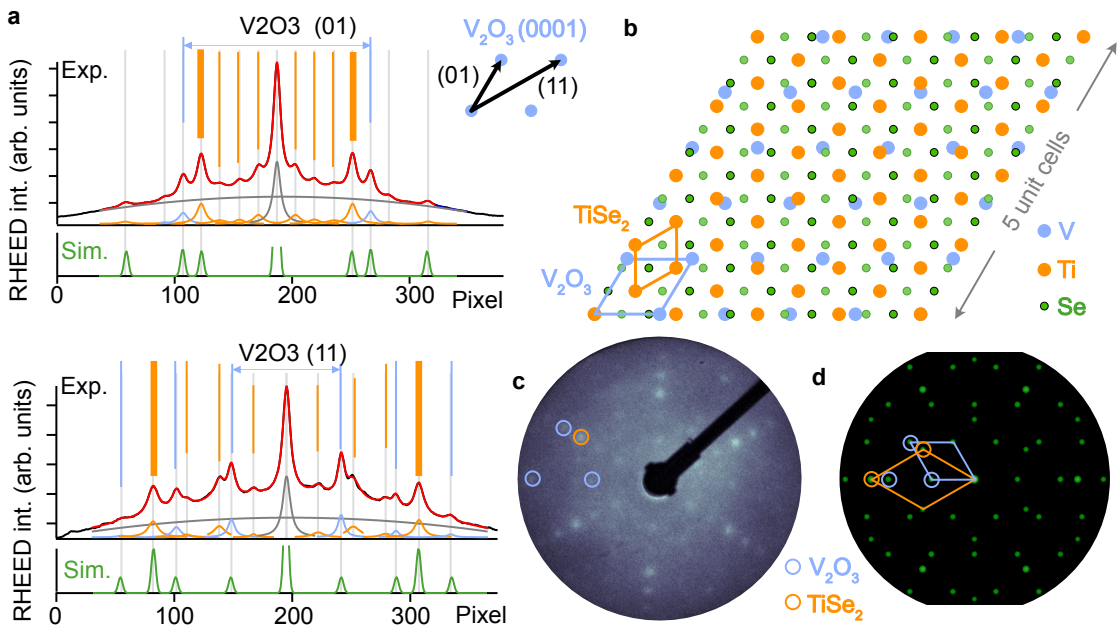

FIGURE 6.6: (a) Fitting of the RHEED pattern measured after the growth of $TiSe_2/V_2O_3$ along the (01) and (11) surface direction. (b) Unit cell R30°-$TiSe_2/V_2O_3$(0001) heterostructure used to simulate the RHEED pattern (green line in (a)). (c-d) Experimental and simulated LEED of the surface.

the substrate pattern and the chalcogenide film's most intense peaks denoted with the bold orange lines. The other $1/5$ RHEED streaks observed experimentally can be related to the expected moiré pattern formed by the interference between the two lattices. In general, the interaction between epilayer and substrate can induce a displacement of the atoms within the unit cell compared to their positions in the free-standing configuration used for the simple calculation presented here. Such distortion is expected to modulate the relative intensity of the RHEED streaks enhancing the moiré diffraction pattern. In principle, one can fine tune the atomic positions to match the experimental intensity, but this goes beyond the purpose of the preliminary study performed in this work. The moiré reciprocal lattice is also clearly visible in the LEED image shown in Fig. 6.6(c) where the diffraction spots of the V_2O_3 and $TiSe_2$ films are highlighted in blue and orange, respectively, in agreement with the simulated LEED pattern shown in Fig. 6.6(d).

6.4 ARPES on $TiSe_2$/ V_2O_3

The electron diffraction analysis discussed in the previous section demonstrates $TiSe_2$ grows on the surface of the V_2O_3 functional substrate despite the presence of the nano-island on the surface of the latter. Exploiting the facilities available in our lab in St. Andrews, the sample

is then transferred to the ARPES system where the band structure of the dichalcogenide film was measured *in-situ* at 110 K. Fig. 6.7(a) reveals the typical band structure of $TiSe_2$ with the valence band at Γ and the conduction band bottom at M. However no signature of the CDW phase is evident as the spectrum is considerably more diffuse compared to the sample grown on BL-Gr/SiC(0001) reported in the previous chapters. Moreover, the electron pocket is significantly larger, suggesting the formation of a considerable amount of Se vacancies during the growth at such high temperature. Similar occupation of the conduction band has also been observed before for $TiSe_2$/BL-Gr samples grown at high T (650°C), showing a complete suppression of the CDW phase at such high doping level [39]. Therefore, the high temperature used during the deposition is detrimental for the lattice instability as well as for the overall crystal quality. Another factor limiting further the film's crystallinity is the roughness of the substrate surface. In Fig. 6.7(b), the AFM image of the sample surface after the $TiSe_2$ growth. On the background, the substrate surface characterised by a few nm high islands with later size of $\sim$ 200 nm is visible, although covered by other higher aspect ratio domains. Since the measurement was performed in air, it is not possible to distinguish if these latter are $TiSe_2$ islands or air particles adsorbed on the surface. The rather square shape of some of them seems not compatible with the triangular crystal structure of $TiSe_2$ pointing to this second option.

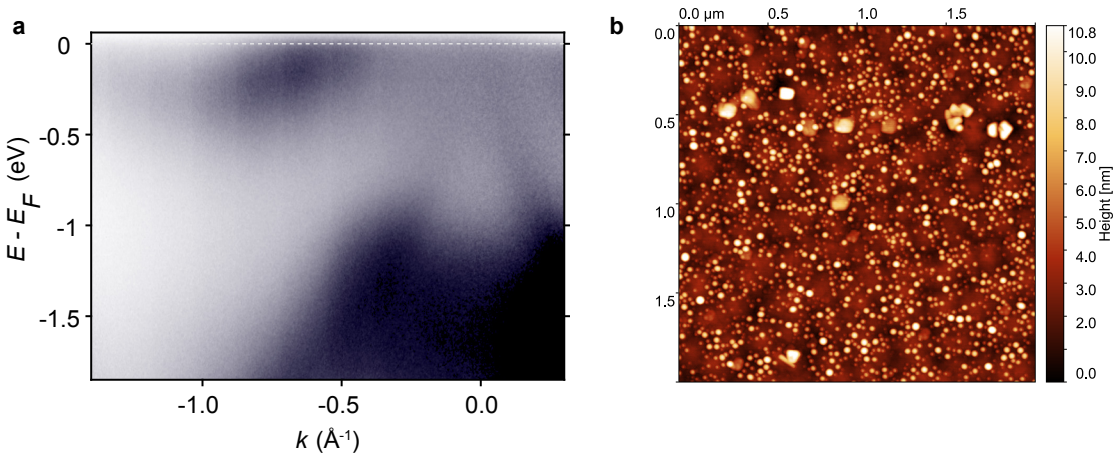

FIGURE 6.7: ((a) Diffuse band structure of $TiSe_2/V_2O_3$ along Γ-M measured with ARPES at 110 K, showing a substantial n-doping which in turns suppresses the CDW phase in the TMD. (b) AFM image of the sample surface after the TMD growth measured *ex situ*.

6.5 Conclusion

As evident from the ARPES and AFM data shown in the previous section, the growth of ML-$TiSe_2$ on V_2O_3(0001) reveals several difficulties. Despite the successful functionalisation of the substrate with a prominent MIT, the rough morphology of the V_2O_3 surface is not ideal for the deposition of a 2D material due to the persistent presence of nanoislands. Different process parameters and post-deposition annealing have been attempted without significantly improving the surface condition. Moreover, the relatively high temperature needed to obtain a sharp $TiSe_2$ RHEED pattern promotes the formation of Se vacancies that, in turn, suppress the desired CDW transition. In this perspective, post-deposition annealing in Se rich environment can improve the crystal quality of the TMD film, although the substrate roughness would always limit its domain size.

The smooth appearance of $TiSe_2$ RHEED pattern and the simultaneous fade out of the V_2O_3 one suggests the formation of a sharp interface between the two materials without any amorphous buffer layer. However, a weak $1/3$ diffraction pattern is observed during the few first minutes of the growth which points to the formation of a possible intermediate structure between the oxide surface and the 2D material. The nature of this $1/3$ reconstruction and its role in the $TiSe_2$ epitaxy are still unknown. Curiously, the $1/3$ diffraction pattern appears only during the co-deposition of Ti and Se but not depositing the single element individually. Indeed, V_2O_3(0001) is remarkably inert to Se as its RHEED pattern doesn't change when its surface is kept at 900°C for several hours under high Se flux. Exposing the substrate to Ti only, a RHEED pattern consistent with a $TiVO_3$ reconstruction appears instead. When this $TiVO_3$ surface is exposed to Se, Ti quickly forms $TiSe_2$, but even this time, no $1/3$ intermediate RHEED pattern was observed during the process.

The relatively intense moiré pattern observed with RHEED and LEED suggests $TiSe_2$ strongly interacts with the substrate. Another hint of such strong coupling is evident from a curious change in the LEED pattern shown in Fig. 6.8(a-b) when the sample is cooled below the substrate T_{MIT}. At low temperatures, the diffraction spots of V_2O_3 and $TiSe_2$ split into triangles under the substrate lattice distortion characterised by the tilting and elongation of the hexagonal unit cell of the oxide [123]. Thus, three equivalent distorted domains rotated 120° with respect to each other are expected to generate the three hexagonal diffraction patterns highlighted in Fig. 6.8(c). This phenomenon was already observed with XRD on V_2O_3 bulk crystals, but in this case, the substrate lattice distortion propagates in the $TiSe_2$, suggesting a strong structural coupling between

the two materials. Further analyses are needed to achieve a better understanding of this intriguing heterostructure.

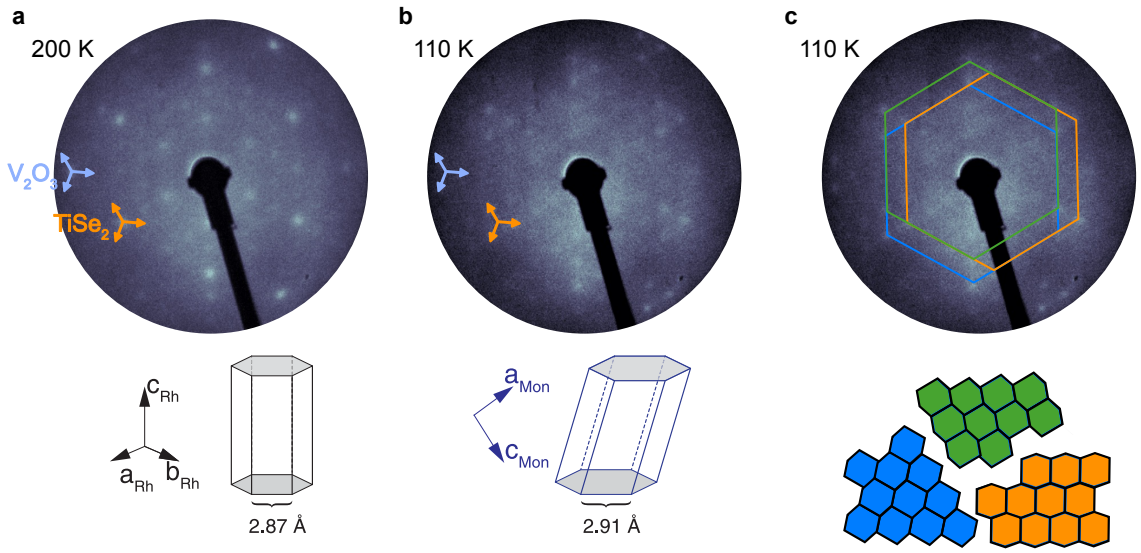

FIGURE 6.8: (a-b) Splitting of $TiSe_2$ and V_2O_3 LEED pattern (e-beam KE=132eV) into triangles when the sample is cooled from 200 K to 110 K. This phenomenon might be related to the tilting and elongation of the V_2O_3 hexagonal unit cell, sketches of the unit cell adapted from Ref. [123]. (c) A possible interpretation of the pattern is the superposition of three equivalent distorted hexagons rotated in three different directions.

Since one of the main issue of the process explored in this chapter concerns the growth of ML-$TiSe_2$ on the oxide surface, one can consider other materials, possibly van der Waals, to use as functional substrate for the selenide. A promising candidate is 1T-TaS_2. This material exhibits a sharp transition from a nearly commensurate NCCDW phase to a commensurate $\sqrt{13}$x$\sqrt{13}$ CCDW phase [124] that could be used for modulate the external screening environment of the ontop ML-$TiSe_2$ film, replacing the MIT in V_2O_3 (Fig. 6.9). Although, the resistivity change between the CCDW and NCCDW phases would be much smaller than the one realised in the V_2O_3 MIT (7 order of magnitude for the oxide against only one for the sulfide), the transition in TaS_2 exhibits an interesting hysteresis that strongly depends on the film thickness. For films thick 42 nm such hysteresis is $\sim$ 100 K wide, much larger than the MIT observed in Fig. 6.4(b). This would provide a direct comparison of the $TiSe_2$ CDW phase in the two substrate states at the same temperature.

Although the functional substrate method presented in this chapter has not yet led to the desired manipulation of the CDW instability in ML-$TiSe_2$, the successful epitaxy of a TMD on top of a highly correlated oxide might pave the way for the realisation of similarly interesting heterostructures where other exotic physics phenomena might emerge.

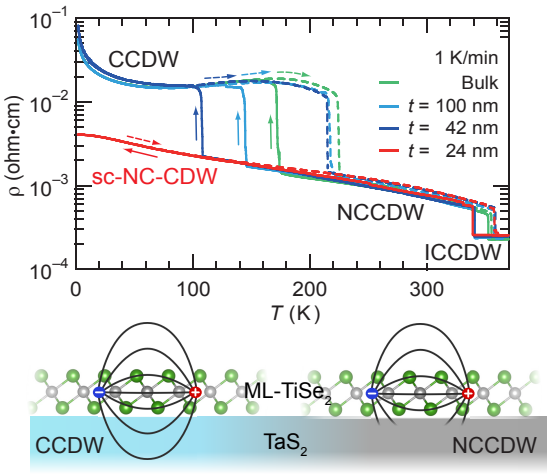

FIGURE 6.9: The CDW transition in TaS_2 shows a promising change in resistivity that could be used to replace the MIT transition in V_2O_3. The CCDW to NCCDW transition in TaS_2 might be used to alter the external screening environment surrounding ML-$TiSe_2$ above, and influence the CDW instability in this latter. Adapted from Ref. [124]

Chapter 7

Conclusion and outlook

This concludes the work performed during my PhD concerning the manipulation of charge density wave (CDW) instabilities in Ti-based dichalcogenides. The unconventional electronic collective phase emerging at low temperatures in this class of materials has fuelled an intense research field in the last 50 years aiming to understand the microscopic interactions driving this lattice instability. Here, three different experimental approaches were proposed for modulating the CDW interaction in these compounds.

In chapter 4, the electronic band structure of $TiTe_2$ was modified by changing the dimensionality of the system enabling the emergence of a (2×2) CDW phase at the two dimensional (2D) limit. Density functional theory calculations provided by my collaborators unveiled the intrinsic nature of such lattice instability in the monolayer and its structural similarity with the one occurring in ML-$TiSe_2$. A careful ARPES analysis of the ML-$TiTe_2$ band structure evolution across its CDW transition unambiguously evidences the hybridisation between the electron and hole pockets occurring in the ordered phase. The mirror symmetry breaking at the phase transition imposes fundamental symmetry selection roles for the mixing of these electronic states, modulating the CDW gap in the momentum space. Such orbital selective hybridisation enables a substantial stabilisation in the electronic system providing the energy gain in driving the CDW transition in the monolayer compound. In the bulk instead, a substantial out-of-plane band dispersion misaligns in energy the bands and drives a relevant modification of their orbital character. Together, these two effects completely suppress the energy gain in the multilayer crystal. As such band structure modification is common in other 1T-TMDs, this mechanism can manifest itself in other members of the material family such as $ZrTe_2$ and $HfTe_2$.

Noticeably, our estimation of the hybridisation strength in ML-$TiTe_2$ (Δ= 42 meV) is weaker than in ML-$TiSe_2$ (Δ= 102 meV). This difference suggests another method for tuning the CDW

interaction in these systems by chemically substituting Te with Se. This underpins the work described in chapter 5, where 2D $TiTe_{2x}Se_{2(1-x)}$ alloys were successfully grown with molecular beam epitaxy. By controlling the film composition, the indirect electronic band gap of such system was engineered, achieving an effective semiconductor to semimetal transition from pure ML-$TiSe_2$ to pure ML-$TiTe_2$. A (2×2) CDW phase was observed with ARPES at low temperature across the entire 2D alloy series, showing signatures of the same orbital selective hybridisation observed in ML-$TiTe_2$. Extracting the critical temperature from the ARPES data, a preliminary phase diagram was proposed showing a relatively quick partial suppression of the lattice instability for $TiTe_{2x}Se_{2(1-x)}$ with x close to zero, while for $x > 0.58$ the critical temperature remains constant up to pure $TiTe_2$. The hybridisation strength at different compositions can be in future extracted using the minimal model developed for ML-$TiTe_2$ providing information regarding the modulation of the CDW interaction across the entire compositional range. Electronic susceptibility calculations might also bring useful insight into how the internal screening environment varies across the semiconductor to semimetal transition and influence the lattice instability at different x.

In chapter 6, preliminary attempts for tuning the external screening environment surrounding ML-$TiSe_2$ were reported. This material was successfully deposited on a functional substrate consisting of a V_2O_3 film which undergoes a metal to insulator transition (MIT) at ~ 140 K. However, due to high temperature used during the epitaxial process, the selenide films obtained were heavily n-doped, inducing the complete suppression of the CDW instability. Electron diffraction analysis also pointed to the strong coupling between the substrate and the TMD layer on top that promotes the splitting of the sample surface in multiple domains driven by the lattice distortion at the substrate MIT. Therefore, this last approach reveals several limitations that can be overcome by replacing the V_2O_3 substrate with another functional material such as 1T-TaS_2.

A new appealing approach has been recently demonstrated to be highly effective in changing charge concentration within 2D materials [125]. Such method consists in fabricating a 2D heterostructure device illustrated in Fig. 7.1. The ML-MX_2 film is deposited on a h-BN film that insulates the TMD layer from a graphite back-gate. The monolayer is also grounded by a graphene flake ensuring the connection with a Pt contact. The charge concentration in the TMD film is therefore controlled by applying a gate potential using an external power supply. This kind of device is also compatible with ARPES and would allow the direct observation of how the CDW hybridisation changes depending on the gate doping in the ML-TiX_2 layer at a certain temperature. However, the fabrication of such heterostructure is a considerable task that needs specific facilities

and a careful integration of several processes. This method might provide an alternative route for further investigations on the charge density wave phase in Ti-based dichalcogenides. In addition to the other methods explored in this thesis, several future perspectives are open for controlling new collective states in these compounds and other 2D materials.

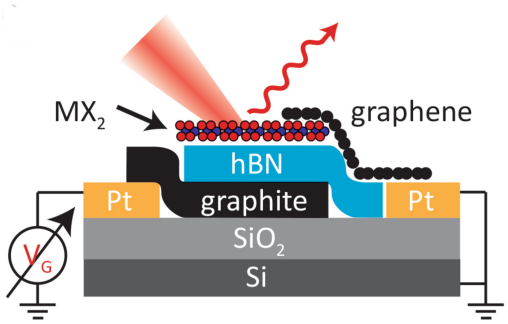

FIGURE 7.1: Schematics of a 2D heterostructure device incorporating a TMD layer (MX_2), allowing the gate doping of a TMD layer (MX_2) by controlling the gate voltage applied to the graphite back gate. Such a device is also compatible with ARPES experiments and might provide an alternative route for studying how the CDW phase in TiX_2 systems is affected by the charge carrier concentration within the material. Adapted from [125].

Bibliography

1. Novoselov, K. S. *et al.* Electric field effect in atomically thin carbon films. *Science* **306,** 666–669 (2004).

2. Li, L. *et al.* Black phosphorus field-effect transistors. *Nature Nanotechnology* **9,** 372–377 (2014).

3. Radisavljevic, B., Radenovic, A., Brivio, J., Giacometti, V. & Kis, A. Single-layer MoS_2 transistors. *Nature Nanotechnology* **6,** 147–150 (2011).

4. Splendiani, A. *et al.* Emerging photoluminescence in monolayer MoS_2. *Nano letters* **10,** 1271–1275 (2010).

5. Akinwande, D. *et al.* Graphene and two-dimensional materials for silicon technology. *Nature* **573,** 507–518 (2019).

6. Wang, Q. H., Kalantar-Zadeh, K., Kis, A., Coleman, J. N. & Strano, M. S. Electronics and optoelectronics of two-dimensional transition metal dichalcogenides. *Nature Nanotechnology* **7,** 699–712 (2012).

7. Yang, H., Kim, S. W., Chhowalla, M. & Lee, Y. H. Structural and quantum-state phase transitions in van der Waals layered materials. *Nature Physics* **13,** 931–937 (2017).

8. Gibertini, M., Koperski, M., Morpurgo, A. F. & Novoselov, K. S. Magnetic 2D materials and heterostructures. *Nature Nanotechnology* **14,** 408–419 (2019).

9. Morosan, E. *et al.* Superconductivity in Cu_xTiSe_2. *Nature Physics* **2,** 544–550 (2006).

10. Yang, J. *et al.* Charge-orbital density wave and superconductivity in the strong spin-orbit coupled $IrTe_2$:Pd. *Physical Review Letters* **108,** 116402 (2012).

11. Ugeda, M. M. *et al.* Characterization of collective ground states in single-layer $NbSe_2$. *Nature Physics* **12,** 92–97 (2016).

12. Wilson, J. A., Di Salvo, F. & Mahajan, S. Charge-density waves and superlattices in the metallic layered transition metal dichalcogenides. *Advances in Physics* **24,** 117–201 (1975).

13. Chhowalla, M. *et al.* The chemistry of two-dimensional layered transition metal dichalcogenide nanosheets. *Nature Chem.* **5,** 263–275 (2013).

14. Chuang, H.-J. *et al.* High mobility WSe_2 p-and n-type field-effect transistors contacted by highly doped graphene for low-resistance contacts. *Nano Letters* **14,** 3594–3601 (2014).

15. Chhowalla, M., Jena, D. & Zhang, H. Two-dimensional semiconductors for transistors. *Nature Reviews Materials* **1,** 1–15 (2016).

16. Manzeli, S., Ovchinnikov, D., Pasquier, D., Yazyev, O. V. & Kis, A. 2D transition metal dichalcogenides. *Nature Reviews Materials* **2,** 1–15 (2017).

17. Neto, A. C. Charge density wave, superconductivity, and anomalous metallic behavior in 2D transition metal dichalcogenides. *Physical Review Letters* **86,** 4382 (2001).

18. Bahramy, M. S. *et al.* Ubiquitous formation of bulk Dirac cones and topological surface states from a single orbital manifold in transition-metal dichalcogenides. *Nature Materials* **17,** 21–27 (2018).

19. Di Salvo, F. J., Moncton, D. E. & Waszczak, J. V. Electronic properties and superlattice formation in the semimetal $TiSe_2$. *Phys. Rev. B* **14,** 4321–4328 (1976).

20. Wilson, J. A. Concerning the semimetallic characters of TiS_2 and $TiSe_2$. *Solid State Communications* **22,** 551–553 (1977).

21. Cercellier, H *et al.* Evidence for an Excitonic Insulator Phase in 1 T- $TiSe_2$. *Physical Review Letters* **99,** 146403 (2007).

22. Rossnagel, K., Kipp, L. & Skibowski, M. Charge-density-wave phase transition in $1T - TiSe_2$: Excitonic insulator versus band-type Jahn-Teller mechanism. *Physical Review B* **65,** 235101 (2002).

23. Kogar, A. *et al.* Signatures of exciton condensation in a transition metal dichalcogenide. *Science* **358,** 1314–1317 (2017).

24. Hedayat, H. *et al.* Excitonic and lattice contributions to the charge density wave in 1 T-$TiSe_2$ revealed by a phonon bottleneck. *Physical Review Research* **1,** 023029 (2019).

25. Tam, C. C. *et al.* Charge density waves in infinite-layer $NdNiO_2$ nickelates. *Nature Materials,* 1–5 (2022).

26. Loret, B *et al.* Intimate link between charge density wave, pseudogap and superconducting energy scales in cuprates. *Nature Physics* **15,** 771–775 (2019).

27. Yu, F. *et al.* Unusual competition of superconductivity and charge-density-wave state in a compressed topological kagome metal. *Nature Communications* **12,** 1–6 (2021).

28. Chen, P *et al.* Emergence of charge density waves and a pseudogap in single-layer $\mathrm{TiTe_2}$. *Nature Communications* **8,** 516 (2017).

29. Kolekar, S., Bonilla, M., Ma, Y., Diaz, H. C. & Batzill, M. Layer- and substrate-dependent charge density wave criticality in 1T-$\mathrm{TiSe_2}$. *2D Materials* **5,** 015006 (2017).

30. Kolekar, S. *et al.* Controlling the Charge Density Wave Transition in Monolayer $\mathrm{TiSe_2}$: Substrate and Doping Effects. *Advanced Quantum Technologies* **1,** 1800070 (2018).

31. Watson, M. D. *et al.* Orbital- and k_z-Selective Hybridization of Se $4p$ and Ti $3d$ States in the Charge Density Wave Phase of $\mathrm{TiSe_2}$. *Physical Review Letters* **122,** 076404 (2019).

32. Ashcroft, N. & Mermin, N. D. *Solid State Physics* (Books/Cole Cengage Learning, 1976).

33. Ibach, H. & Lüth, H. *Solid-state physics: an introduction to principles of materials science* (Springer Science & Business Media, 2009).

34. Kittel, C. & McEuen, P. *Introduction to Solid State Physics* (John Wiley & Sons, 2018).

35. Simon, S. H. *The Oxford Solid State Basics* (OUP Oxford, 2013).

36. YU, P. & Cardona, M. *Fundamentals of Semiconductors: Physics and Materials Properties* (Springer Berlin Heidelberg, 2005).

37. Löwdin, P.-O. Band theory, valence bond, and tight-binding calculations. *Journal of Applied Physics* **33,** 251–280 (1962).

38. Slater, J. C. & Koster, G. F. Simplified LCAO Method for the Periodic Potential Problem. *Physical Review* **94,** 1498–1524 (1954).

39. Watson, M. D. *et al.* Strong-coupling charge density wave in monolayer $\mathrm{TiSe_2}$. *2D Materials* **8,** 015004 (2020).

40. Kaneko, T., Ohta, Y. & Yunoki, S. Exciton-phonon cooperative mechanism of the triple-q charge-density-wave and antiferroelectric electron polarization in $\mathrm{TiSe_2}$. *Phys. Rev. B* **97,** 155131 (2018).

41. Parlinski, K., Li, Z. Q. & Kawazoe, Y. First-Principles Determination of the Soft Mode in Cubic $\mathrm{ZrO_2}$. *Physical Review Letters* **78,** 4063–4066 (1997).

42. Kresse, G, Furthmüller, J & Hafner, J. Ab initio Force Constant Approach to Phonon Dispersion Relations of Diamond and Graphite. *Europhysics Letters (EPL)* **32,** 729–734 (1995).

43. Antonelli, T. *et al.* Orbital-selective Band Hybridisation at the Charge Density Wave Transition in Monolayer $TiTe_2$. *arXiv:2203.15560* (2022).

44. Holy, J. A., Woo, K. C., Klein, M. V. & Brown, F. C. Raman and infrared studies of superlattice formation in $TiSe_2$. *Physical Review B* **16,** 3628–3637 (1977).

45. Crommie, M., Lutz, C. P. & Eigler, D. Imaging standing waves in a two-dimensional electron gas. *Nature* **363,** 524–527 (1993).

46. Peierls, R. E. *Quantum Theory of Solids* eng, 238 (Oxford University Press, Oxford, 2001).

47. H. Frohlich. On the theory of superconductivity: the one-dimensional case. *Proceedings of the Royal Society of London. Series A. Mathematical and Physical Sciences,* 296–305 (1954).

48. Kohn, W. Image of the Fermi Surface in the Vibration Spectrum of a Metal. *Physical Review Letters* **2,** 393–394 (1959).

49. Grüner, G. *Density waves in solids* (CRC press, 2018).

50. Rossnagel, K. On the origin of charge-density waves in select layered transition-metal dichalcogenides. *Journal of Physics: Condensed Matter* **23,** 213001 (2011).

51. Johannes, M. D. & Mazin, I. I. Fermi surface nesting and the origin of charge density waves in metals. *Physical Review B* **77,** 165135 (2008).

52. Kartoon, D., Argaman, U. & Makov, G. Driving forces behind the distortion of one-dimensional monatomic chains: Peierls theorem revisited. *Physical Review B* **98,** 165429 (2018).

53. Kwok, R. S., Gruner, G. & Brown, S. E. Fluctuations and thermodynamics of the charge-density-wave phase transition. *Physical Review Letters* **65,** 365–368 (1990).

54. Jérome, D. Organic conductors: From charge density wave TTF- TCNQ to superconducting (TMTSF) 2PF6. *Chemical Reviews* **104,** 5565–5592 (2004).

55. Chen, P. *et al.* Unique Gap Structure and Symmetry of the Charge Density Wave in Single-Layer VSe_2. *Physical Review Letters* **121,** 1–6 (2018).

56. Xi, X. *et al.* Strongly enhanced charge-density-wave order in monolayer $NbSe_2$. *Nature Nanotechnology* **10,** 765–769 (2015).

57. Ryu, H. *et al.* Persistent Charge-Density-Wave Order in Single-Layer $TaSe_2$. *Nano Letters* **18,** 689–694 (2018).

58. Chen, P. *et al.* Charge density wave transition in single-layer titanium diselenide. *Nature Communications* **6,** 8943 EP – (2015).

59. Sun, K. *et al.* Hidden CDW states and insulator-to-metal transition after a pulsed femtosecond laser excitation in layered chalcogenide 1T-$TaS_{(2-x)}Se_x$. *Science Advances* **4,** eaas9660 (2018).

60. Ang, R *et al.* Atomistic origin of an ordered superstructure induced superconductivity in layered chalcogenides. *Nature Communications* **6,** 1–6 (2015).

61. Inosov, D. *et al.* Fermi surface nesting in several transition metal dichalcogenides. *New Journal of Physics* **10,** 125027 (2008).

62. Flicker, F. & van Wezel, J. Charge order from orbital-dependent coupling evidenced by NbSe2. *Nature Communications* **6,** 7034 (2015).

63. Coelho, P. M. *et al.* Charge density wave state suppresses ferromagnetic ordering in VSe_2 monolayers. *The Journal of Physical Chemistry C* **123,** 14089–14096 (2019).

64. Duvjir, G. *et al.* Multiple charge density wave phases of monolayer VSe_2 manifested by graphene substrates. *Nanotechnology* **32,** 364002 (2021).

65. Rahn, D. *et al.* Gaps and kinks in the electronic structure of the superconductor 2H-$NbSe_2$ from angle-resolved photoemission at 1 K. *Physical Review B* **85,** 224532 (2012).

66. Strocov, V. N. *et al.* Three-Dimensional Electron Realm in VSe_2 by Soft-X-Ray Photoelectron Spectroscopy: Origin of Charge-Density Waves. *Physical Review Letters* **109,** 086401 (2012).

67. Lu, Y. *et al.* Zero-gap semiconductor to excitonic insulator transition in Ta_2NiSe_5. *Nature Communications* **8,** 1–7 (2017).

68. Hughes, H. P. Structural distortion in $TiSe_2$ and related materials-a possible Jahn-Teller effect? *Journal of Physics C: Solid State Physics* **10,** L319–L323 (1977).

69. Suzuki, N., Yamamoto, A. & Motizuki, K. Microscopic theory of the CDW state of 1 T-$TiSe_2$. *Journal of the Physical Society of Japan* **54,** 4668–4679 (1985).

70. Halperin, B. I. & Rice, T. M. Possible Anomalies at a Semimetal-Semiconductor Transistion. *Reviews Modern Physics* **40,** 755–766 (1968).

71. Kaneko, T., Toriyama, T., Konishi, T. & Ohta, Y. Orthorhombic-to-monoclinic phase transition of Ta_2NiSe_5 induced by the Bose-Einstein condensation of excitons. *Physical Review B* **87,** 035121 (2013).

72. Van Wezel, J., Nahai-Williamson, P. & Saxena, S. S. Exciton-phonon-driven charge density wave in $TiSe_2$. *Physical Review B* **81,** 165109 (2010).

73. Cho, A. Y. Film deposition by molecular-beam techniques. *Journal of Vacuum Science and Technology* **8,** S31–S38 (1971).

74. Chambers, S. A., Kaspar, T. C., Prakash, A., Haugstad, G. & Jalan, B. Band alignment at epitaxial $BaSnO_3/SrTiO_3$ (001) and $BaSnO_3/LaAlO_3$ (001) heterojunctions. *Applied Physics Letters* **108,** 152104 (2016).

75. Cirlin, G. *et al.* Critical diameters and temperature domains for MBE growth of III–V nanowires on lattice mismatched substrates. *physica status solidi (RRL)–Rapid Research Letters* **3,** 112–114 (2009).

76. Petroff, P. & DenBaars, S. MBE and MOCVD growth and properties of self-assembling quantum dot arrays in III-V semiconductor structures. *Superlattices and microstructures* **15,** 15 (1994).

77. Koma, A. Molecular beam epitaxial growth of organic thin films. *Progress in crystal growth and characterization of materials* **30,** 129–152 (1995).

78. Lüth, H. *Solid surfaces, interfaces and thin films* (Springer, 2001).

79. Rajan, A., Underwood, K., Mazzola, F. & King, P. D. C. Morphology control of epitaxial monolayer transition metal dichalcogenides. *Phys. Rev. Materials* **4,** 014003 (2020).

80. Horio, Y. Reflection High-Energy Electron Diffraction. *Compendium of Surface and Interface Analysis,* 527–530 (2018).

81. Hasegawa, S. Reflection high-energy electron diffraction. *Characterization of Materials* **97,** 1925–1938 (2012).

82. Hüfner, S. *Photoelectron spectroscopy principles and applications* (Springer Science & Business Media, 2013).

83. Damascelli, A. Probing the electronic structure of complex systems by ARPES. *Physica Scripta* **2004,** 61 (2004).

84. Willmott, P. *An introduction to synchrotron radiation: techniques and applications* (John Wiley & Sons, 2019).

85. Pereira, V. M. *et al.* Challenges of topological insulator research: Bi_2Te_3 thin films and magnetic heterostructures. *physica status solidi (b)* **258,** 2000346 (2021).

86. Duvjir, G. *et al.* Emergence of a Metal–Insulator Transition and High-Temperature Charge-Density Waves in VSe_2 at the Monolayer Limit. *Nano Letters* **18,** 5432–5438 (2018).

87. Koike, Y., Okamura, M., Nakanomyo, T. & Fukase, T. Log T Dependence of Resistivity and Negative Magnetoresistance in the Layered Compound $TiTe_2$. *Journal of the Physical Society of Japan* **52,** 597–604 (Feb. 1983).

88. Allen, P. B. & Chetty, N. $TiTe_2$: Inconsistency between transport properties and photoemission results. *Phys. Rev. B* **50,** 14855–14859 (1994).

89. Claessen, R. *et al.* Complete band-structure determination of the quasi-two-dimensional Fermi-liquid reference compound $TiTe_2$. *Phys. Rev. B* **54,** 2453–2465 (1996).

90. Strocov, V. *et al.* Three-dimensional band structure of layered $TiTe_2$ Photoemission final-state effects. *Physical Review B* **74,** 195125 (2006).

91. Guster, B., Robles, R., Pruneda, M., Canadell, E. & Ordejón, P. 2×2 charge density wave in single-layer $TiTe_2$. *2D Materials* **6,** 015027 (2018).

92. Zhou, J. S. *et al.* Theory of the thickness dependence of the charge density wave transition in 1T-$TiTe_2$. *2D Materials* **7,** 045032 (2020).

93. Bawden, L. *et al.* Hierarchical spin-orbital polarization of a giant Rashba system. *Science Advances* **1,** e1500495 (2015).

94. Cao, Y. *et al.* Mapping the orbital wavefunction of the surface states in three-dimensional topological insulators. *Nature Physics* **9,** 499–504 (2013).

95. Zhu, Z.-H. *et al.* Photoelectron Spin-Polarization Control in the Topological Insulator Bi_2Se_3. *Physical Review Letters* **112,** 076802 (2014).

96. Kane, E. O. Band structure of indium antimonide. *Journal of Physics and Chemistry of Solids* **1,** 249–261 (1957).

97. Voit, J. *et al.* Electronic Structure of Solids with Competing Periodic Potentials. *Science* **290,** 501–503 (2000).

98. Sunko, V. *et al.* Probing spin correlations using angle-resolved photoemission in a coupled metallic/Mott insulator system. *Science Advances* **6,** eaaz0611 (2020).

99. Song, Y. *et al.* Signatures of excitonic insulating state in monolayer 1T-$ZrTe_2$. *arXiv:2201.11592* (2022).

100. Tsipas, P. *et al.* Epitaxial $HfTe_2$ Dirac semimetal in the 2D limit. *APL Materials* **9,** 101103 (2021).

101. Hellgren, M. *et al.* Critical Role of the Exchange Interaction for the Electronic Structure and Charge-Density-Wave Formation in $TiSe_2$. *Physical Review Letters* **119,** 176401 (2017).

102. Lian, C., Zhang, S.-J., Hu, S.-Q., Guan, M.-X. & Meng, S. Ultrafast charge ordering by self-amplified exciton–phonon dynamics in $TiSe_2$. *Nature Communications* **11,** 1–8 (2020).

103. Xie, L. Two-dimensional transition metal dichalcogenide alloys: preparation, characterization and applications. *Nanoscale* **7,** 18392–18401 (2015).

104. Zuo, Y. *et al.* Robust growth of two-dimensional metal dichalcogenides and their alloys by active chalcogen monomer supply. *Nature Communications* **13,** 1007 (Feb. 2022).

105. Arnaud, Y. & Chevreton, M. Etude comparative des composés TiX_2 (X = S, Se, Te). Structures de $TiTe_2$ et TiSeTe. *Journal of Solid State Chemistry* **39,** 230–239 (1981).

106. May, M. M. *PhD thesis: Two ways of suppressing charge density waves in 1T-$TiSe_2$* (Humboldt-Universit¨at zu Berlin, 2010).

107. Chen, P. *et al.* Atomic-Scale Chemical Conversion of Single-Layer Transition Metal Dichalcogenides. *ACS Nano* **13,** 5611–5615 (2019).

108. Linderälv, C., Rahm, J. M. & Erhart, P. High-throughput characterization of transition metal dichalcogenide alloys: Thermodynamic stability and electronic band alignment. *arXiv:2204.11223* (2022).

109. Wagner, C. *et al.* NIST X-ray Photoelectron Spectroscopy Database, NIST Standard Reference Database 20, Version 3.4 (Web Version). *US Department of Commerce* (2003).

110. Lee, S. Y. *et al.* Large work function modulation of monolayer MoS_2 by ambient gases. *Acs Nano* **10,** 6100–6107 (2016).

111. Mammadov, S. *et al.* Work function of graphene multilayers on SiC (0001). *2D Materials* **4,** 015043 (2017).

112. Katzke, H, Tolédano, P & Depmeier, W. Theory of morphotropic transformations in vanadium oxides. *Physical Review B* **68,** 024109 (2003).

113. Brahlek, M. *et al.* Opportunities in vanadium-based strongly correlated electron systems. *MRS Communications* **7,** 27–52 (2017).

114. Hansmann, P *et al.* Mott Hubbard transition in V_2O_3 revisited. *physica status solidi (b)* **250,** 1251–1264 (2013).

115. Pergament, A., Stefanovich, G. & Velichko, A. Oxide electronics and vanadium dioxide perspective: A review. *Journal on Selected Topics in Nano Electronics and Computing* **1,** 24–43 (2013).

116. Wang, Y., Nakano, M., Kashiwabara, Y., Matsuoka, H. & Iwasa, Y. Transport properties of a few nanometer-thick $TiSe_2$ films grown by molecular-beam epitaxy. *Applied Physics Letters* **113,** 073101 (2018).

117. Dillemans, L. *et al.* Correlation between strain and the metal–insulator transition in epitaxial V_2O_3 thin films grown by Molecular Beam Epitaxy. *Thin Solid Films* **520,** 4730–4733 (2012).

118. Dillemans, L. *et al.* Evidence of the metal-insulator transition in ultrathin unstrained V_2O_3 thin films. *Applied Physics Letters* **104,** 071902 (2014).

119. Feiten, F. E., Kuhlenbeck, H. & Freund, H.-J. Surface structure of V_2O_3 (0001): A combined I/V-LEED and STM study. *The Journal of Physical Chemistry C* **119,** 22961–22969 (2015).

120. Dupuis, A.-C., Haija, M. A., Richter, B., Kuhlenbeck, H. & Freund, H.-J. V_2O_3 (0001) on Au (111) and W (110): growth, termination and electronic structure. *Surface Science* **539,** 99–112 (2003).

121. Sass, B *et al.* Structural and electronic properties of epitaxial V_2O_3 thin films. *Journal of Physics: Condensed Matter* **16,** 77 (2003).

122. Wang, K. & Smith, A. R. Efficient kinematical simulation of reflection high-energy electron diffraction streak patterns for crystal surfaces. *Computer Physics Communications* **182,** 2208–2212 (2011).

123. Singer, A. *et al.* Nonequilibrium phase precursors during a photoexcited insulator-to-metal transition in V_2O_3. *Physical Review Letters* **120,** 207601 (2018).

124. Yoshida, M., Suzuki, R., Zhang, Y., Nakano, M. & Iwasa, Y. Memristive phase switching in two-dimensional 1T-TaS_2 crystals. *Science Advances* **1,** e1500606 (2015).

125. Nguyen, P. V. *et al.* Visualizing electrostatic gating effects in two-dimensional heterostructures. *Nature* **572,** 220–223 (2019).